THE PROJECTILE IMPACT RESPONSES OF THE COMPOSITE FACED ALUMINUM FOAM AND CORRUGATED ALUMINUM SANDWICH STRUCTURES: A COMPARATIVE STUDY

A Thesis Submitted to
the Graduate School of Engineering and Sciences of
İzmir Institute of Technology
in Partial Fulfillment of the Requirements for the Degree of

MASTER OF SCIENCE

in Mechanical Engineering

by
İsmet Kutlay ODACI

July 2011
İZMİR

We approve the thesis of **İsmet Kutlay ODACI**

Prof. Dr. Mustafa GÜDEN
Supervisor

Assoc. Prof. Dr. Alper TAŞDEMİRCİ
Co-supervisor

Prof. Dr. Ramazan KARAKUZU
Committee Member

Prof. Dr. Hasan YILDIZ
Committee Member

Assist. Prof. Dr. Selçuk SAATÇİ
Committee Member

4 July 2011

Prof. Dr. Metin TANOĞLU
Head of the Department of
Mechanical Engineering

Prof. Dr. Durmuş Ali DEMİR
Dean of the Graduate School
of Engineering and Sciences

ACKNOWLEDGEMENTS

I would like to express my deep and sincere gratitude to my supervisor Prof. Dr. Mustafa GÜDEN and my Co-Advisor Associate. Prof. Dr. Alper TAŞDEMİRCİ for their instructive comments, encouragement, guidance and support from the beginning to the final stage enabled to me to completely understand the subject. I also thank to Cumhur AKAR for his material and technical support during this study.

I gratefully thank to my colleagues, Cenk Kılıçaslan, Ali Kara, Ali Kıvanç Turan and Gözde Tunusoğlu for their support and help. I also wish to thank my family who deserve a special mention for their endless support and prayers. My father, Necmi ODACI, is the person who helped and directed me during my whole education life to be successful. My mother, Mine ODACI, is the one who sincerely raised me with her caring and gently love. Sılay ODACI thanks for being supportive and caring sibling.

Furthermore, I would like to thank my girlfriend Burcu ALAÇAM whose love, patience and permanent confidence in me, has made the life easier during my study. Finally, I would like to thank everyone who helped me during this thesis and I offer an apology that I could not mention personally one by one.

ABSTRACT

THE PROJECTILE IMPACT RESPONSES OF THE COMPOSITE FACED ALUMINUM FOAM AND CORRUGATED ALUMINUM SANDWICH STRUCTURES: A COMPARATIVE STUDY

The projectile impact and energy absorption characteristics of the corrugated aluminum cored E-glass/polyester composite sandwich structures were determined at the impact velocities of 150 m/s. For comparison, E-glass/polyester sandwich structures cored with aluminum foam were also investigated. The test conditions were kept the same for each structure in order to identify the impact properties at the similar test conditions. The composite and the foam core composite sandwiches were produced by vacuum assisted resin transfer molding and the mechanical tests were performed on the composite and core samples based on ASTM. High strain rate tests were performed using a compression type Split Hopkinson Pressure Bar and drop weight test set-up. It was found that aluminum foam sandwich structures had higher ballistic limit and energy dissipating performance than corrugated aluminum sandwich structures; however, as the thickness of the face sheets increased the corrugated aluminum cores were observed to be more effective. The results showed that corrugated aluminum structures had the potentials to be used as core material in composite sandwich structures.

ÖZET

KOMPOZİT YÜZLÜ ALÜMİNYUM KÖPÜK VE DALGALI ALÜMİNYUM SANDVİÇ YAPILARIN PROJEKTÖR ÇARPIŞMA DAVRANIŞI: KARŞILAŞTIRMALI ÇALIŞMA

Cam elyaf/polyesterden kompozit yüzlü dalgalı alüminyum göbekli sandviç malzemelerin balistik limiti ve enerji yitim performansı 150 m/s darbe hızlarında belirlenmiştir. Kıyaslama amacı ile, cam elyaf/alüminyum köpük sandviç malzemelerde araştırılmıştır. Darbe özelliklerini aynı koşullarda belirlemek için her iki malzeme için testler aynı koşullarda yapılmıştır. Kompozit ve köpük göbekli kompozit sandviç yapılar vakumla desteklenmiş reçine transferi ile kalıplama yöntemiyle hazırlanmış ve kompozit ve göbek malzemeler üzerine mekanik testler ASTM standartlarına göre uygulanmıştır. Yüksek hız testleri split Hopkinson basınç barı ve düşen ağırlık test metotları kullanılarak yapılmıştır. Alüminyum sandviç köpüklerin dalgalı alüminyum sandviç yapılardan daha yüksek balistik limite ve enerji yitim performansına sahip olduğu ve ancak yüzey kaplaması kalınlığı arttıkça dalgalı alüminyum sandviç yapıların etkinliğinin arttığı bulunmuştur. Sonuçlar, dalgalı alüminyum yapıların sandviç yapılarda göbek malzemesi olarak kullanılabileceği potansiyeline sahip olduğunu göstermiştir.

TABLE OF CONTENTS

LIST OF FIGURES

Figure **Page**

LIST OF TABLES

Table **Page**

CHAPTER 1

INTRODUCTION

1.1. Introduction

The use of sandwich structures is becoming increasingly popular in the design of light-weight structures. Sandwich structures offer light weight, substantial bending strength and impact resistance, as load-bearing components, in many applications including satellites, aircrafts, ships, automobiles, rail cars, wind energy systems and bridge constructions. The sandwich structures normally consist of a low density core material sandwiched between two stiff face skins. Commonly used face skin materials are composites and metals, while the cores are generally constructed from honeycombs, foams, balsa wood and trusses. The face skins carry almost all of the bending and in-plane loads and the core materials function to stabilize the face skins and define the flexural stiffness and out-of- plane shear and compressive behavior [1]. A typical sandwich structure is depicted in Figure 1.1. In the same figure, a is the length of the face sheet and the core material, t is the thickness of face sheet, c is the thickness of core material and h is the total thickness of the sandwich structure.

Sandwich structures can be combinations of variety of materials depending on the requirements. One of these combinations is the composite sandwich structure, which is generally used in commercial aircrafts. The composite sandwich structures are used both interior and external structure of the aircrafts as shown in Figure 1.2. The interior applications are fairings and the floor panels in passenger compartment. The typical external applications are the radar domes, belly fairings, engine cowlings, leading and trailing edge fairings and landing gear doors. Radar domes and leading edge fairings are exposed to impacts due to bird and lightning strikes and the abrasion caused by rain and dust. Furthermore, foreign object damage caused by runway debris is another important problem for the lower side of the aircraft.

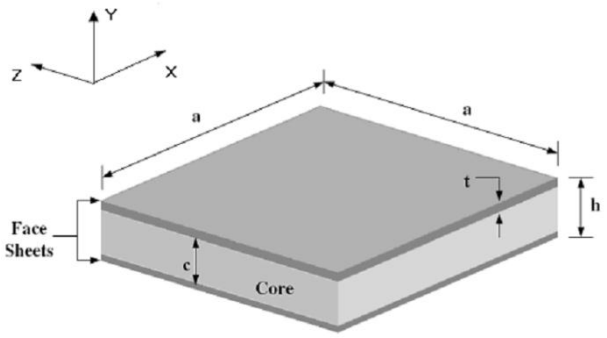

Figure 1.1. Sandwich structure and geometrical parameters.

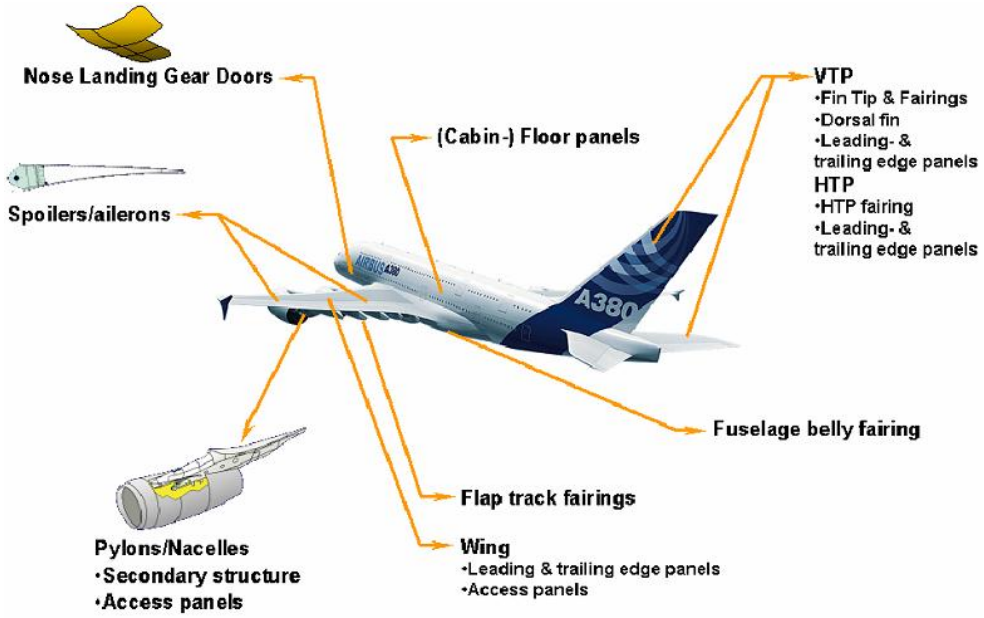

Figure 1.2. Composite sandwich applications in A380 .
(Source: Hermann, 2005)

The aircraft design is a complicated process, for which many parameters relating safety regulations should be taken into account [2]. In addition to these design parameters, environmental effects such as bird strike and runway and tire debris impacts have to be considered in the designing stages. The design should include the materials that may withstand crash and impact loads. Consequently, the material's strain-rate sensitivity, energy absorption and deformation mechanisms are needed to be characterized at increasing high deformation rates in order to reach reliable material properties in the designing stage.

Tire debris is one of the most dangerous impacts that can occur with aircraft structures. The impact of such materials on fuel tank panel, cabin, engine coverings, wing and some electronics can lead to fatal consequences. In order to take precautions against the debris impacts, the tests that simulate component behavior must be performed on the structural materials.

1.2. Aim and Scope of the Study

The applications of composite materials and sandwich structures in aerospace and other industries are increasing because of their light weight and strength. They also offer good energy absorption and shielding properties. Several experiments have been carried out to find ballistic limit, mode of failure and the materials properties but further study is needed to fully characterize and model the behavior of sandwich structures under impact loading, particularly with novel light weight core materials.

Corrugated aluminum structures are moderately new materials offering pretty much similar mechanical properties with aluminum foams. Corrugated aluminum structures are also noted to have more homogeneous/regular cellular structure than aluminum foams; hence are expected to provide reliability in the structures. To be used as core materials in sandwich structures, the performances and advantages of the corrugated structures over commercially available aluminum foam cores in sandwich plates should be identified. The aim of this study is therefore to determine the projectile impact and energy absorption characteristics of the corrugated aluminum cored E-glass/polyester composite sandwich structures. For comparison, E-glass/polyester sandwich structures cored with aluminum foam were also investigated. The test conditions were kept the same for each structures in order to identify the impact properties at the similar test conditions.

The content of the thesis are as follows. The applications and properties of the sandwich structures are summarized in Chapter 1. The energy dissipating performance, ballistic limits and failure modes of sandwich structures and the projectile impact test setups and the test procedures in the literature are reviewed in Chapter 2. The materials and material processing methods and testing methods are given in Chapter 3. The test results and the comparison of the test results are given in Chapter 4. Discussion of the results and conclusion are given in Chapter 5 and Chapter 6, respectively.

CHAPTER 2

LITERATURE SURVEY

2.1. Introduction

Projectile impact tests have been applied to composite laminates and sandwich structures for a long time in order to identify the impact response and energy absorbing characteristics. The penetration characteristics of composite materials at high velocities become very much important as they are increasingly used in the protective helmet, protective body armor, load-bearing structures, inner and outer components of the aircraft and military vehicles and equipment.

2.2. The Projectile Impact and Low Velocity Impact Response of Laminated Composites

Cantwell and Motron [3] examined the perforation behavior of carbon fiber reinforced plastic composites. The effects of target thickness and length on the perforation energy of the composite were determined in the same study. At low velocity, the areal geometry of the target was found to determine the perforation threshold energy. While, at high velocity impact loading, the perforation threshold appeared to be independent of the areal geometry of the target. Moreover, a simple perforation model was proposed based on the dissipation of energy during the impact. A good correlation between the experimental and the model-predicted results was reported for the target thicknesses up to 4 mm. For thicker targets, the model was shown to not applicable due to change in the perforation mode.

Zhu et al. [4] investigated the impact response of woven Kevlar/polyester laminates varying in thicknesses using cylindro-conical projectiles. Ballistic limits were determined for a series of the targets ranging the thicknesses from 3.125 to 12.7 mm. It was reported that local deformation and fiber failure constituted the major energy absorption mechanisms in target perforation. Quasi-static and dynamic delaminations

were found to dissipate a large amount of energy. Zhu et al. [5]developed an analytical representation of the normal impact and perforation of conically-tipped hard-steel cylinders. The model utilized the laminated plate theory to determine global target deflection. Dissipative mechanisms, including indentation of the striker tip, bulging at the surface, delamination, fiber failure and friction were included in the model. The predicted ballistic limits by the model agreed well with those of test results; the difference was 12% and 1.3% for thinner (3.125 mm) and thicker (9.525 mm) specimen, respectively.

Lee and Sun [6] developed a quasi-static model to simulate the penetration process of composite laminates struck by blunt-ended projectiles. A series of static punch tests was conducted to characterize the load-displacement curves during the penetration in $([0/90/45/-45]_s)_2$ Hercules AS4/3501-6 graphite/epoxy composites. The major damage modes were reported to be delamination and plugging. An axisymmetric finite element analysis was performed to simulate the quasi-static penetration process. Comparisons of punch load-displacement curves showed a good agreement between models and tests. Lee and Sun [7] determined the ballistic limit of graphite/epoxy laminates struck by a blunt-ended projectile. Comparison between the computed ballistic limit and test results further showed good agreement.

Sun and Potti [8] utilized the static punch curve as a basis to calculate the energy required for the penetration of composite laminates. A series of impact tests was performed on 2, 4.1, 6.1, and 8.1 mm thick graphite-epoxy (Hercules AS4-3501/6) quasi-isotropic composite laminates. The hardened tool steel projectile was 14.6 mm in diameter and 24 mm in length. The projectile tests were performed at incident velocities ranging from 20 to 150 m/s. The overall damage pattern in the dynamic case was found to be similar to that of the static case. The residual velocities predicted using static punch-through energy overestimated the experimental values for thick laminates. But, the method provided an easy and inexpensive upper bound approximation.

Jenq et al. [9] predicted the ballistic limit of plain woven glass/epoxy composite laminates struck by a 14.9 g bullet-like rigid projectile with a tip radius of 5 mm. The 4 mm thick square specimens were clamped along their 100 mm edges. A pneumatic gun was used to propel the bullet with the incident velocities ranging from 140 to 200 m/s. The ballistic limit was experimentally determined to be 153 m/s. A series of quasi-static punch tests was also performed in order to investigate the progressive damage modes of

the targets and to obtain the punch load-displacement curves. These quasi-static punch tests were conducted to characterize the penetration process. Similar to dynamic impact test results, the major damage modes for targets subjected to quasi-static punch loading were found to be governed by delamination and fiber breakage. After specimens were perforated, a steady friction force was observed in the quasi-static punch tests. Test results indicated that the rhombus-shaped delamination of impact damaged samples was greater than that of quasi-statically punched specimens. A partial hybrid stress finite element code was incorporated with the proposed static penetration model to simulate the dynamic impact process. An energy consideration was applied to predict the ballistic limit. The difference between the predicted and test ballistic limits was found 24% when the target's static material properties were used in the simulation. Due to the rate-sensitive nature of glass/epoxy composites, the effect of dynamic elastic properties on the predicted ballistic limit was further investigated. Good agreement between the predicted and test ballistic limits was found, when the target's elastic moduli were taken two times of the static values.

Morye et al. [10] developed a simple model predicting the energy absorption mechanisms of the polymeric nylon-A, nylon-B, aramid and dynemaa UD66 composite plates at the ballistic limit. The first mechanism was the energy absorption in the tensile failure of the primary yarns, the second was the energy absorption in the elastic deformation of the secondary yarns and the third was the energy absorbed in the form of kinetic energy of the moving cone. In the experiments, the kinetic energy of the moving cone was determined the dominant energy absorbing mechanism. The results of the ballistic experiments and the model were found to be in good agreement for nylon-A, nylon-B and aramid composites, while the test and model results of dynemaa UD66 composite showed discrepancy because of the low through-thickness shear modulus of the composite.

Billon and Robinson [11] presented two numerical and an analytical model for assessing the projectile impact of multiple layers of ballistic nylon, high modulus polyethylene (HMPE) and aramid fabric. The experiments were performed using a gas gun at velocities in the range of 200-750 m/s using 5.59 or 7.62 mm diameter projectiles. Nylon/HMPE (9/7 ply sequence) had the highest ballistic limit, then aramid layers had the second highest ballistic limit. Furthermore, the test results showed good agreements with those of the numerical models for aramid fabric, while showed poor

agreement for HMPE and Nylon fabrics. Since the ballistic limits predicted for hybrids using the analytical model were in good agreement with experiments, the analytical model was reported to provide a practical means of rapidly determining the ballistic limits of new fabric armor designs.

Wen et al. [12] proposed analytical equations to predict the penetration and perforation of thick fiber reinforced plastic (FRP) laminates struck normally by missiles over a wide range of impact velocity. Truncated, conical, flat, ogival and hemispherical missile nose shapes were used in the formulation of the penetration depth. The formulations were based on the localized deformation assumption. The mean pressure of the targets to resist the missiles consisted of two components. One component was cohesive quasi-static resistive pressure due to the elastic-plastic deformation of the laminate materials; the other is a dynamic resistive pressure arising from velocity effects. Analytical equations were derived for the depth of penetration in the FRP laminate targets and the ballistic limits in the case of perforation.

Cui et al. [13] investigated the impact response and energy absorbing characteristics of laminated foam and honeycomb sandwich composites. A model was proposed in order to predict the ballistic limit of laminated composites. The ballistic limit and energy absorption per unit thickness of the three composites under different conditions were calculated and it was shown that honeycomb sandwich composite had the highest ballistic resistance and energy absorption among the three composites.

Gellert et al. [14] conducted ballistic tests on glass/fiber reinforced plastic composite plates of various thicknesses using hard steel cylinders in two different diameters and three different nose shapes. A simple model was developed to explain the bi-linear behavior, provided the basis for geometrical scaling of composite ballistic perforation data. The study showed that energy absorption in thin composite targets was largely independent of projectile nose geometry and thin glass/fiber reinforced and Kevlar composite targets responded similarly to the fragment simulating projectiles on a thickness basis. Furthermore, the deformation mechanisms were found to be cone delamination towards the exit side and fiber breakage in the through thickness direction. Finally, the analysis showed that the indentation phase was the most significant absorber of energy and should be maximized in any bonded composite armor design, indicating that thicker targets were more efficient ballistically, especially against blunt projectiles.

Naik et al. [15] studied the projectile impact behavior of two dimensional fabric E-glass/epoxy composites. It was shown that a significant amount of energy was transferred as the kinetic energy of the moving cone during impact. The major energy absorbing mechanisms were reported to be deformation of secondary yarns and fracture of primary yarns. The increase in cone surface radius was nearly linear with respect to time. The rate of increase of cone depth/height decreased with time. The contact duration between the projectile and the target decreased as the incident ballistic impact velocity increased. Above the ballistic limit velocity, the reduction in the contact duration was shown to be significant. As the stress wave transmission factor increased, the ballistic limit increased. As the diameter of the projectile increased, the ballistic limit velocity increased for the same mass of the projectile. As the mass of the projectile increased, the ballistic limit velocity decreased for the same diameter of the projectile. As the target thickness increased, the ballistic limit velocity increased for the same mass and diameter of the projectile.

Gower et al. [16] performed both experimental and numerical studies on the impact response of Kevlar 29 and 129 composite panels used in the protective body armor. The composite panels were impacted using two different projectiles; 7.5 mm diameter hardened steel 120° cylindrical–conical, and 9 mm hemispherical nosed non-deformable 4340 hardened steel. The impact velocity ranged between 130 and 250 m/s, which were below the penetration limit of the panels. This allowed the study of the back face signature (BFS) of the composite panels. Results showed that Kevlar 29 exhibited a lower BFS than the Kevlar 129 at low impact speeds; however, this changed for higher velocity impacts. The Kevlar 129 panels showed reduced BFS with blunt projectiles and less resistance to penetration with sharp projectiles as compared with the Kevlar 29 panels.

Cheeseman and Bogetti [17] reviewed the factors that influenced the ballistic performance of the composites including the material properties of the yarn, fabric structure, projectile geometry and velocity, far field boundary conditions, multiple plies and friction. The effects of factors were investigated one by one or by a combination of two or more factors (i.e., the effect of projectile geometry and velocity on different fabric structure).

Ulven et al. [18] studied the ballistic impact resistance of carbon/epoxy fiber composites. Two different thicknesses of carbon composite panels were investigated;

3.2 mm (7 layers) and 6.5 mm (17 layers). The impact tests were performed using a gas-gun setup with four different 14 grams tool steel projectiles geometries; hemispherical, conical, fragment simulating and flat tip. The ballistic limit was taken as the velocity at which the projectile almost emerged from the back face of the sample. The conical projectile resulted in the highest energy absorption followed by the flat, hemispherical and fragment simulating projectiles. The fragment simulating projectile initially created a shear zone followed by elastic/plastic hole enlargement. The flat projectile created a shear zone resulting in plugging or ejection of a circular plug but the energy absorption was much smaller due to the large impact face. Failure in the panels impacted with the conical and hemispherical projectile was elastic/plastic hole enlargement, in which the fibers were spread and stretched while the projectile penetrated. Due to a small angle on the conical projectiles and the large surface area on the hemispherical projectiles, part of the failure was also observed to result in the shear loading of the laminate. In addition, the energy absorbed by the panels increased as the amount of cracking due to back face tension increased. The cracking was observed to be more significant in transverse direction than longitudinal direction. Finally, the penetration of carbon/epoxy panels impacted by different shape projectiles was concluded to be significantly dependent on the panel thickness.

Faur-Csukat et al. [19] investigated the mechanical behavior and ballistic performance of carbon, glass, aramid and polyethylene fabric reinforced composites with different epoxy resins: Eporezit AH16+Hardener T54, XB 3517+Hardener XB 3419, Eporezit AH 16+Hardener T58 and Polypox E492. The highest energy absorption was found in glass reinforced composites. Aramid and dyneema reinforced composites exhibited relatively good energy absorption, while the energy absorption of the dyneema reinforced composite was lower than that of the aramid reinforced composite. On the other hand, carbon fabric reinforced composites showed relatively low energy absorption. The specific energy absorption ability of E-glass and carbon fabric composites increased with the increasing number of the plies; therefore, the efficiency of the layers also increased. The basket wave fabric structure reinforced samples showed 10% higher energy absorption in all cases than plain weave fabric reinforced samples.

Davies et al. [20] investigated flat nose projector impact response of thick glass/polyester and glass/phenolic laminates. The compression after impact tests showed

that the residual strength of the thick impacted plates was higher than that of the thin plates when plotted against impact force and only fractionally higher when plotted against incident kinetic energy. The deformation mechanism of 10 mm thick plates was dominated by matrix cracking that surrounded the immediate vicinity of the impact contact area. Surface micro-buckling was also seen to propagate along the undulating fiber directions in the shape of a cross. The deformation mechanism of 25 mm thick plate was extensive delamination, fiber shear-out and fiber fracture.

Belingardi and Vadori [21] worked on the glass fiber reinforced epoxy matrix composites suitable for constructing structural parts devoted to dissipate kinetic energy during impacts. The low velocity impact tests were conducted according to ASTM 3029 standard. Different levels of impact kinetic energy were obtained by changing the drop height and as a result the impact velocities were altered. The glass fiber reinforced epoxy matrix composite specimens were produced with three different stacking sequences, [0/90]s, [0/+60/60]s, [0/+45/-45]s, and also with woven and unidirectional layout. Fiber fraction in all samples ranged between 62% and 66%. The test specimens were prepared in accordance with ASTM 3029 standard. The test results were evaluated according to three cases, the first one was free fall, stop and rebound case in which the energy absorbed by the specimen was not too high and a rebound occurred. The second one was free fall and stop case in which the projector stopped without rebounding. The final case was free fall and perforation in which the energy was higher than saturation energy. Furthermore, two thresholds were identified according to the force versus displacement curves; the damage force and the maximum force. It was concluded that the values of these two thresholds remained constant with the impact energy. Finally, by comparing the force versus displacement and the energy versus displacement curves, it was concluded that the glass fiber epoxy matrix had no strain rate sensitivity.

Sevkat et al. [22] studied the progressive damage behavior of woven S2-glass/toughened epoxy, woven IM7-graphite/toughened epoxy and woven S2-glass-IM7-graphite fibers/toughened epoxy hybrid woven composite panels impacted by drop-weights at four different velocities by a combined experimental and 3-D dynamic nonlinear finite element approach. The fiber volume of the test specimens was 55% and the thickness was 6.35 mm. Four different stacking sequences of composite structure were investigated. The first stacking sequence was glass fabrics (GL), second type had glass fabrics outside and graphite fabrics inside (GL/GR/GL), the third type had

graphite skins outside and glass core inside (GR/GL/GR) and the fourth type, called the GR specimen, consisted of graphite fabrics. GL composite was found to have the highest impact resistance and GL/GR/GL hybrid composite had the second highest impact resistance, GR/GL/GR hybrid composite had the third highest impact resistance and finally GR non-hybrid composite had the least impact resistance. It was further observed that the hybrid composites were prone to delamination, especially between dissimilar layers but they satisfied the control of impact force and damage. Finally, the results of the FE simulations with LS-DYNA offered good agreement with experimental results.

2.3. The Projectile Impact Response of Sandwich Structures

Hou et al. [23] investigated the quasi-static indentation and ballistic impact response of aluminum sandwich structures with CYMAT closed cell aluminum foam core using flat, hemispherical and conical stainless steel projectiles. The face-sheets were glued onto the surfaces of the foam core using an epoxy adhesive. It was found that the dynamic perforation significantly increased the perforation energy; the thicker skins and the cores resulted in higher ballistic limits and larger delamination area between the core and back face and blunter projectiles resulted in larger petalling area and tended to increase the ballistic limit and energy dissipation.

Hanssen et al. [24] conducted experimental tests and LS-DYNA simulations of a bird striking a double sandwich panel made from AlSi7Mg0.5 aluminum foam core and AA2024-T3 aluminum face sheets. Birds were used as projectiles in the tests with velocities of 140 m/s and 190 m/s. The back sheet of the double sandwich panel was instrumented by a set of strain gages centered on the impact area to capture the strains. No complete penetration of the panels took place in the experiments and also for the model. It was found that the model represented local strains, global deformation behavior and local failure fairly well.

Roach et al. [25] studied static and dynamic penetration energies of E-glass woven/polyester laminates with a closed cell PVC foam core. The indenters used were all flat-faced and 20 mm in diameter. It was found that the static penetration energy of the laminates with and without core were similar for thicknesses of 2, 4 and 8 mm. However, 16 mm thick laminate without a core sustained a noticeably greater energy to

penetration than the laminate with a core. The dynamic impact response of 2.64 mm thick laminate was dominated by global rather than local deformation at 30 m/s. Laminates of 4.15 mm and 4.52 mm thick showed some evidence of global deformation with slight fiber failure at the edges, although the damage was dominated by delamination in the central region of the specimen. Laminates of 7.91 mm and 8.04 mm thick showed delamination predominantly in the central region, implying that the failure process was localized and similar in nature to the static case. At 60 m/s impact tests similar behavior was observed. At 120 m/s impact tests only 4.52 mm and 7.91 mm laminates were fully penetrated. Finally, it was concluded that the static penetration tests were inadequate to estimate the impact penetration energy.

Villanueva and Cantwell [26] studied the high velocity impact response of Alporas aluminum foam core sandwich structures with unidirectional glass fiber polypropylene, woven glass fiber polypropylene and aluminum 2024-T3 alloy plain skins. Four different types of sandwich structures were produced by using sheets of glass fiber reinforced polypropylene (GFPP) prepreg and combinations of GFPP and aluminum 2024T3 (for the FML skins) which were stacked on either side of a 10 mm aluminum foam. The specific perforation energy of the tested structures from highest to lowest ones were as follows; cross-ply glass fiber reinforced polypropylene, woven glass fiber reinforced polypropylene, the unidirectional fiber-metal laminate third and aluminum 2024 T3 alloy sheet. The energy absorption mechanisms of the GFPP skinned aluminum foam sandwich structures were found to be fiber-matrix delamination, longitudinal splitting and fiber fracture in the composite skins and indentation, progressive collapse and densification in the aluminum foam. The energy absorption mechanisms of the FML skinned sandwich structures were the fracture of the aluminum alloy, longitudinal splitting and fiber fracture in the FML skin and indentation, crushing and densification in the aluminum foam.

Zhou and Stronge [27] investigated the perforation of monolithic and two-layered steel sheets and lightweight sandwich panels both experimentally and numerically. The projectiles used in the experiments were short cylindrical projectiles with either a flat or hemispherical nose that struck the target at an angle of obliquity between 0° and 45°. ABAQUS/explicit was used to simulate both the impact response of monolithic and layered plates. The hemispherical projectile was found to induce a higher ballistic limit than flat projectile because there was more localized deformation

near the penetrating corner of the projectile's nose. Furthermore, layered plates were found to have higher ballistic limit than monolithic plates composed of the same material and having the same material thickness for oblique impact by a flat projectile. For oblique impact by hemispherical-nosed projectiles, monolithic plates and sandwich panels had nearly the same ballistic limit. Finally, obliquity angles between 30° and 45° had the minimum ballistic limit for thin metallic plates which were penetrated by both hemispherical and flat-nosed projectiles.

Aktay et al. [28] studied the damage behavior of composite sandwich panels with aramid paper honeycomb (NOMEX) and polyetherimide (PEI) foam cores under transverse impacts at high velocities. Hard and soft projectiles were used to simulate the impact scenarios for an aircraft structure. Hard projectiles represented the runaway and engine debris impacts; on the other hand, soft projectiles represented the bird strike or burst tire rubber fragments impacts. The maximum expected impact speed of runaway debris on an aircraft structure during start and landing was chosen as 60 m/s. Concrete spherical nosed cylindrical projectiles 26 mm in diameter and 37 mm in length were used in the impact tests. PAM-CRASH, a commercial explicit FE crash code, was used to model the impact response of the composite faces and foam cores. The numerical impact models provided reasonable accurate details of high velocity impact on sandwich structures including impact force, displacement, velocity, energy response and damage development during impact.

Goldsmith et al. [29] investigated the ballistic perforation characteristics of Al 5052 H39 alloy and acrylonitrile-betadyne styrene (ABS) sandwich structures with honeycombs or flexible sheets of aluminum 2024 alloys (Flexcore) cores in the axial direction using hardened steel projectiles of two different sizes with three different geometries; spherical, cylindro-conical and cylindrical. It was found that thinner Flexcore pierced by a 6.35 mm diameter projectile had a ballistic limit of 8 m/s; on the other hand, the sandwich structure with a 15.9 mm thick F40/5052-0.0019 Flexcore and of 2 x 1.58 mm thick 2024-0 A1 covers had a ballistic limit of 388 m/s.

Rubino et al. [30] investigated the impact response of the fully clamped, monolithic and sandwich plates of equal areal mass using metal foam projectiles. Monolithic plates, sandwich plates with Y-frame or corrugated cores were made from AISI 304 stainless steel material. The impact of the foam projectile created a momentum on the target and the momentum was altered by changing the impact

velocity. Furthermore, the permanent deflections and level of core compression of the sandwich plates were compared with those of simulations. At low projectile momentum, the sandwich plates outperformed the monolithic plates of equal mass. It was further found that the plates deflected less than the beams. The increase in the momentum acting on the sandwich constructions increased the permanent deflection over those of monolithic plates. In addition, Radford et al. [31] studied the dynamic response of the stainless steel end-clamped monolithic and sandwich austenitic stainless beams using the metal foam projectiles. The sandwich beams were made of stainless steel pyramidal, stainless steel corrugated and closed cell aluminum alloy metal foam cores. It was shown that sandwich beams deflected less than the monolithic beams because each had stretching resistance provided by the core. The deformation mechanism observed in the experiments was the travelling plastic hinges. The corrugated core and aluminum foam core sandwich beams showed the highest shock resistance followed by the pyramidal core sandwich beams and the monolithic beams.

CHAPTER 3

CHARACTERIZATION AND TESTING METHODS OF THE COMPOSITE, AL FOAM AND CORRUGATED AL

3.1. Introduction

The mechanical testing methods chosen for determining the response and characteristics of materials depend on the type of material and design considerations. Different types of testing methods were applied depending on the isotropic or anisotropic behavior of the materials. Furthermore, mechanical tests at different strain rates are usually applied to determine the response of materials and understand the deformation mechanisms and failure types at increasing high deformation rates. Quasi-static tests are usually conducted at a constant cross-head speed in the range of 10^{-3} to 10^{-1} s^{-1}; low velocity impact tests are performed using a drop weight testing machine at the strain rates between 1 to 100 s^{-1} and high strain rates tests are usually performed using a split Hopkinson pressure bar (SHPB) test setup at the strain rates between 100 and 10^{4} s^{-1}.Composite materials consist of two or more components having different properties; therefore, the properties vary with the properties of the individual constituent, fiber volume fraction, packing geometry and processing. All these make them difficult to characterize and develop an analytical model to fit the parameters. The fully characterization of composite materials requires diverse testing methods including tension, shear, compression, 3 point bending tests in three directions and off-axis tests.

3.2. Face Sheet and Corrugated Aluminum Processing

The corrugated structures including face sheets, interlayer sheets and core were made of 1050H14 and 3003H14 aluminum alloys. The corrugated structures were prepared using two methods. In the first method, the sandwich structure was prepared by bonding the individual layers (fin, interlayers and face sheets) using an epoxy glue. In the second method, the sandwich structure was prepared by brazing the individual

layers. 4343 Al alloy (6.8-8.2%) was used as the filler material in the brazing. Two types of sandwich structures were prepared and tested. In small fin corrugated aluminum sandwich structures, Figure 3.1(a) the face sheets and the interlayer sheets were made of 1050H14 Al alloy, while in big fin corrugated sandwich structures, the face sheets were made of 3003 Al alloy, Figure 3.1(b). In both structures, the fin type core was made of 1050H14 Al alloy sheet. The height of the fin is 4 mm in the small fin corrugated structure and 9 mm in big fin corrugated structure. The thicknesses of 1050H14 alloy in the small fin corrugated structure were 0.135mm in the fin, 0.5 mm in the interlayer and 2 mm in the face sheets. The thicknesses of 1050H14 alloy in the small fin corrugated structure were 0.135 mm in the fin and 0.5 mm in the interlayer and the thickness of 3003 Al face sheets was 2 mm. The small and big fin corrugated cores had an effective density of $\rho_{Smallfin} = 656kg/m^3$ and $\rho_{Bigfin} = 360kg/m^3$, respectively. The mechanical properties aluminum alloys used as face sheet, core, interlayer and filler material are tabulated in Table 3.1.

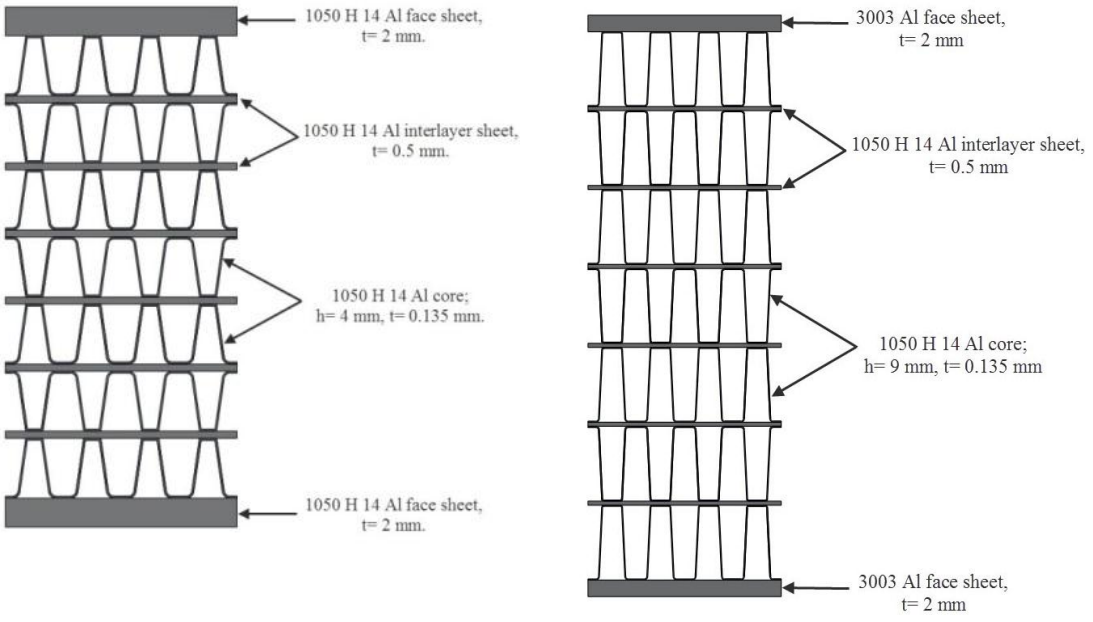

(a) (b)

Figure 3.1. Sketch of (a) small fin corrugated and (b) big fin corrugated Al structure.

Table 3.1. The mechanical properties of Al alloys used in sandwich manufacturing.

Material	**Density ρ (kg/m^3)**	**Elastic Modulus E (GPa)**	**Ultimate Tensile Strength σ_{UTS} (MPa)**	**Yield Strength σ_y (MPa)**	**Failure Strain (%)**	**Poisson's Ratio**
1050H14	2705	69	110	103	10	0.33
3003H14	2730	68.9	152	145	8	0.33
4343H14	2680	70	150	120	1	0.33

The trapezoidal corrugated aluminum layers used to construct core material in the sandwich structure are produced using a sheet folding process. The folding was accomplished using a paired punch and die tool to fold Al sheets into regular trapezoidal core resulting in a highly flexible core structure as seen in Figure 3.2.

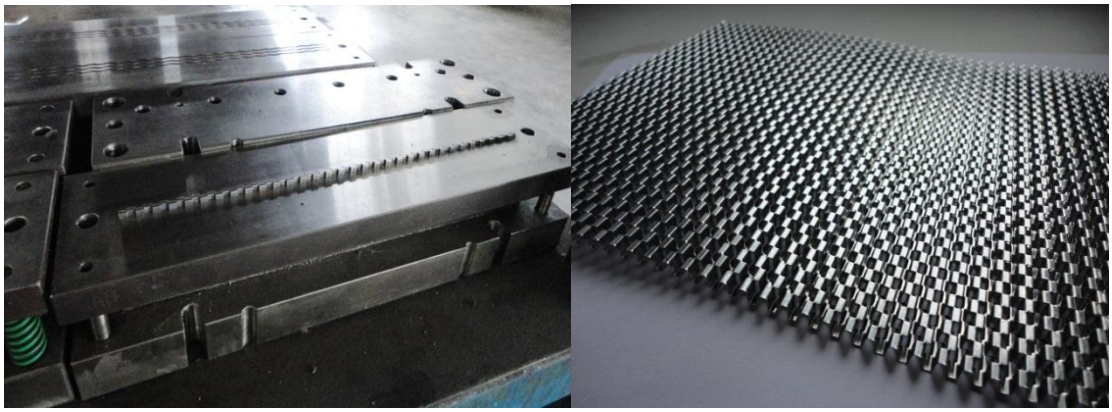

Figure 3.2. The punch and the corrugated sheet layer.

As stated earlier, Aluminum corrugated sandwich structures were assembled using an epoxy resin and through brazing of the core, interlayers and face sheets. Before brazing in the furnace, the assembly was cleaned to remove oils and lubricants as well as other contaminants on the surfaces. The cleaning procedure must allow for adequate flux re-tension and render the surfaces suitable for brazing. After cleaning, the flux slurry was sprayed on the assembly. The excess flux slurry was removed with air blow.

Then the assembly was placed in a furnace for brazing in air at 600^0C± 5^0C ideally uniform temperature for 10 minutes. Figure 3.3 shows the picture of one of the sandwich panels after brazing.

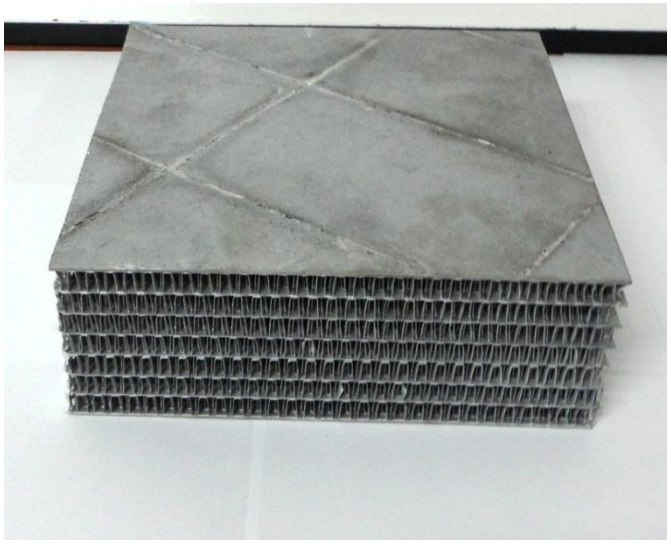

Figure 3.3. A corrugated aluminum core sandwich panel produced by brazing.

3.3. Material Preparation

E-glass/polyester composite plates were produced by vacuum assisted resin transfer molding (VARTM).The reinforcement was Metyx$[0°/90°]_s$ E-glass biaxial fibers and the polyester resin was CRYSTIC 703 PA. Methyl ethyl ketone peroxide (MEKP) was used as hardener with 2 wt. %. The composite plates with thicknesses of 2, 3 and 5mm were prepared with $[0°/90°]_s$ and $[\pm 45°]_s$ fiber orientations. In all composite plates prepared, the fiber volume content was assumed nearly 0.6. The number of fiber plies needed to obtain an intended thickness was calculated using the following relation,

$$d = \frac{n \cdot A_w}{\rho_f \cdot V_f} \tag{3.1}$$

where, d is the thickness of the plate, n is the number of plies; A_w is the areal weight of the fibers, ρ_f is the density of the fiber and V_f is the fiber volume fraction. The weight of the polyester was calculated using the following relation,

$$M_p = (\rho_m \cdot V_p) \cdot V_m \tag{3.2}$$

where, M_p is the weight of polyester, ρ_m is the density of the polyester, V_p is the volume of the plate and V_m is the volume fraction of the matrix in the composite plate.

The used infusion process set-up is shown in Figure 3.4. The vacuum infusion process was performed on a glass plate. Initially, a thin layer of wax layer was deposited on the glass plate surface for the easy separation of the composite plate from the glass plate. Then the fiber plies were sequentially placed on the glass plate. The fibers were covered with tear-off tissue and then draining tissue was place on tear-off tissue. Additional fiber plies were placed on the tear-off tissue to slow down the flow of the resin. Then, vacuum ramps and resin ramps were placed and gutta (sealtex) was applied peripheral to the fibers. Vacuum bag was cut in suitable dimensions and installed for forming a good vacuum over the fiber plies. Vacuum pipes were connected and the vacuum was checked against a leakage.

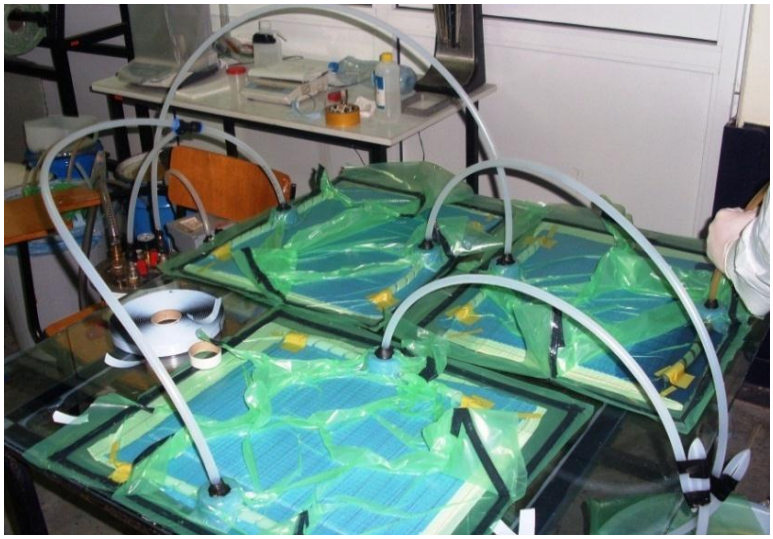

Figure 3.4. Vacuum infusion set-up.

Aluminum closed cell foam core composite sandwich structures were also prepared using a modified VARTM method to satisfy a good resin transfer. There was a height difference between resin ramp and top face of the sandwich structure and the problem was solved applying a second resin ramp to the VARTM set-up as seen in Figure 3.5. Although the flow rate on top surface was lower with respect to the bottom surface, the fibers were wetted with resin successfully. Foam cores were supplied from

Alulight in two densities; 297 kg/m^3 and 405 kg/m^3 corresponding to 0.11 and 0.15 relative densities and in a thickness of 30 mm. Totally, 18 composite sandwich structures with Al foam cores were prepared in 200 mm x 200 mm cross-section. Composite plates of $[\pm 45°]_s$ fiber orientation and 2, 3 and 5 mm in thickness were used as the face sheet of aluminum closed cell foam core. The thicknesses of sandwich plates prepared were 34 mm, 36 mm and 40 mm. The prepared sandwich structures with 2, 3 and 5 mm thick composite skins are shown in Figure 3.6.

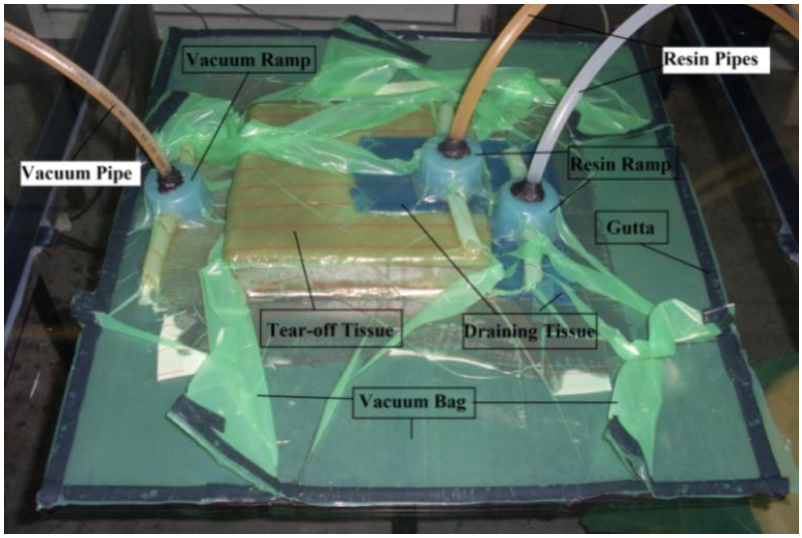

Figure 3.5. Modification of the VARTM method.

Figure 3.6. Sandwich structures with aluminum foam core.

The corrugated aluminum core composite sandwich structures were prepared by gluing the corrugated layers on the composite plate using an epoxy resin. In order to

increase the adhesion area and to keep the corrugated structures rigid 0.3 mm Al sheet interlayers were inserted between the layers. This sequence of operations was applied until 6 corrugated layers were obtained. Finally, the second composite face skin was stuck on the last corrugated layer. The assembly was kept under 20 kg weight for 2 h. The corrugated aluminum core composite sandwich structure with 5mm face plates is shown in Figure 3.7.

Figure 3.7. Corrugated aluminum core composite sandwich.

3.4. Materials Testing

The tension test samples of E-glass/polyester composite material in $[0°/90°]_s$ fiber orientation were prepared in accord with ASTM 3039M test specimen geometry with end tabs. Furthermore, whole tests are conducted through the principle directions 1, 2 and 3 (Figure 3.8). The test samples were machined to a width of 25 mm, a thickness of 2 mm and a length of 175 mm for 90° orientation. The test samples for 0° orientation were 15 mm in width, 250 mm in length and 1.5 mm in thickness. The end tab thickness was 1.5 mm, the tab length was 25 mm for 90° and 56 mm for 0° orientation and the tab bevel angle was 90°. The balanced and symmetric specimen geometry was also used in the tests because of the biaxial fiber. The width of the specimens was 25 mm, the length of the specimens was 250 mm and the thickness was 2.5 mm for the balanced and symmetric samples. The tolerances for the specimen width and tab thickness were kept in ±1% of the recommended dimensions; the tolerance for the thickness of the specimen was satisfied in ±4% of the recommended thickness. The tabbing material was E-glass/Polyester composite in the same orientation with the

composite specimen and the adhesive used to glue end tabs was two component BISON epoxy. The specimens used through thickness tension test were 125 mm in length, 25 mm in width and 2 mm in thickness and the infusion process for specimen preparation for $[0°/90°]_s$ and $[\pm 45°]_s$ orientation can be seen in Figure 3.9. All the samples were cut from plates using a hand held rotary tool, as seen in Figure 3.9, except the through thickness samples. During machining, precautions were taken against notches, undercuts, rough and uneven surfaces and delaminations caused by inappropriate machining.

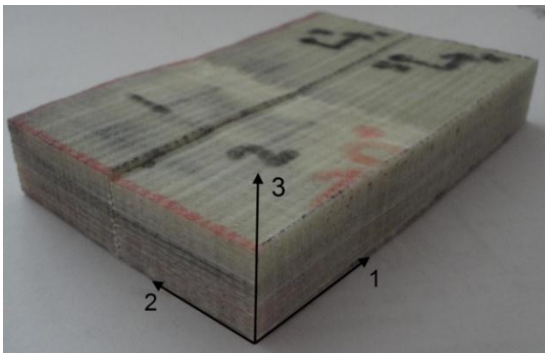

Figure 3.8. Test directions of composite samples.

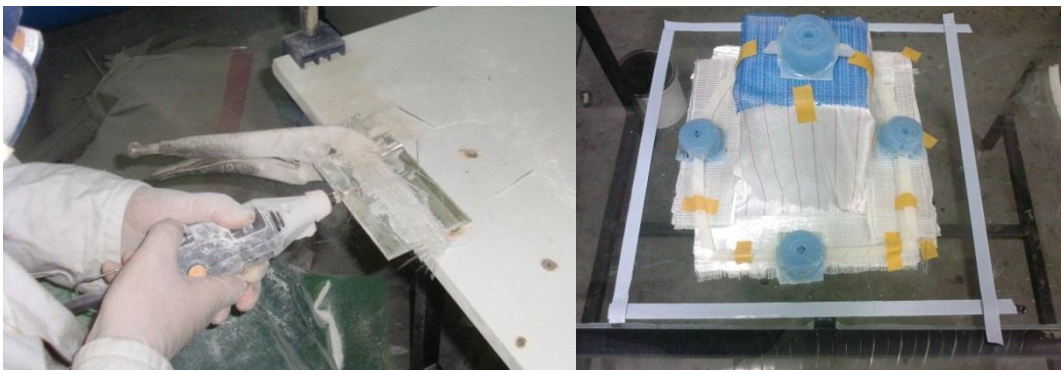

(a) (b)

Figure 3.9. (a) Sample cutting by hand held rotary tool and (b) through thickness sample preparation by VARTM method.

The tension tests were performed using Shimadzu universal testing machine at a crosshead speed of 2 mm/min. Strain gages were fixed on the sample to determine the Poisson's ratio of the composite plates in all directions (Figure 3.10). A video extensometer was used to record the longitudinal strain and strain gages were used for recording the transverse strain. Strain gages (MM, 350 ohm resistance and 2.09 gage

factor) were conditioned by a signal conditioner. A 10V excitation voltage and 20 gain were applied by the signal conditioner. The conditioned signal was transferred to the oscilloscope to monitor and record the signal. The signal conditioner and oscilloscope used in the experiments are shown in Figure 3.11. The voltage difference was translated into strain using following relation,

$$\varepsilon(t) = \frac{4 \times Voltage(t)}{V_{excitation} \times Gage_{factor} \times Gain} \tag{3.3}$$

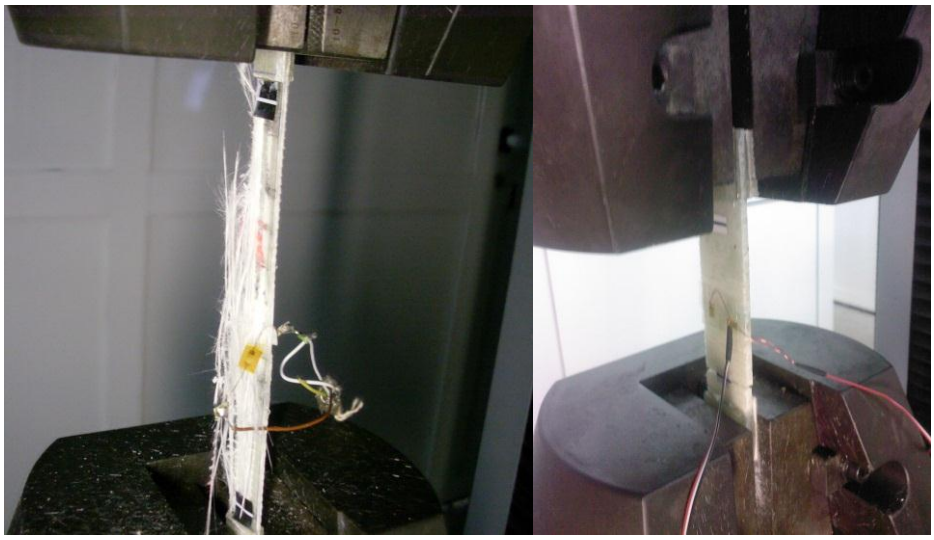

Figure 3.10. Strain gage and video extensometer marker on tested composite specimens.

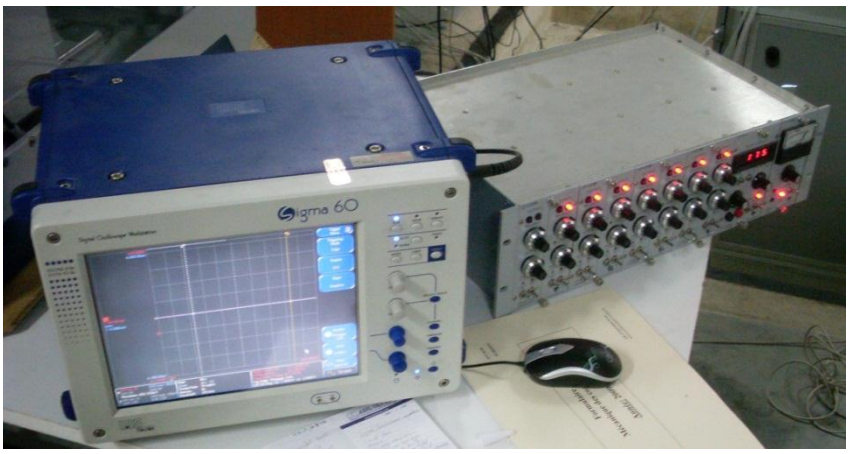

Figure 3.11. Oscilloscope on the left and signal conditioner on the right.

The material properties obtained after the tensile tests are;

- Young's modulus in the fiber direction, E_1.
- Young's modulus in the transverse to the fiber direction, E_2.
- Young's modulus in the through thickness direction, E_3.
- Ultimate tensile stress and strain in the fiber direction, X_1^T, ε_1^T.
- Ultimate tensile stress and strain transverse to the fiber direction, X_2^T, ε_2^T.
- Ultimate tensile stress and strain in the through thickness direction, X_3^T, ε_3^T.
- Poisson's ratio, $\nu_{21}, \nu_{31}, \nu_{32}$.

Off-axis tension test specimens with fiber orientation of 30° and 60° were cut from the composite plates having the same fiber orientation. The off-axis test specimens were 229 mm long, 12.7 mm wide and 1.5 mm thick. The objective of the off-axis tension test is to verify and check the validity of the ply properties determined in the previous characterization tests and obtain the ultimate tensile strength of off-axis composite orientation based on Tsai-Wu criterion. The tensile strength of the off-axis tensile coupon is a function of the off-axis angle. The state of stress in the fiber coordinate system as a function of angle may be obtained from the following equation,

$$\begin{bmatrix} \sigma_1 \\ \sigma_2 \\ \tau_{12} \end{bmatrix} = \sigma_x \begin{bmatrix} m^2 \\ n^2 \\ -mn \end{bmatrix} \tag{3.4}$$

where, $m = \cos\theta$ and $n = \sin\theta$, so the state of stress in the fiber coordinate system is biaxial. In Tsai-Wu criterion, tensile and compressive strengths are assumed to be equal and $F_{12} = -1/[2(X_1^T)^2]$. The Tsai-Wu criterion reduces to the Tsai-Hill criterion as [32],

$$\frac{\sigma_1^2 - \sigma_1\sigma_2}{(X_1^T)^2} + \left(\frac{\sigma_2}{X_2^T}\right)^2 + \left(\frac{\tau_{12}}{S_6}\right)^2 = 1 \tag{3.5}$$

substituting σ_1, σ_2 and τ_{12} in Equation 3.4 into Equation 3.5 gives the expression for the tensile strength of the off-axis coupon as,

$$\sigma_x^{ult} = \left[\frac{m^4 - m^2 n^2}{(X_1^T)^2} + \frac{n^4}{(X_2^T)^2} + \frac{m^2 n^2}{(S_6)^2} \right]^{-1/2} \tag{3.6}$$

The test procedures for off-axis tensile tests were the same with the uniaxial tensile tests. The samples were gripped and pulled with a crosshead speed of 2 mm/min until the failure. Only longitudinal strain was recorded with video extensometer.

Shear test samples were prepared according to ASTM 3518 test standard. This test standard also recommends ASTM 3039M test specimen geometry for shear tests. The test was used to determine shear modulus and shear strength of a composite material. The width, length and thickness of the shear test specimen were sequentially 25, 250 and 2.5 mm. The tabs used in these tests were 56 mm in length and 1.5 mm in thickness and the tab bevel angle was 90°. The response of the composite material to shear force is generally nonlinear. For this reason, full characterization is needed for stress-strain values. A region of pure, uniform shear stress should be provided for a proper shear test. The major difficulty in shear tests is attaining a uniform state of pure shear stress in the test section. In this study, to satisfy a pure and uniform shear region $[\pm 45]_{ns}$ ($n \geq 2$) tension test was used. The geometry for the $[\pm 45]_{ns}$ tensile coupon has the same geometry as ASTM D3039 tension test. The $[\pm 45]_{ns}$ tension test provides an indirect measure of the in-plane shear stress-strain response in the fiber coordinate system. In the tests, the tensile test coupon was instrumented with two strain gages; one of them was located in the fiber direction and the other one was transverse to the fiber direction. The specimen was tested in tension until failure with a crosshead speed of 2 mm/min. Using laminated plate theory τ_{12} is given as,

$$\tau_{12} = \sigma_x / 2 \tag{3.7}$$

where, σ_x is the axial stress and the shear strain is found using following relation,

$$\gamma_{12} = \varepsilon_x - \varepsilon_y \tag{3.8}$$

where, ε_x and ε_y are the axial and transverse strains, respectively. The slope of shear stress vs. strain curve gives the shear modulus, G_{12}. The ultimate shear stress, S_6, is defined as the maximum value of $\sigma_x / 2$.

Cylindrical compression test samples (Figure 3.12) were prepared for both $[0°/90°]_s$ and $[\pm 45°]_s$ fiber orientations using a core drill machine and a high precision saw. The samples were drilled from 18 mm thick $[0°/90°]_s$ and $[\pm 45°]_s$ composite laminates. The cylindrical compression test samples were 9.81 mm diameter and satisfied length to diameter ratio of 1.5. The precision saw machining was used to obtain parallel and high quality surfaces. Compression tests were conducted in all directions at 10^{-3}, 10^{-2} and 10^{-1} s^{-1} strain rates. The crosshead speed was calculated using known values of specimen length and strain rate by the following equation,

$$V_{Cr} = \dot{\varepsilon} \times L_0 \tag{3.9}$$

where, V_{Cr} is the crosshead speed in mm/s, $\dot{\varepsilon}$ is the strain rate in s^{-1} and L_0 is the initial length of the specimen. Material properties obtained from the compression test are;

- Young's modulus in the fiber direction, E_1.
- Young's modulus in the transverse to the fiber direction, E_2.
- Young's modulus in the through thickness, E_3.
- Ultimate compressive stress and strain in the fiber direction, X_1^C, ε_1^C.
- Ultimate compressive stress and strain transverse to the fiber direction, X_2^C, ε_2^C
- Ultimate compressive stress and strain in the through thickness, X_3^C, ε_3^C

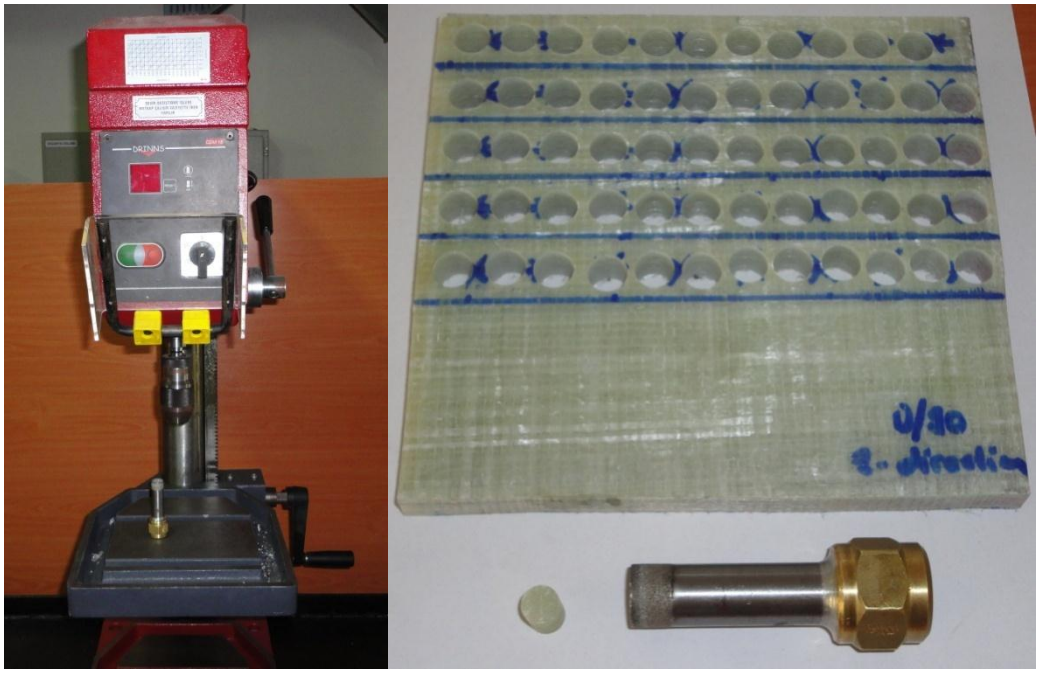

Figure 3.12. Core-drilled compression test sample.

Flexure tests (3-point bending tests) were conducted on $[0°/90°]_s$ fiber oriented composite samples using the bending test fixture shown in Figure 3.13. The span to thickness ratio (L/h) was chosen 16 based on the ASTM D790-92. The diameter of the load noses and support pins should be at least 6.4 mm according to the specification so a load nose with 10 mm diameter was used to conduct tests. Specimens were nominally 130 mm long and 12.7 mm wide. In flexure test the top side of the specimen is under compression while the bottom side is tension. The mid-plane contains the neutral axis and is under zero bending stress. The interlaminar shear stress is maximum at the beam center [33]. The stress level is dependent on the span to thickness ratio (L/h).

Beams with a small L/h ratio are dominated by shear. Figure 3.14 shows the flexural test specimen. At least five specimens from each thickness were tested using Shimadzu uniaxial testing machine with a crosshead speed of 2 mm/min. Force and deflection were recorded and the strength was calculated using,

$$\sigma = \frac{3PL}{2wh^2} \tag{3.10}$$

where, P is the applied load, L is the span length; h is the thickness of the beam and w is the width of the beam. The strain at the mid-span of the beam is calculated as,

$$\varepsilon = 6Dh / L^2 \tag{3.11}$$

where, ε is the strain of the fibers and D is the deflection of the beam. The flexural modulus, E_f is calculated using the following equation,

$$E_f = \frac{mL^3}{4wh^3} \tag{3.12}$$

where m is the slope of the load-deflection curve.

Figure 3.13. Adjustable 3-point bending test fixture.

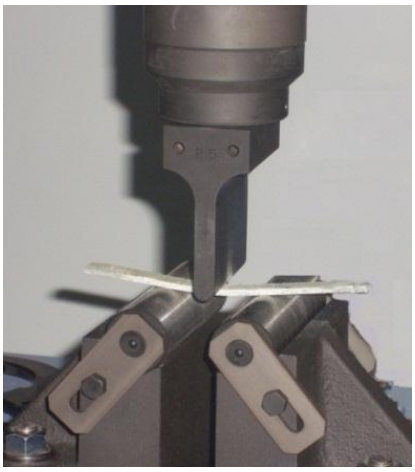

Figure 3.14. Flexural test specimen

ASTM D2344M standard short beam shear test method (Figure 3.15) was used to determine the interlaminar shear strength of composite. The specimens, 110 mm in length, 18 mm thick and 36 mm in width, were cut from the composite plates. Specimen length to thickness ratio was 6 and width to thickness ratio was 2. The span to measured thickness ratio was 4±0.3 mm. The crosshead speed was taken as 1 mm/min according to ASTM D2344M standard.

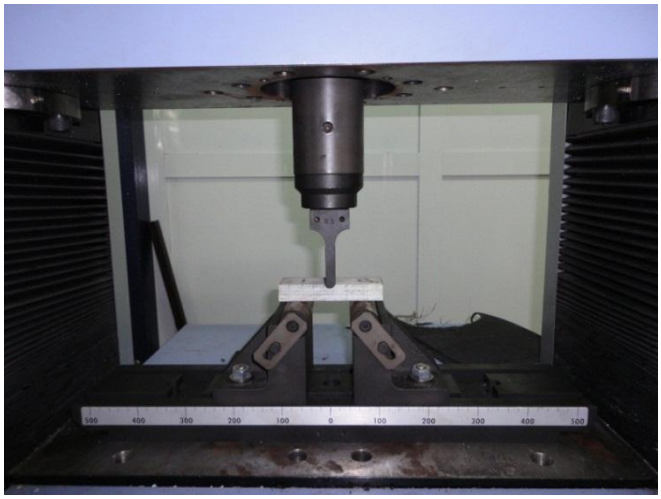

Figure 3.15. Interlaminar shear test on short beam

The specimen was inserted into the test fixture with the tools resting on the reaction supports. The specimen was aligned and centered such that its longitudinal axis was perpendicular to the loading nose and side supports. The span length was adjusted according to the span to measured thickness ratio of 4. The loading nose (5R) was located equidistant between the side supports. Finally, the crosshead speed was set to 1 mm/min and the results were recorded simultaneously during the test and the interlaminar shear strength, τ_{max} , was found by the Equation 3.13;

$$\tau_{max} = \frac{0.75 \cdot P}{wh} \tag{3.13}$$

where P is the force, w and h are width and thickness of the specimen, respectively.

The fiber volume fraction of the prepared composite plates was determined through burn-off method. Samples with 50 mm width and 50 mm length were cut from

both $[0°/90°]_s$ and $[\pm 45°]_s$ composites with 2 mm, 3 mm and 5 mm thicknesses. The used ceramic crucibles and samples after the burn-off are shown in Figure 3.16. The ceramic crucibles were weighted and their masses were recorded as M_1 and then the composite specimens were placed into the ceramic crucibles and weighted and recorded as M_2. Then the ceramic crucibles within composite samples placed into the oven at a temperature of 625°C and the samples were kept for 30 minutes until the resin completely removed. After cooling, the ceramic crucibles with fibers were weighted and recorded as M_3. The mass of the fiber (m_f) and matrix (m_m) were calculated using the following relations,

$$m_f = M_3 - M_1 \tag{3.14}$$

$$m_m = M_2 - M_3 \tag{3.15}$$

The fiber volume fraction (V_f) was calculated using the following relation;

$$V_f = \frac{V_f'}{V_f' + V_m'} = \frac{\left(\frac{m_f}{\rho_f}\right)}{\left(\frac{m_f}{\rho_f} + \frac{m_m}{\rho_m}\right)} \tag{3.16}$$

where, V_m and V_f are the matrix and fiber volume, respectively and ρ_m and ρ_f are the matrix and fiber density, respectively.

Figure 3.16. Ceramic crucibles and fibers after burn-off process.

Drop weight tests and projectile impact tests were performed on $[0°/90°]_s$ and $[\pm 45°]_s$ fiber oriented composite plates. Drop weight test specimens were 100 mm long, 100 mm wide and 2 mm, 3 mm and 5 mm thick (Figure 3.17). All the samples were cut from the prepared composite plates using a jig saw. The specimens for projectile impact test were 200 mm long, 200 mm wide and 2 mm, 3 mm and 5 mm thick.

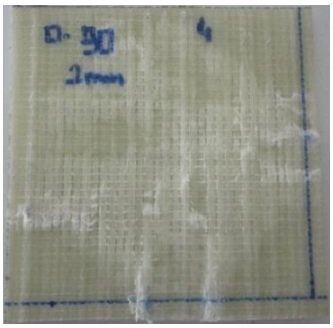

Figure 3.17. Drop weight test specimen.

3.5. Aluminum Foam and Corrugated Aluminum Structures Testing

Compression tests were conducted on aluminum foam specimens (relative densities of 0.11 and 0.15) and corrugated aluminum specimens produced by brazing and using epoxy. The aluminum foam compression specimens with dimensions of 50 mm in length, 50 mm in width and 30 mm in thickness (Figures 3.18 (a) and (b)) were cut using a jig saw.

(a) (b)

Figure 3.18. Aluminum foam samples (a) 0.11 and (b) 0.15 relative density.

Both big fins and small fins corrugated sandwiches were prepared through brazing, while only big fin corrugated sandwich specimens were prepared using epoxy (Figures 3.19 (a) and (b)). The compression big and small fin corrugated test specimens were sequentially 50 mm in length, 50 mm in width and 70 mm in thickness and 50 mm in width, 50 mm in length and 32 mm in thickness. Compression tests were conducted using Shimadzu uniaxial testing machine with a strain rate of 10^{-3} s^{-1}. At least 3 compression tests were performed for each sample.

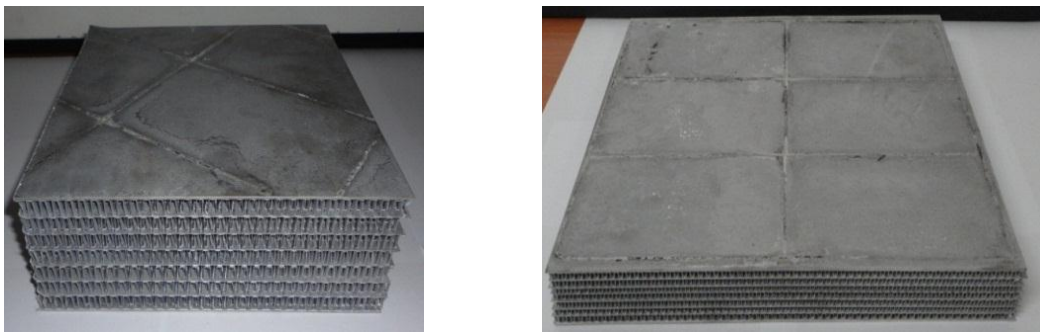

(a) (b)

Figure 3.19. (a) Big and (b) small fin corrugated aluminum core sandwich structures.

3.6. Low Velocity Impact Tests

The low velocity impact tests were conducted using a FRACTOVIS drop weight tower (Figure 3.20). The equipment consists of striker holder which accommodates additional weights, striker and the 20 mm diameter hemispherical impactor (Figure 3.21). The impactor is attached to the tip of the 90 kN capacity piezoelectric force

transducer. The weights are added to alter the impact energy. The velocity of the impact is measured by a photocell device which is placed in the path of the striker before the impactor strikes to the specimen. The force-time history is measured from the point of initial contact with the specimen and the striker travels through the thickness of the specimen. Energy is calculated from integration of the force-time signal. The load-displacement, force-time and energy-time history are some of the parameters that were recorded by Data Acquisition System (DAS) (Figure 3.22). Totally 16000 points were recorded in a test. Sampling frequency was 1000 kHz with 16 ms of test duration. The data acquisition system is represented in.

Figure 3.20. FRACTOVIS low velocity impact test equipment.

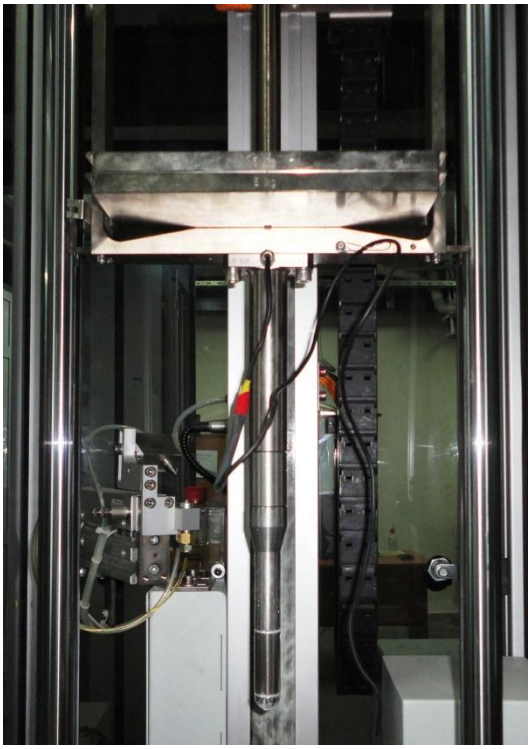

Figure 3.21. Striker holder, weights and the impactor.

Figure 3.22. Data Acquisition System

In composite material's low velocity impact tests a total weight of 15.78 kg was used. Drop height changed during the test because of the variable impact velocity and in some tests additional energy system was used to reach the desired impact velocity. Impact velocities were between 4 m/s and 10 m/s which include both rebound and perforation mechanism velocities. For the impact conditions where the striker rebounds from the specimen, multiple impacts can occur which cause excessive damage that is not a single impact condition. To avoid repeated impacts, two rebound arrestors are

located on both side of the specimen. The rebound arrestors are pneumatically actuated, and spring up and separate the striker from the specimen after the first impact. The arrestors and the anti-rebound system are shown in Figure 3.23.

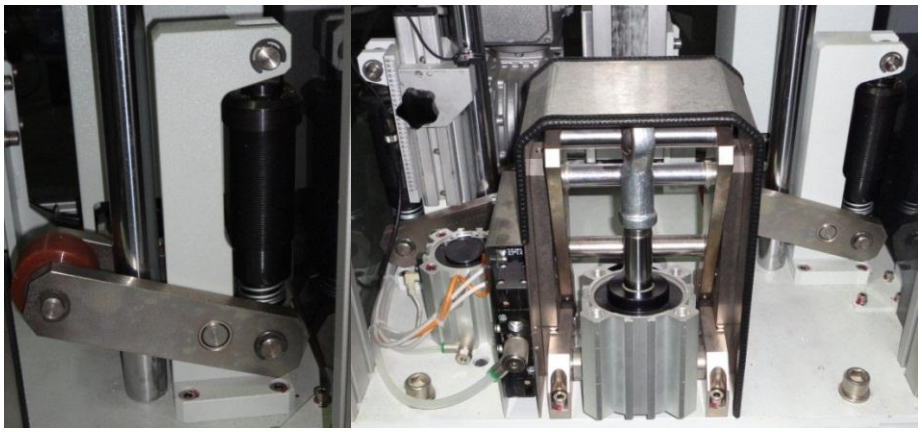

Figure 3.23. The arrestors and the anti-rebound system.

The composite low velocity impact test samples were in 100 mm x 100 mm dimension and 2 mm, 3 mm and 5 mm thicknesses for $[0°/90°]_s$ and $[\pm45°]_s$ fiber orientations. The specimen was fixed in a fully clamped support condition with a 76.2 mm diameter hole that allowed the impactor to strike the specimen. The applied clamping force on the specimen was 75 N to avoid rotation and sliding of the specimen at the impact instant.

Various properties can be obtained from low velocity impact tests: impact velocity and incipient energy (E_i), total energy absorbed (E_t), total deflection (I_t), incipient damage point (P_i), maximum load (P_{max}), failure load point, total load point (P_t), energy at maximum load (E_m), deflection at maximum load (I_m) and energy ($E_p=E_t-E_m$) and deflection ($I_p=I_t-I_m$) after maximum load [34]. A typical low velocity impact load-time curve is shown in Figure 3.24 with the determined properties. The point of incipient damage (P_i and E_i) is the first significant deviation or break from the initial portion of the load-time curve. This point shows the onset delamination, matrix micro-cracking or fiber damage. At the point of maximum load and maximum energy, maximum penetration of the impactor occurs and then the rebound begins. In some cases, the incipient damage point coincides with the maximum load. The failure load and energy points indicate the specimen response up to the end of the rebound phase of the impactor. These parameters can be influenced by material thickness and geometry,

boundary conditions, progression and sequence of damage accumulation, fiber orientation, interface variations and impactor geometry (sharp, blunt, and spherical). It should be noted that the heterogeneous and anisotropic nature of the fiber reinforced composites cause the different types of failure modes including (1) matrix cracking due to tension, compression or shear; (2) delamination between the plies because of the interlaminar shear stress; (3) fiber break and buckling; (4) penetration.

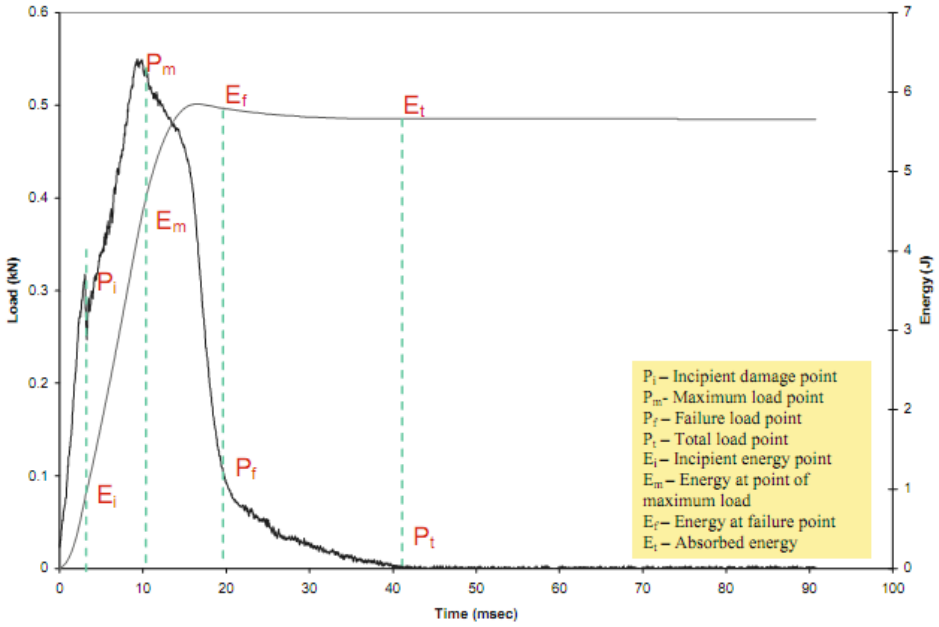

Figure 3.24. A typical load-energy-time curve for impact analyses. (Source: Abrate, 2011)

3.7. Split Hopkinson Pressure Bar Testing

The common method of determining the material properties at high strain rates is the split Hopkinson pressure bar testing. The strain rate that can be reached in split Hopkinson pressure bar is usually between 100 s^{-1} and 10^4 s^{-1}. The maximum strain rate that can be obtained from the split Hopkinson pressure bar test varies inversely with the length of the test specimen. The maximum strain rate is also limited by the elastic limit of the Hopkinson bars that are used to transmit the stress pulse to the test sample.

In the split Hopkinson pressure bar test, a short cylindrical specimen is sandwiched between long bars, as shown in Figure 3.25. Generally, a striker bar is fired into the end of the input bar generating a compressive pulse (Incident pulse). This

compressive pulse travels along the input bar towards the specimen-input bar interface where a portion of the pulse is reflected into the input bar and the other portion is transmitted through the output bar. The reflected pulse is reflected as a tension wave and the transmitted pulse remains in compression.

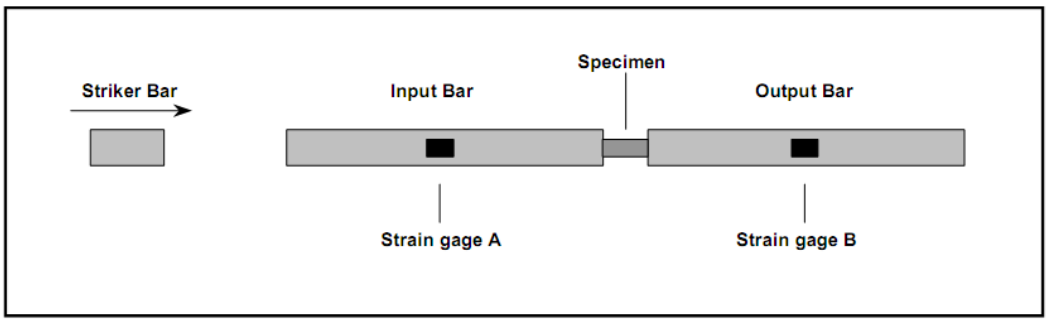

Figure 3.25. Schematic representation of split Hopkinson pressure bar apparatus. (Source: Kaiser, 1998)

The yield strength of the selected pressure bar material determines the maximum stress achieved within the deforming specimen while the pressure bars should remain elastic. Inconel bars are preferred at elevated temperature Hopkinson bar testing as it retains its mechanical properties up to 800°C. The length, l and diameter, d, of the Hopkinson bars are chosen to meet some requirements to satisfy test validity as well as maximum strain rate and strain level in the sample. For a given pulse duration, the length of the bars must first ensure the one dimensional wave propagation and to fulfill this propagation 10 bar diameters are required. Length to diameter ratio of 20 should be exceeded for each bar, to separate the incident and reflected waves for data reduction. Furthermore, the maximum strain rate desired will influence the selection of the bar diameter because the highest strain rate tests require the smallest diameter pressure bars. The amount of total strain that will be imparted to the specimen also affects the bar length; the magnitude of the strain depends on the length of incident wave. The pressure bar must be at least twice the length of the incident wave if the incident and reflected waves are to be recorded without interference. When the deformation is pure elastic then the longitudinal wave velocity (C_0), is given by,

$$C_0 = \sqrt{\frac{E}{\rho}} \tag{3.17}$$

where, E is the elastic modulus and ρ is the density of the bar. If the deformation is in the plastic region, the plastic wave velocity (C_p) is given as,

$$C_p = \sqrt{\frac{d\sigma / d\varepsilon}{\rho}} \tag{3.18}$$

where, $d\sigma / d\varepsilon$ is the slope of the true stress-true strain curve. For many materials, the slope is approximately 1% of the elastic modulus; thus the plastic wave velocity is approximately 10% of the elastic wave velocity.

A typical pulse recorded from a composite material high strain rate test is shown in Figure 3.26. Incident, reflected and transmitted strains measured from strain gages on the bars are ε_I, ε_R and ε_T, respectively. The average stress on the specimen is calculated by taking the average of the forces, $F_1(t)$ and $F_2(t)$, on both sides of the specimen (Figure 3.27) as,

$$F_{avg}(t) = \frac{F_1(t) + F_2(t)}{2} \tag{3.19}$$

The forces in terms of the strains are,

$$F_1(t) = E \cdot [\varepsilon_I(t) + \varepsilon_R(t)] \cdot \frac{\pi D_{BAR}^{\ 2}}{4} \tag{3.20}$$

$$F_2(t) = E \cdot \varepsilon_T(t) \cdot \frac{\pi D_{BAR}^{\ 2}}{4} \tag{3.21}$$

Substituting Equations 3.20 and 3.21into the Equation 3.19 gives the average stress as,

$$\sigma_{avg}(t) = \frac{\pi D_{BAR}^{\ 2}}{2} \cdot E \cdot [\varepsilon_I(t) + \varepsilon_R(t) + \varepsilon_T(t)] \tag{3.22}$$

The strains on the incident and transmitter bars are taken equal as,

$$\varepsilon_I(t) + \varepsilon_R(t) = \varepsilon_T(t) \tag{3.23}$$

Then, the average stress on the specimen is,

$$\sigma_{AVG}(t) = \frac{D_{BAR}^{\ 2}}{D_S^{\ 2}} \cdot \varepsilon_T(t) \tag{3.24}$$

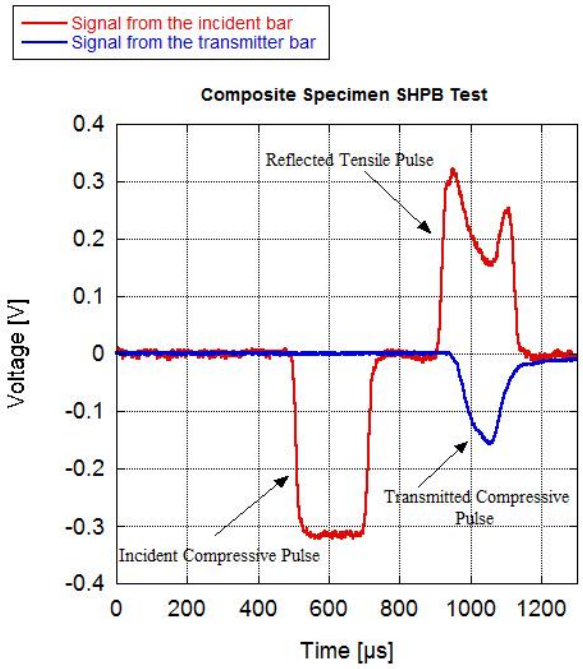

Figure 3.26. A typical voltage versus time response recorded form SHPB test.

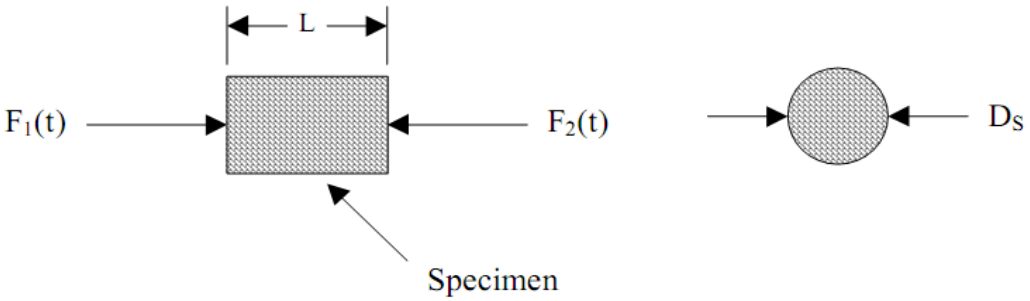

Figure 3.27. Cylindrical specimen and forces acting on the specimen.
(Source: Kaiser, 1998).

The strain rate in the specimen is,

$$\frac{d\varepsilon}{dt} = \frac{V_1 - V_2}{L} \tag{3.25}$$

where, L is the specimen length and$V_1$and V_2 are the velocities at the incident bar/specimen and specimen/transmitter bar interfaces, respectively. The velocity V_1 is the product of the longitudinal wave velocity, C_0 and $\varepsilon_I - \varepsilon_R$ ($V_1 = C_0 \cdot (\varepsilon_I - \varepsilon_R)$). Similarly, the velocity V_2 is equal to the product of C_0 and the transmitted strain ($V_2 = C_0 \cdot (\varepsilon_T)$). Then, the strain rate in terms of strains is expressed as,

$$\frac{d\varepsilon(t)}{dt} = \frac{C_0}{L}[\varepsilon_I(t) - \varepsilon_R(t) - \varepsilon_T(t)] \tag{3.26}$$

By taking uniform deformation, then the above equation is simplified as,

$$\frac{d\varepsilon}{d_t} = -\frac{2 \cdot C_0 \cdot (\varepsilon_R)}{L} \tag{3.27}$$

The integration above gives the specimen strain as,

$$\varepsilon_S(t) = \frac{-2 \cdot C_0}{L_S} \cdot \int \varepsilon_R(t) dt \tag{3.28}$$

The cylindrical test samples used in the tests were 9.81 mm in diameter and 14.715 mm in length with an l/d ratio of 1.5. A thin grease layer was applied on both interfaces of the bars before the cylindrical samples were sandwiched between the incident and transmitter bars to minimize the frictional forces. The SHPB apparatus used consists of Inconel 718 bars, 500 mm striker, 3116 mm incident and 2080 mm transmitter bars, all with a diameter of 19.35 mm. In Figure 3.28, the sample, incident bar and transmitter bar configuration for testing is shown. A full bridge strain gage was used to measure the strains on the Inconel bars. The distance between the interface of

the bar and the strain gage was 1010 mm. The signals measured by the strain gages were conditioned with a signal conditioner and the voltage versus time records were monitored by a digital oscilloscope. A high speed camera, 5000 frames/sec, was used to record the split Hopkinson pressure bar tests.

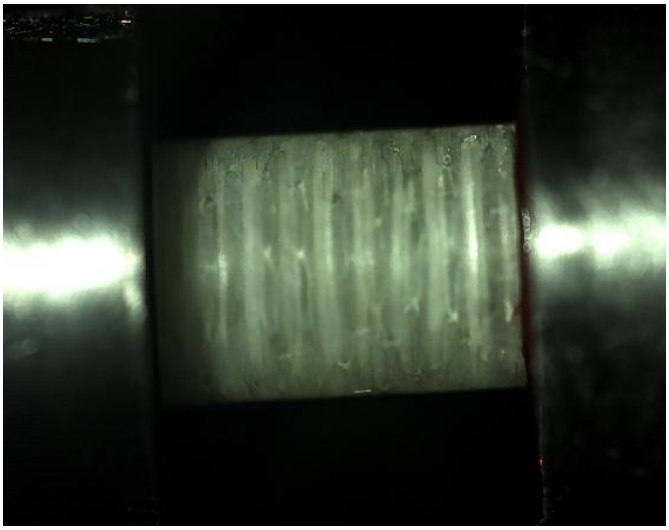

Figure 3.28. Incident bar, transmitter bar and composite sample prior to impact.

3.8. Projectile Impact Testing

The projectile impact tests were applied on 0°/90° and ±45° fiber oriented E-glass/polyester composite plates with different thicknesses, aluminum foam core composite sandwich structures, corrugated aluminum core composite sandwich structures, corrugated aluminum core aluminum sandwich structures and aluminum foam plates. The gas gun assembly used in the test is shown in Figure 3.29. The assembly consisted of pressure vessel, specimen holder and velocity measurement devices.

The pressure vessel was filled with air using an air compressor which operated at maximum 6 bar. The maximum inflate pressure obtained from the system is 5 bar because of the air leakage in pipes. The air pressure inside the pressure vessel was measured by two manometers which are installed directly on the pressure vessel. A hardened steel sphere with 30 mm in diameter and 110 g in weight was used as the projectile (Figure 3.30 (a)). In order to guide the projectile, a sabot (18 g) was produced

from polyurethane foam by injection into a specific mold (Figure 3.30 (b)). One of the two sabot sides included a center hollow in the shape of the projectile in order to house the projectile. The other side of the sabot was conical to provide a concentrated air flow allowing the acceleration of the sabot. An anvil was used at the exit side of six meter canon to stop the sabot. At the exit side, the sabot impacted the anvil and the steel ball projected through the target.

Figure 3.29. Overview of the projectile impact test setup.

(a) (b)

Figure 3.30. (a) Spherical steel projectile and (b) sabot.

The target holder was made of steel (Figure 3.31) and the target were clamped between the two thick steel plates using bolts. The center of the barrel pointed the center of the target. The specimen dimensions varied between 150 mm and 230 mm. Two laser

barriers were used to measure the velocity of the projectile. Both laser barriers consisted of two laser beam columns to measure the velocity. One of them was located close to the anvil and before the specimen holder, which measured the impact velocity (Figure 3.32 (a)) and the other was located back of the specimen holder, which was mounted at the back face of square steel plates (Figure 3.32 (b)).

Figure 3.31. Specimen holder.

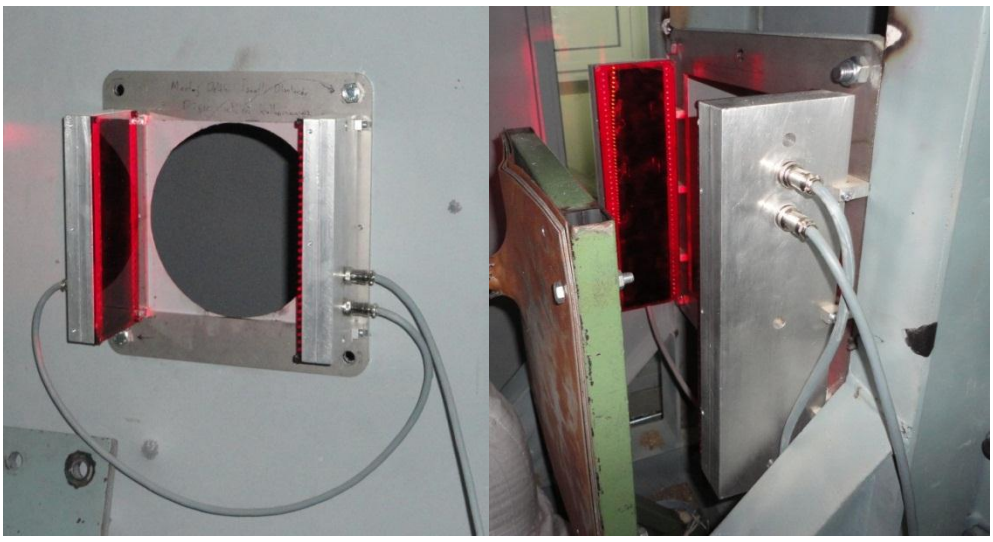

(a) (b)

Figure 3.32. Laser barrier (a) before the specimen holder and (b) back of the specimen holder.

A high speed video camera was used to record the impact and the motion of the projectile after the penetration. The specimen housing contained two polycarbonate windows, one was located on the top and the other was on the right hand side of the housing. These windows allowed recording the projectile motion before and just after the impact. The camera was controlled by the trigger system in the laser barriers control unit. When the projectile passed through the first laser barrier, the system sent a signal to the camera and then it started to record automatically. The images were taken at 5000 frames/s and recorded as both photo and video format. The high speed camera images were also used to measure the impact and residual velocities.

The composite targets were cut in 200 mm x 200 mm plates of $[0°/90°]_s$ and $[\pm 45°]_s$ fiber oriented composite laminates. Three different thicknesses; 2 mm,3 mm and 5 mm for both orientations were tested at the same pressure. The projectiles were 30 mm diameter hardened steel spheres and their mass was 110 g. The impact velocity was in the range of 127 m/s to 190 m/s and all the impacts were normal impacts.

Five different sandwich structures were tested at the same impact velocities and projectile shapes. The sandwich targets were cut in 200 mm x 200 mm dimensions to install in the specimen holder. The sandwich targets were fully supported by the help of the steel clamps. The clamping was applied carefully and slowly to prevent the collapse of the core.

The composite plates and sandwich structures were examined after the projectile impact test and size of visible projectile damage was measured on both surfaces of the materials. Furthermore, the ballistic limits for the composite plates and sandwich structures were determined from the recorded impact and residual velocities. The energy absorbed by the composite plates and sandwich structures were also calculated.

CHAPTER 4

RESULTS

4.1. Fiber Volume Fraction of Composite Samples

The fiber volume fraction calculations were based on 0.6 fiber volume fraction. This calculated fraction may vary resulting from the inefficiencies in the processing. Table 4.1 tabulates the ceramic crucible weights (M1), the ceramic crucible and composite sample weights (M2), ceramic crucible and composite sample weights after burn-off (M3) and fiber (m_f) and matrix (m_m) weights of 9 composite samples of 50 mm long, 50 mm wide and 2 mm, 3 mm and 5 mm thick. The calculated fiber volume fraction using Equation 3.16 are also listed in Table 4.2. In the calculations, the density of E-glass fiber (ρ_f) was taken as 2550 kg/m^3 and the density of the polyester resin was measured (ρ_m) as 1220 kg/m^3. The fiber volume fraction is found to vary between 0.506 and 0.515 as tabulated in Table 4.2. As the thickness increased the fiber volume fraction increased on slightly.

Table 4.1. The recorded masses for resin burn-off method.

Sample Name	**M_1**	**M_2**	**M_3**	**m_f**	**m_m**
Sample 1	25.25 g	28.66 g	27.55 g	2.3 g	1.11 g
Sample 2	22.75 g	26.08 g	24.98 g	2.23 g	1.1 g
Sample 3	23.53 g	26.67 g	25.61 g	2.08 g	1.06 g
Sample 4	22.75 g	25.63 g	24.74 g	1.99 g	0.89 g
Sample 5	23.38 g	26.18 g	25.32 g	1.94 g	0.86 g
Sample 6	22.97 g	25.81 g	24.92 g	1.95 g	0.89 g
Sample 7	23.42 g	24.76 g	24.36 g	0.94 g	0.4 g
Sample 8	23.01 g	24.63 g	24.14 g	1.13 g	0.49 g
Sample 9	22.41 g	24.32 g	23.74 g	1.33 g	0.58 g

Table 4.2. The fiber volume fractions.

SampleGroup	Sample 1 Fiber Volume Fraction	Sample 2 Fiber Volume Fraction	Sample 3 Fiber Volume Fraction	Average Fiber Volume Fraction
2 mm thick	0.484	0.512	0.523	0.506
3 mm thick	0.492	0.519	0.525	0.512
5 mm thick	0.498	0.517	0.529	0.515

4.2. Tensile Properties of Composite Samples

$[0°/90°]_s$ fiber oriented tension test samples were tested in 3 principal material directions for each directions at least 3 samples were tested at 2 mm/min cross-head speed. The tensile stress-strain curves of the principal material direction 1 and 2 are shown in Figure 4.1. For the first principal axis; the average tensile strength is 412 MPa, the average elastic modulus is 16.6 GPa and the average failure strain is 0.0247. The Poisson's ratio for the principal plane 21 is found 0.13, for the principal plane 31 and plane 32 0.23. The tensile properties of the principal material direction 2 are nearly same with the direction 1 since the fiber orientation is quite similar and biaxial. For this direction, the average tensile strength is 407.8 MPa, the average elastic modulus is 16.51 GPa and the average failure strain is 0.0244. Tensile tests of through thickness direction of the composite were also performed and the result is shown in Figure 4.2. The tensile strength in this direction is 4.2MPa, the elastic modulus is 6.8GPa and the failure strain is 0.0005.

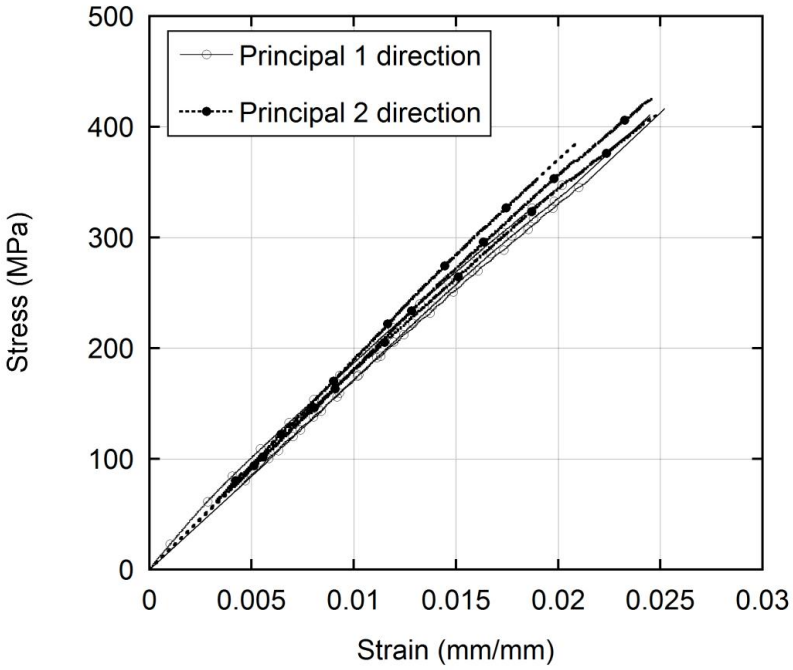

Figure 4.1. Tensile stress-strain curves for the principal direction 1 and 2.

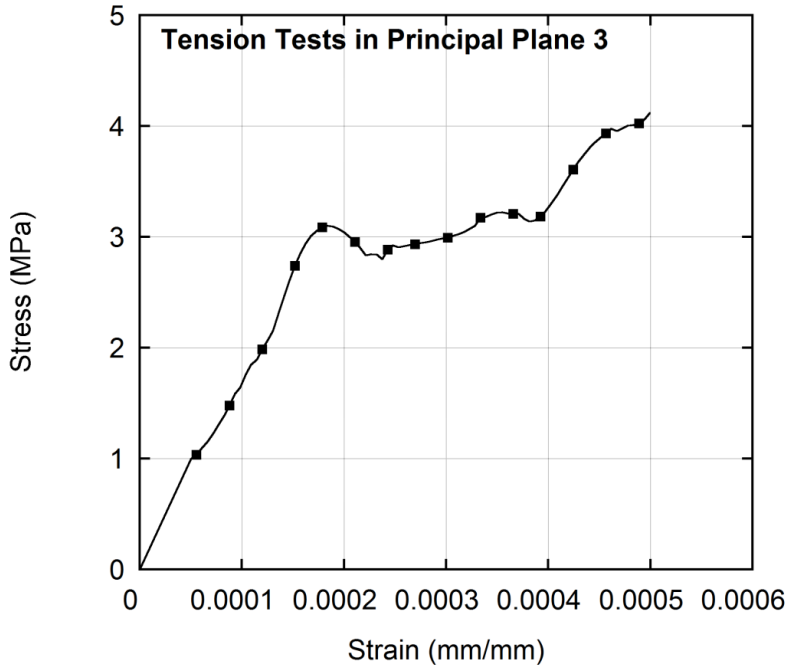

Figure 4.2. Tensile stress-strain curves for the principal direction 3.

4.3. Compression Properties of Composite Samples

The compression testing on $[0°/90°]_s$ and $[\pm45°]_s$ composite samples were performed at 10^{-3}, 10^{-2}, $10^{-1}$and 500-1200 s^{-1} strain rates. The stress-strain curves of $[0°/90°]_s$ composite samples for 1, 2 and 3 directions at different strain rates are shown sequentially in Figures 4.3(a-c). Under compression loading, the material response is nearly linear elastic up to the maximum stress point followed by abrupt failure in all directions. The compression stress-strain curves of the composite samples in 1 and 2 directions are noted to be similar in Figures 4.3(a) and (b) because of the biaxial fiber orientation. While, as the strain rate increases maximum compression or failure stress increases. The compression strength of the composite in 3 direction is higher as seen in Figure 4.3(c) and increases with increasing strain rate. The increase in compression strength in direction at high strain rates is also much higher than 1 and 2 directions. It is also noted that except 1 direction the failure strain decreases at increasingly high strain rates.

The typical compression stress-strain responses for $[\pm45°]_s$ E-glass/polyester composite at different strain rates in all principle directions are shown in Figures 4.4(a-c). Under quasi-static loading, the material response is nearly linear elastic up to the maximum stress point followed by a gradual stress decrease as the composite develops damage. The $[\pm45°]_s$ samples also show similar compression behavior in principal directions 1,and 2. As similar with $[0°/90°]_s$ samples, in 3 direction $[\pm45°]_s$ samples show higher strength values and a higher strain rate sensitivity as depicted in Figure 4.4(c). As a summary, the effect of strain rate is to increase the compression modulus and strength with reduction in failure strain.

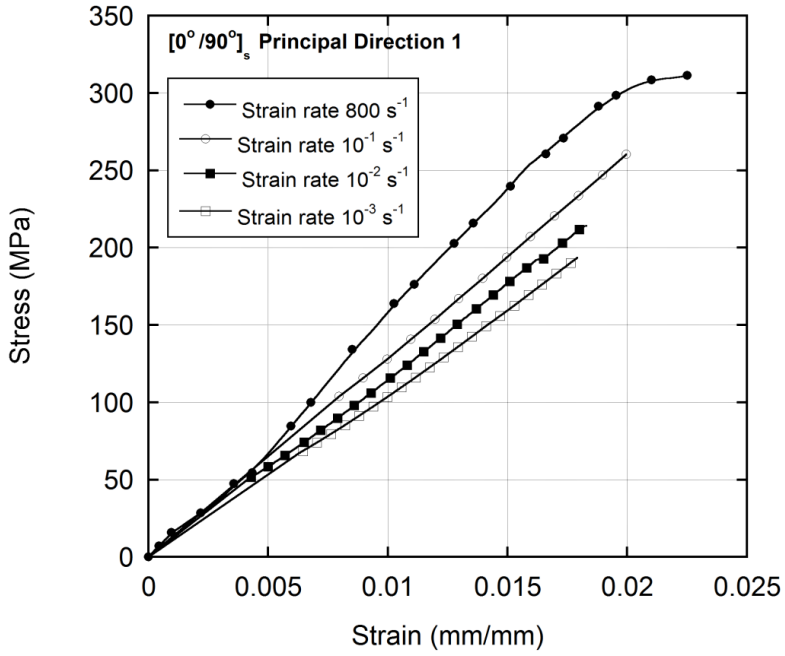

(a)

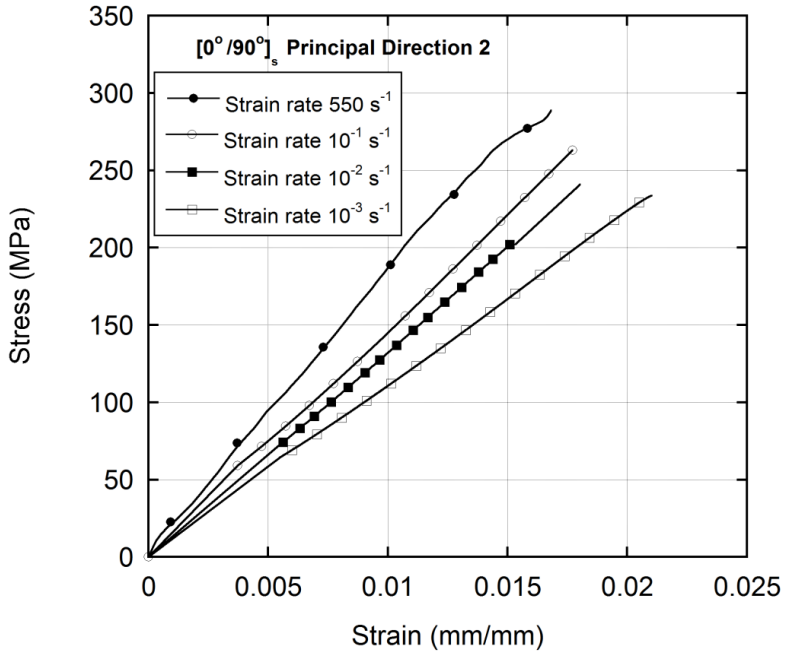

(b)

Figure 4.3. The compressive response of composite samples at different strain rates in (a) direction 1, (b) direction 2 and (c) direction 3.

(cont. on next page)

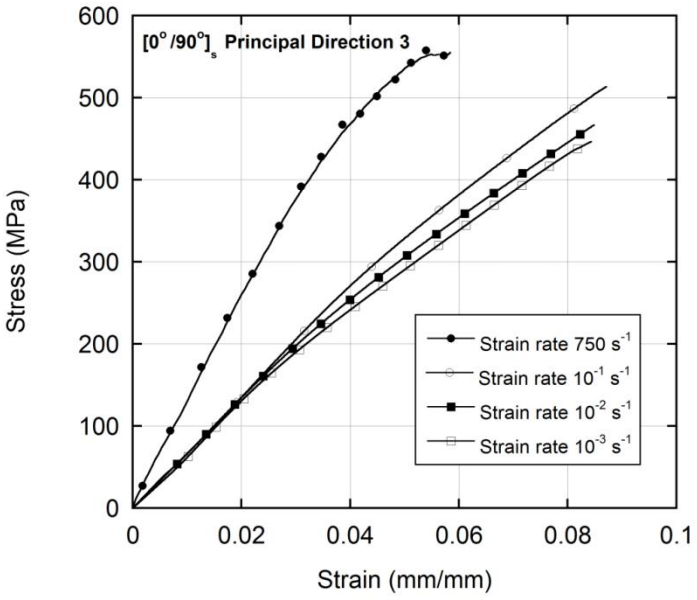

(c)

Figure 4.3. (cont.).

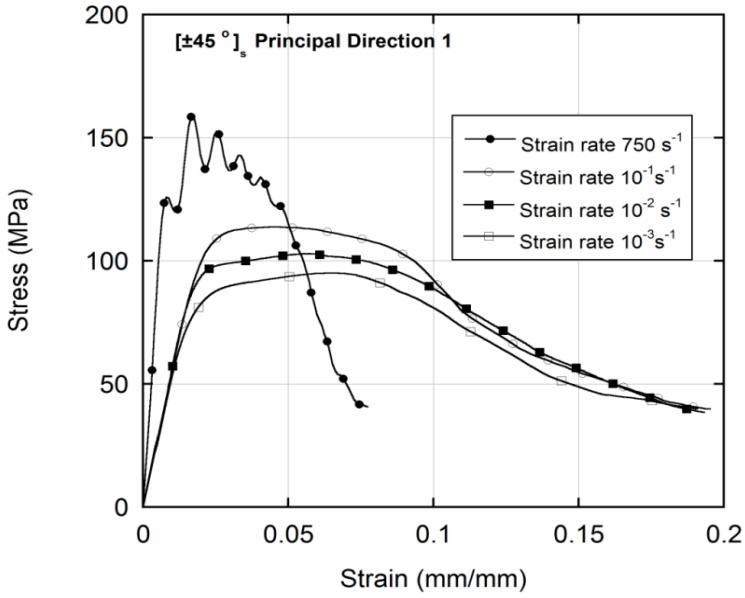

(a)

Figure 4.4. The compressive response of $[\pm 45°]_s$ composite samples at different strain rates in (a) direction 1, (b) direction 2 and (c) direction 3.

(cont. on next page)

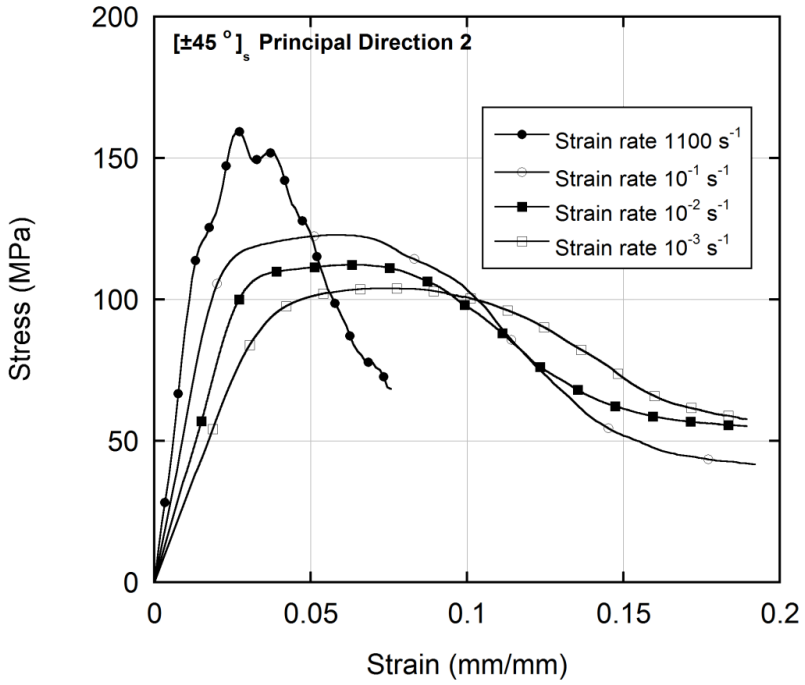

(b)

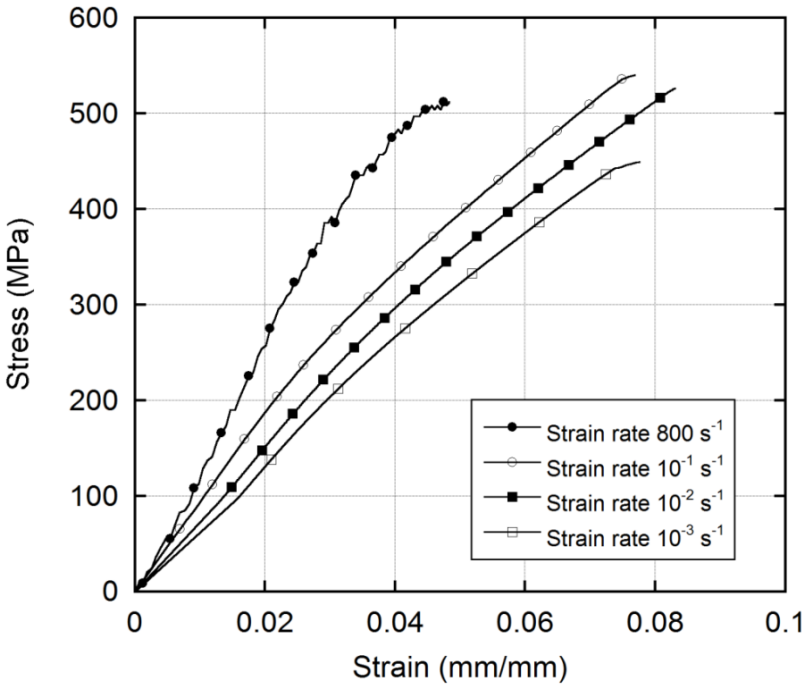

(c)

Figure 4.4. (cont.).

4.4. Shear Properties of Composite Samples

In the shear tests of $[\pm 45°]_s$ E-glass/polyester composite samples, the longitudinal and transverse strains were recorded to determine the shear strain. Figure 4.5 shows the recorded longitudinal and transverse strains using strain gages. The stress-strain curves were determined in principle plane 12, principle plane 23 and principle plane 31 are shown sequentially in Figures 4.6(a-b). In principle plane 12 (Figure 4.6(a)), the average shear stress is determined 43.41 MPa, the average shear modulus is determined 3.885 GPa and the ultimate shear strain is determined 0.553. In principle plane 32 (Figure 4.6(b)), the average shear stress is 0.8 MPa, the average shear modulus 1.655 GPa and the ultimate strain 0.0025. Finally, in principle plane 31 (Figure 4.6(b)), the average shear stress is 2 MPa, the average shear modulus is 1.62 GPa and the ultimate strain is 0.0022.

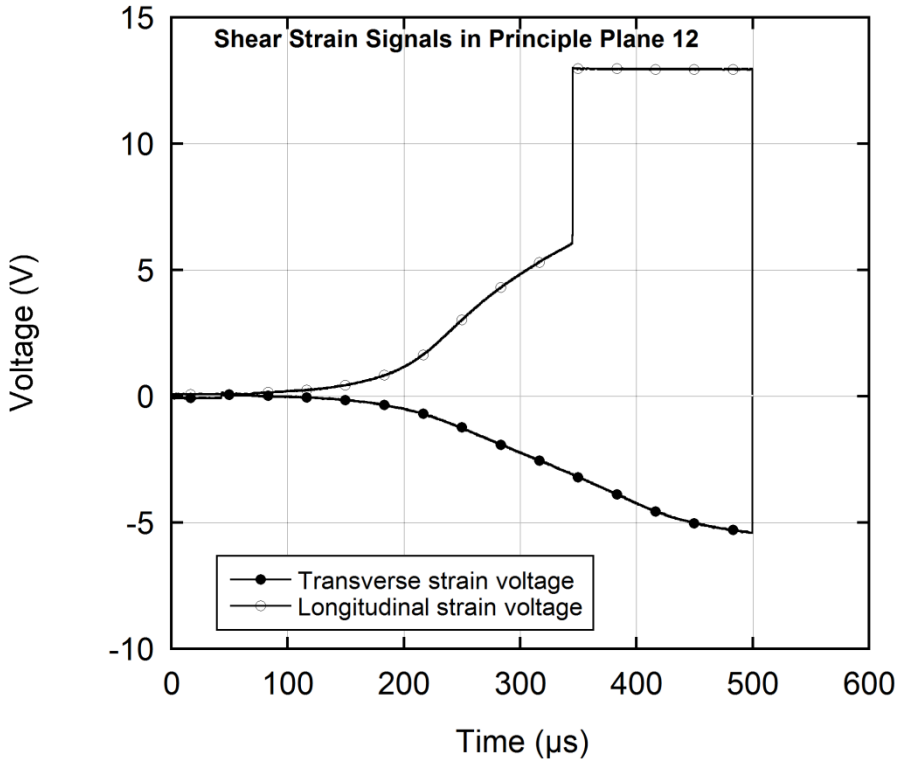

Figure 4.5. Shear strain voltages in principle directions recorded by strain gages.

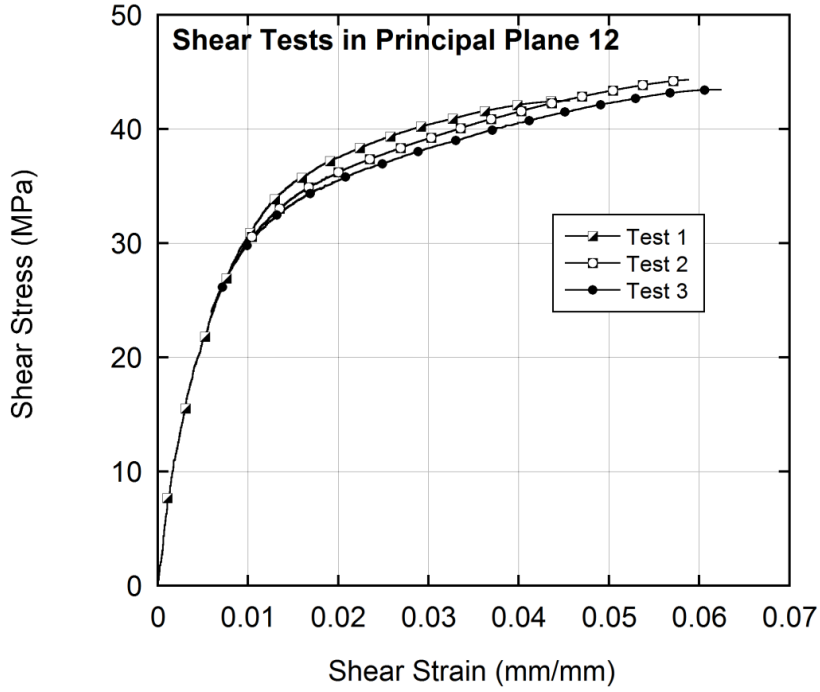

(a)

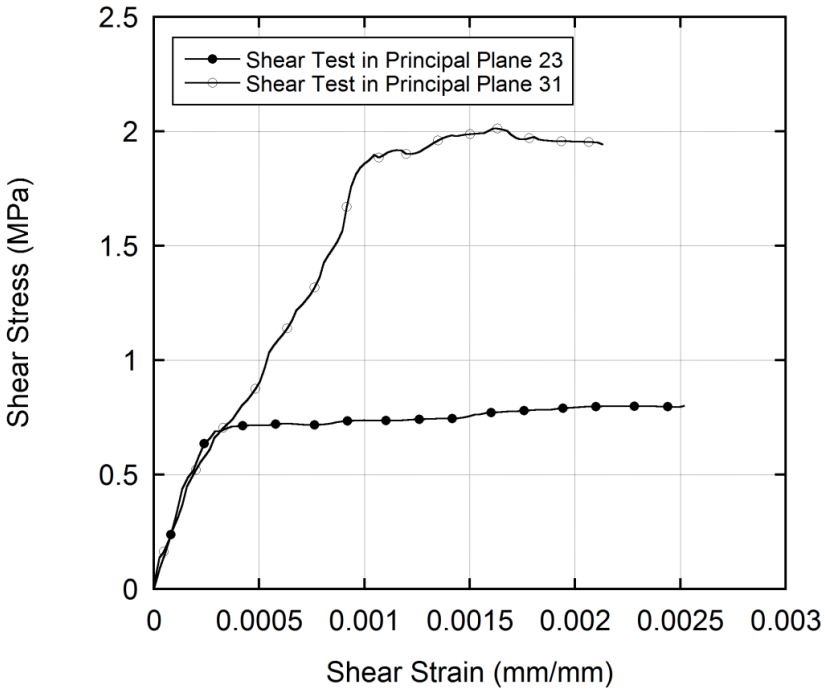

(b)

Figure 4.6. The shear response of composite samples (a) principle plane 12, (b) principle plane 32 and 31.

4.5. Off-Axis Tensile Properties of Composite Samples

Figure 4.7 shows the tensile stress-strain curves of 30° and 60° fiber orientated samples. The off-axis tensile properties of composite samples with different off-axis angles are tabulated in Table 4.3. In the same table the failure stresses based on Tsai-Wu criterion (Equation 3.6) is also listed for comparison. The comparison of the theoretical and experimental stress values of the E-glass/polyester composite samples is further depicted in Figure 4.8.

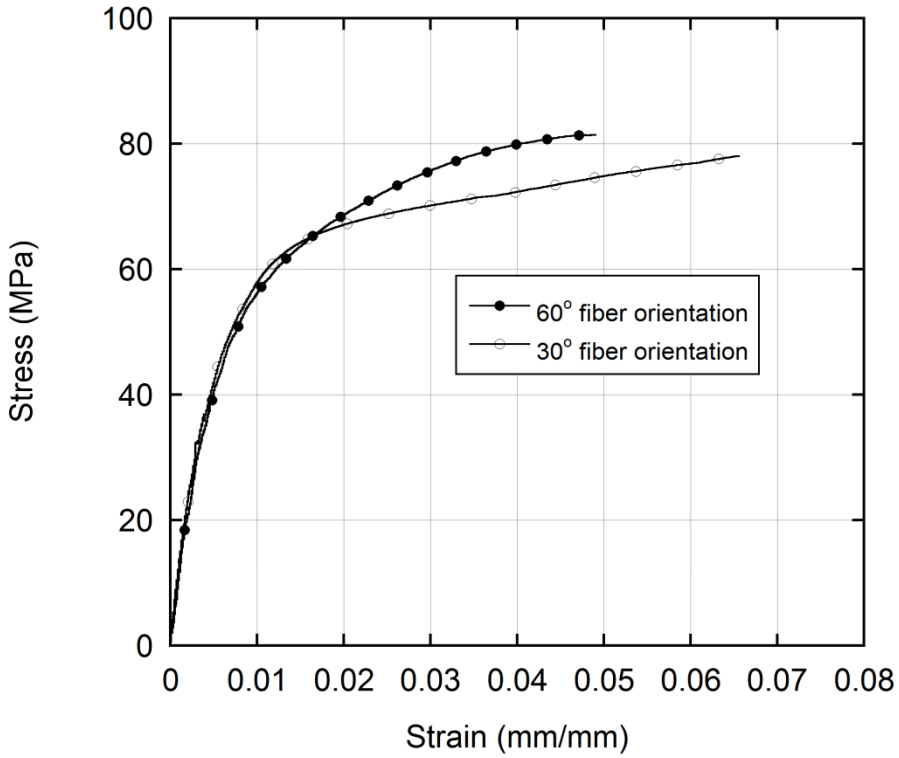

Figure 4.7. The off-axis tensile responses of E-glass/polyester composite.

Table 4.3. Off-axis tensile properties of composite samples.

OFF-AXIS TENSILE PROPERTIES OF COMPOSITESAMPLES		
Fiber orientation	**Experimental Strength (MPa)**	**Tsai-Wu Criterion Strength (MPa)**
0°	412	412
30°	78	98
45°	43	86
60°	81	98
90°	407.8	407.8

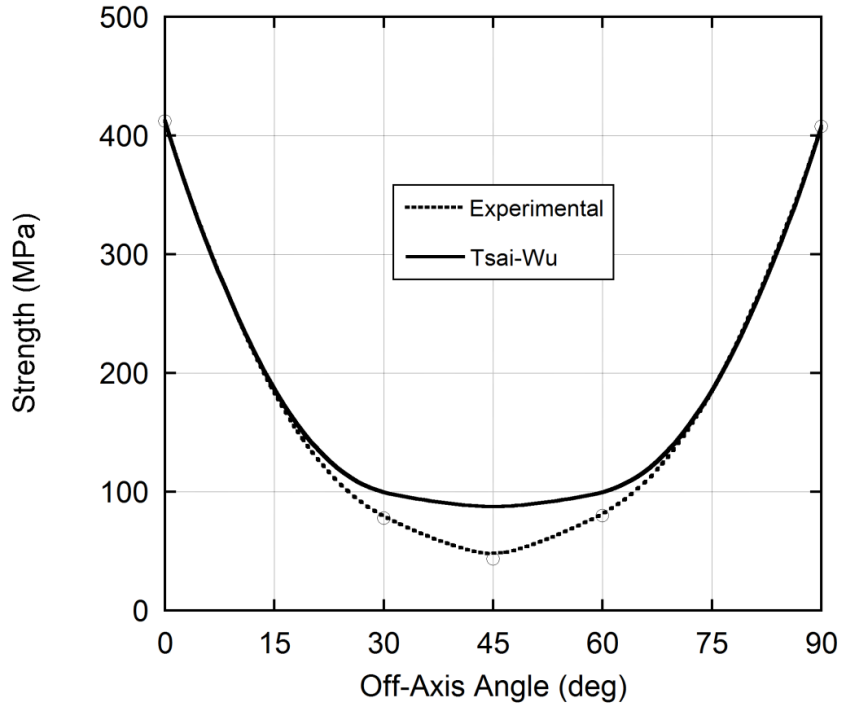

Figure 4.8. Comparison of theoretical and experimental off-axis failure stress.

4.6. Flexure Response of Composite Samples

The flexural stress-strain responses of 2 mm, 3 mm and 5 mm thick E-glass/polyester $[0°/90°]_s$ composite samples are shown in Figure 4.9. The flexural strength and flexural modulus values of 2, 3 and 5 mm thick samples are tabulated in Table 4.4. The properties are found to be very similar for the samples tested.

Table 4.4. The flexural properties of composites.

Specimen	Flexural Strength (MPa)	Flexural Modulus (GPa)	Span Length (mm)
2mm $[0°/90°]_s$	500	20.111	32
3mm $[0°/90°]_s$	505	20.327	48
5mm $[0°/90°]_s$	553	20.647	80

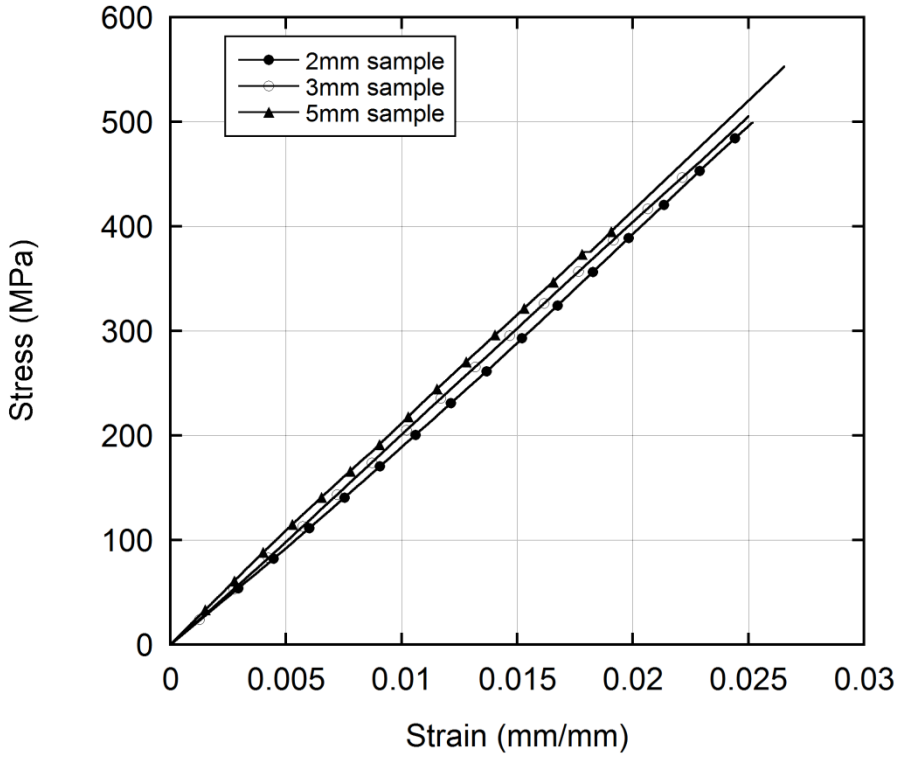

Figure 4.9. Flexural stress-strain responses of [0°/90°] E-glass/polyester composites.

4.7. Interlaminar Shear Properties of Composite Samples

The short beam stress-strain curves of $[0°/90°]_s$ and $[\pm45°]_s$ composite samples are shown in Figure 4.10 and Figure 4.11, respectively. The average interlaminar shear strength of $[0°/90°]_s$ and $[\pm45°]_s$ composite is found very similar; 21.4 MPa and 21.9 MPa, respectively.

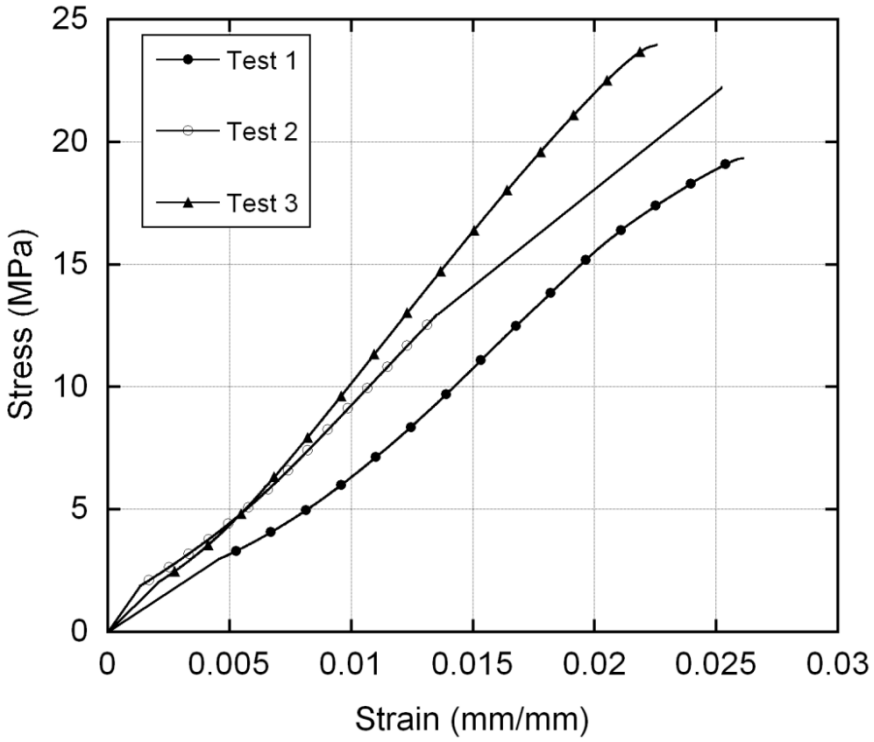

Figure 4.10. Interlaminar shear strength of [0°/90°] E-glass/polyester composites.

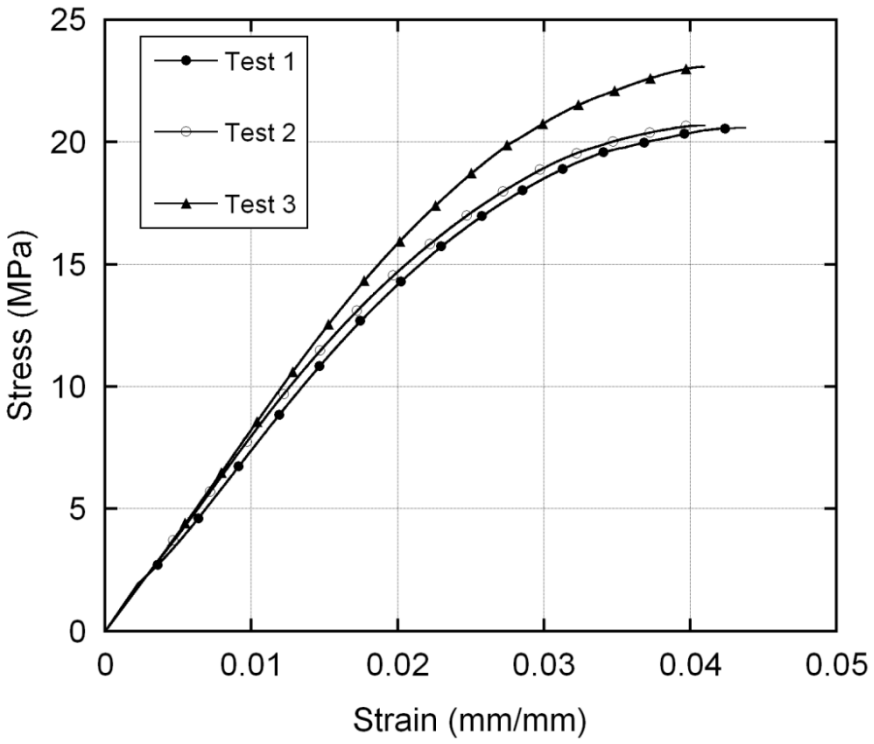

Figure 4.11. Interlaminar shear strength of [±45°] E-glass/polyester composites.

4.8. Compression Properties of Aluminum Foam and Corrugated Aluminum Structures

The quasi-static (10^{-3} s^{-1}) compression stress-strain curves of Alulight aluminum foams of 0.11 and 0.15 relative densities are shown in Figure 4.12. The curves exhibit characteristic of metallic foam deformation and comprise three regions: (1) an elasto-plastic deformation where partially reversible cell walls bending occurs, (2) an extended plateau where cell walls buckle, yield and fracture and (3) rapidly increasing stress region, where the cell walls become pressed together and the material attains bulk-like properties. In the plateau region, the stress is noted to be not constant and increases with increasing strain. For an ideal energy absorber, a constant stress plateau region is expected. The compression mechanical properties of the tested aluminum foams of 0.11 and 0.15 relative densities are tabulated in Table 4.5. It is noted in same table, as the relative density increases modulus and plateau stress increases.

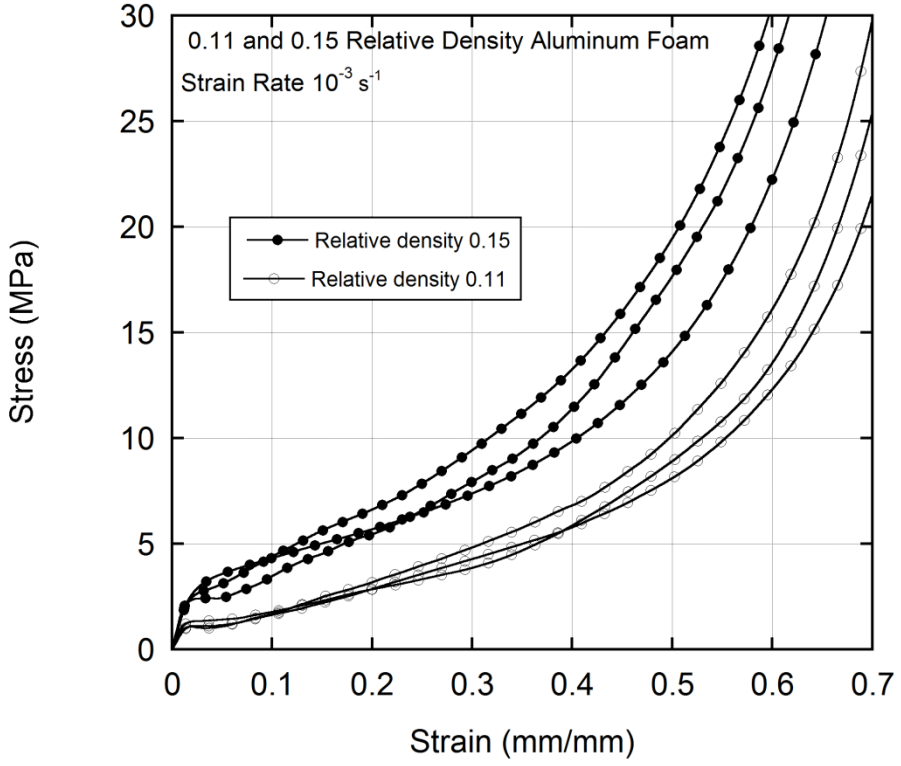

Figure 4.12. Compression stress-strain curves of 0.11 and 0.15 relative density aluminum foam.

Table 4.5. The compression mechanical properties of tested aluminum foams.

Material	**Density ρ (kg/m^3)**	**Young's modulus E (GPa)**	**Poisson's ratio, ν**	**Plateau Stress, $\sigma_{pl}(MPa)$**	**Densification strain, ε_D**
0.15 relative density Al foam	512	0.13	0.29	2.4	0.79
0.11 relative density Al foam	426	0.06	0.29	1.11	0.85

The uniaxial quasi-static (10^{-3} s^{-1}) compressive stress-strain curves of brazed small (relative density of 0.24) and big (relative density of 0.13) fin corrugated aluminum structures are shown in Figure 4.13. As is expected, the small fin corrugated structure show higher plateau stresses than big fin corrugated structure as seen in Figure 4.13. The effect of epoxy mounting on the compression stress-strain curve of big fin corrugated structure is shown in Figure 4.14. Epoxy mounting increases plateau stress values and decreases densification strain of the big fin corrugated structure. This effect will be elaborated later. The determined compressive mechanical properties of the big and small fin corrugated structures are summarized in Table 4.6.

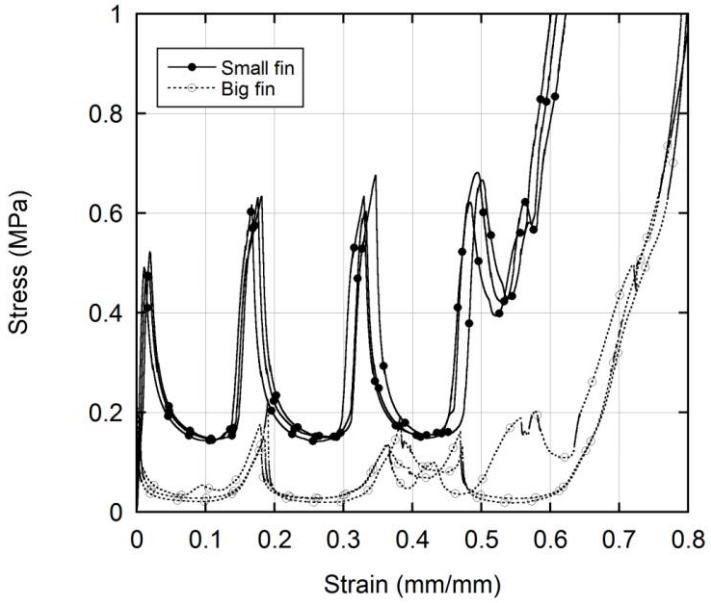

Figure 4.13. Brazed small and big fin corrugated aluminum structures compressive stress-strain curves.

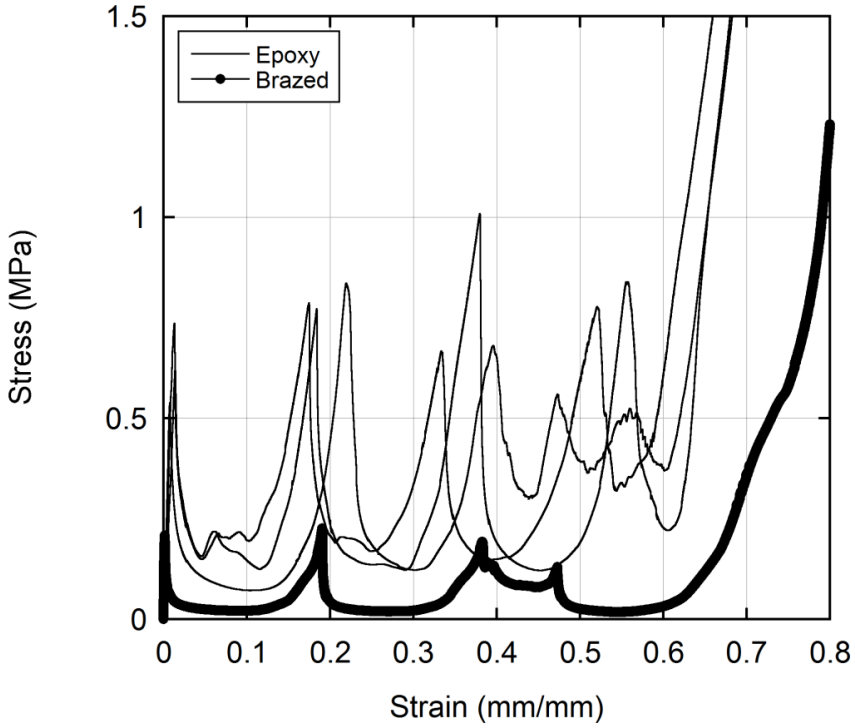

Figure 4.14. Epoxy mounted and brazed big fin corrugated aluminum structures compressive stress-strain curves.

Table 4.6. Compressive mechanical properties of corrugated aluminum structures.

Material	**Density (kg/m^3)**	**Yield Strength,** $\sigma_y(MPa)$	**Young's Modulus, E (GPa)**	**Plateau Stress,** $\sigma_{pl}(MPa)$	**Densification strain,** ε_D
Small fin (Braze)	656	0.46	0.055	0.15	0.56
Big fin (Brazed)	361	0.18	0.038	0.027	0.62
Big fin (Epoxy bonding)	327	0.6	0.049	0.15	0.65

4.9. Low Velocity Impact Properties of Composite Plates

In low velocity impact tests, the rebound velocity, saturation impact velocity, perforation velocity and the energy absorption of the $[0°/90°]_s$ and $[\pm45°]_s$ fiber oriented E-glass/polyester composite laminates were determined. DAS 16000 data acquisition

system of Ceast-Fractovis instrumented drop weight impact tester can only measure the initial velocity of the impactor and force vs. time. The parameters such as absorbed energy, velocity of the impactor and deflection, are calculated using the equations of motion.

The force-time responses of the $[0°/90°]_s$ and [±45°]s fiber oriented E-glass/polyester composite laminates with 2 mm, 3 mm and 5 mm thickness are sequentially shown in Figures 4.15(a-c) and Figures 4.16(a-c). The letters on these graphs, P, S, R refer to perforation, saturation and rebound, respectively. In saturation there is partial penetration but no perforation. The incipient damage and maximum forces of 2, 3 and 5 mm thick $[0°/90°]_s$ composite plates are 1102 and 6607 N, 2250 and 8115 N and 4113 and 18689 N, respectively. The incipient damage and maximum forces of 2, 3 and 5 mm thick $[±45°]_s$ composite plates are 1088 and 7214.5 N, 2550 and 10108 N and 4816.4 and 20935 N, respectively. These results show that $[±45°]_s$ composite plates show higher perforation forces than $[0°/90°]_s$ composite plates. The perforation impact energy responses of the $[0°/90°]_s$ and $[±45°]_s$ fiber oriented E-glass/polyester composite laminates with 2 mm, 3 mm and 5 mm thickness are shown in Figure 4.17. As the thickness of the composite increases the absorbed energy increases. In addition, a higher energy absorption is clearly seen in $[±45°]_s$ composite plates than $[0°/90°]_s$ composite plates, which is in accord in measured higher perforation forces in in $[±45°]_s$ composite plates. In Table 4.7, the incident damage force, maximum force, failure force, maximum energy, incipient damage and failure energy and absorbed energy of the tested composite specimens are tabulated.

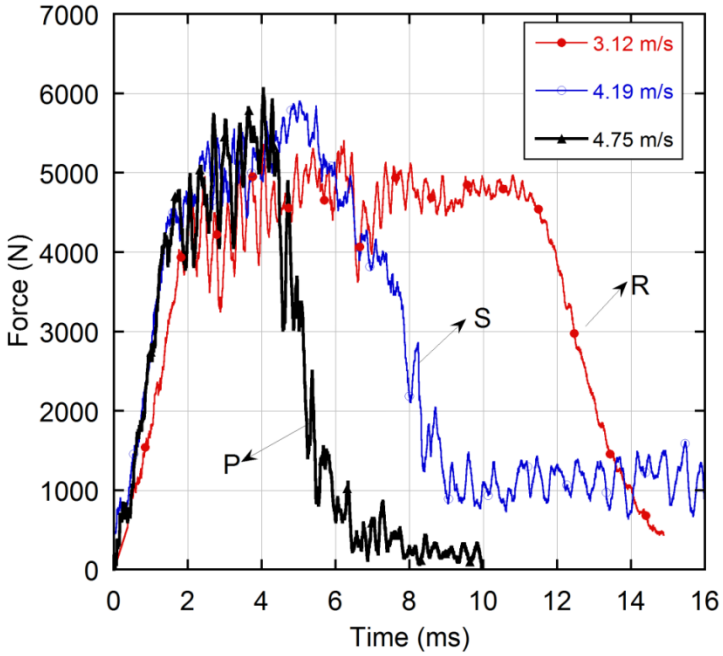

(a)

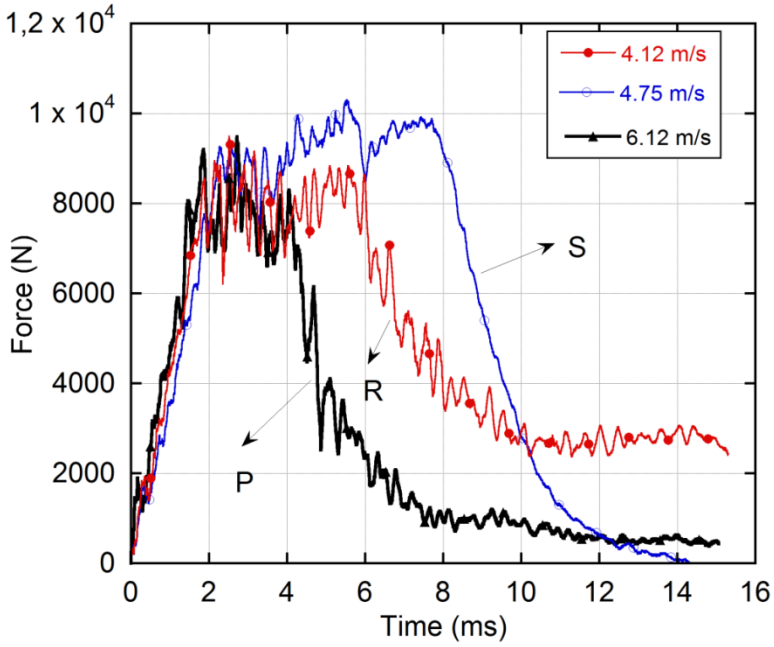

(b)

Figure 4.15. Force-time histories for the drop weight impact test of (a) 2, (b) 3 and (c) 5 mm $[0°/90°]_s$ composite laminates.

(cont. on next page)

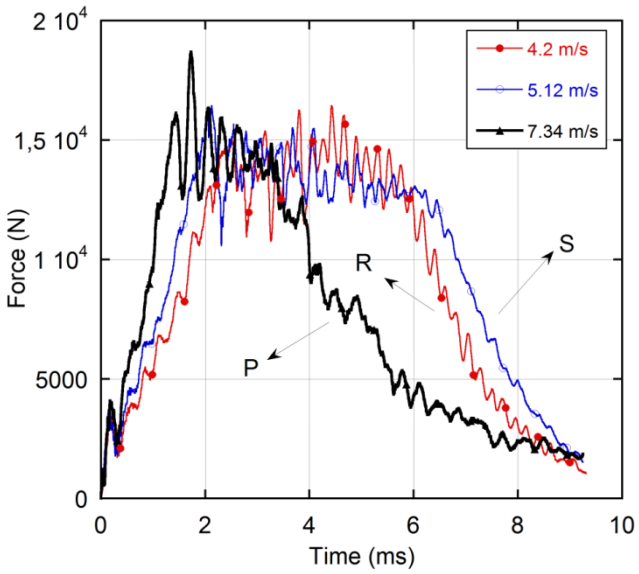

(c)

Figure 4.15. (cont.).

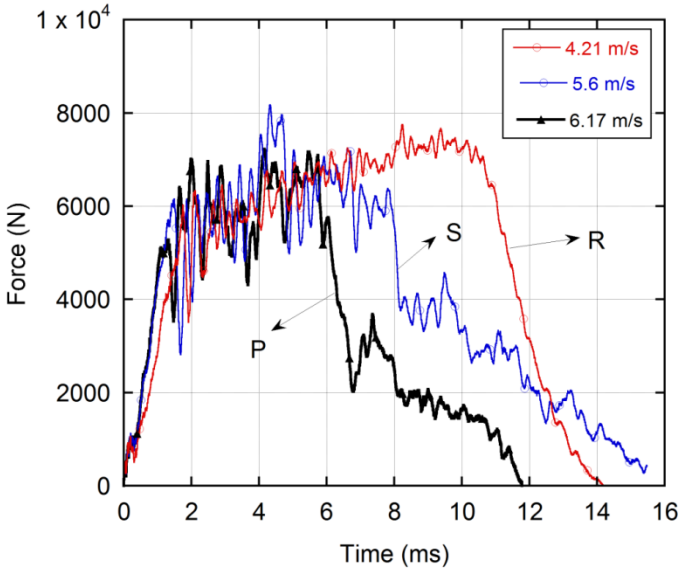

(a)

Figure 4.16. Force-time histories for the drop weight impact test of (a) 2, (b) 3 and (c) 5 mm $[\pm 45°]_s$ composite laminates.

(cont. on next page)

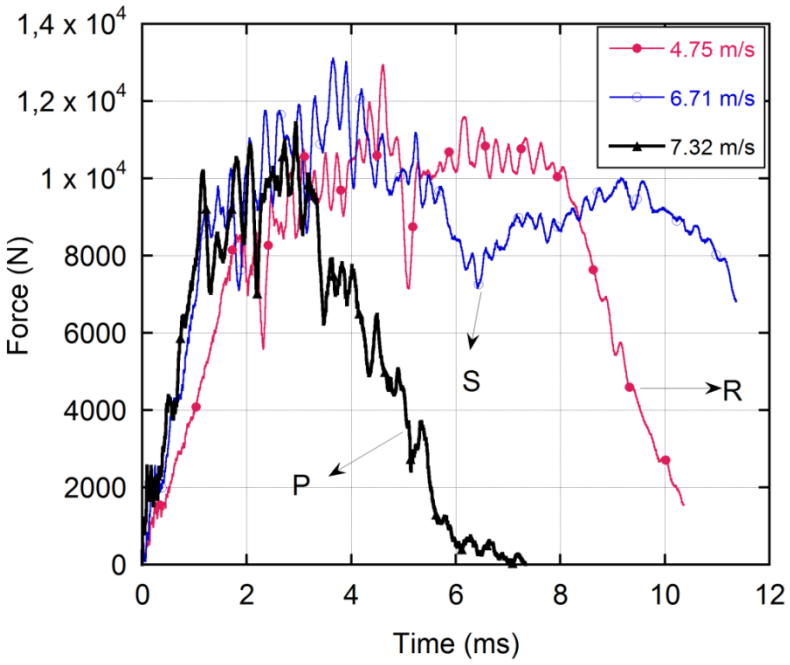

(b)

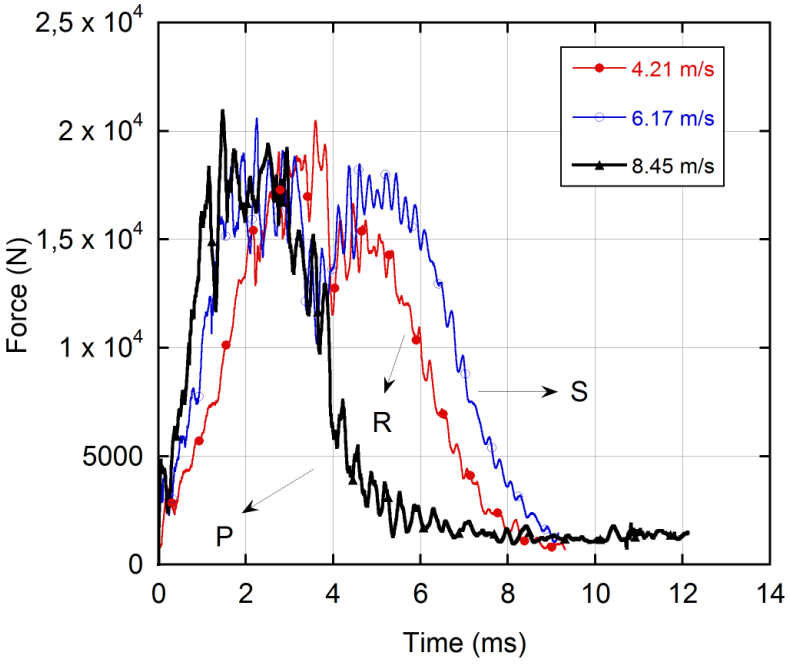

(c)

Figure 4.16. (cont.).

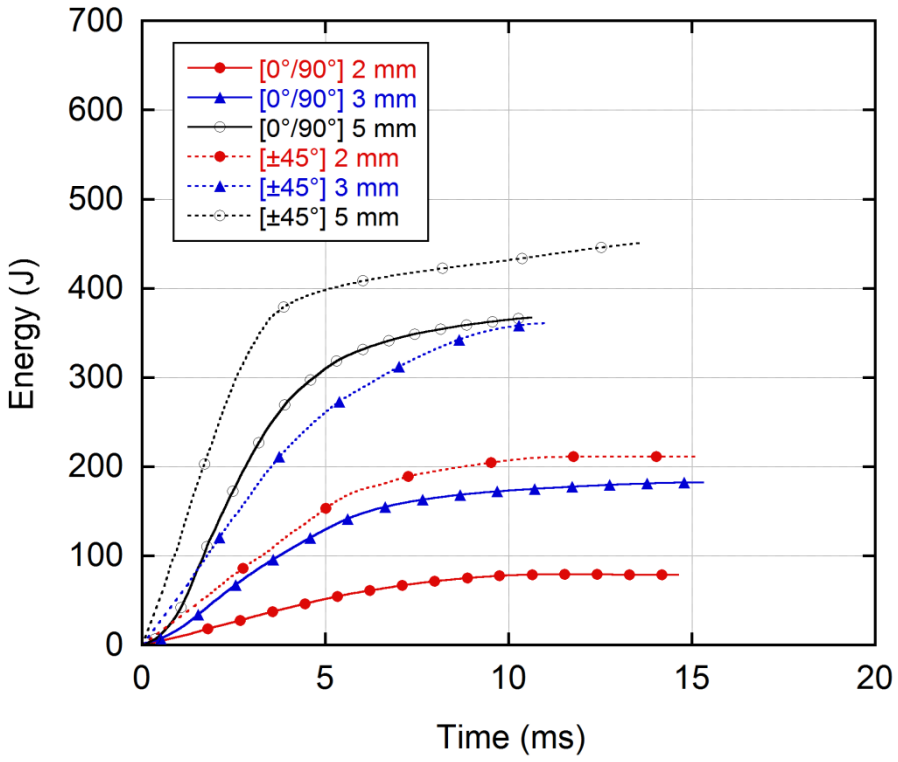

Figure 4.17. Energy-time histories for the drop weight impact test of $[0°/90°]_s$ and $[\pm45°]_s$ composite specimens.

Table 4.7. Low velocity impact properties of composite specimens.

Specimen Name	Maximum Force (N)	Failure Force (N)	Energy at Maximum Force (J)	Incipient damage energy (J)	Energy at failure (J)	Absorbed Energy (J)
$[0°/90°]_s$ 2 mm	6607	1438	109.7	1	125.6	129.5
$[0°/90°]_s$ 3 mm	8115	2430	90	2.7	134	153
$[0°/90°]_s$ 5 mm	18689	4388	110	4.4	326	358
$[\pm45°]_s$ 2 mm	7214.5	1755	110	2	194	210.4
$[\pm45°]_s$ 3 mm	10108	2433	151	4	227	238
$[\pm45°]_s$ 5 mm	20935	3883	114	6	384	451

4.10. Projectile Impact Properties of Composite Plates and Sandwich Structures

The ballistic limit and perforation energy which are the keys parameters for evaluating the penetration resistant behavior and energy dissipating performance of the composite laminates. The perforation energy is equal to the change of kinetic energy of the projectile dissipated by the composite laminates and given as,

$$E_p = \frac{1}{2} m_p V_i^{\,2} - \frac{1}{2} m_p V_r^{\,2} \tag{4.1}$$

Where m_p is the mass of projectile, V_i is the impact velocity and V_r is residual velocity. The ballistic limit can be calculated, assuming that the kinetic energy loss of the projectile is all dissipated by the composite laminate. The corresponding ballistic limit is calculated as

$$V_b = \sqrt{\frac{E_p}{2}} m_p \tag{4.2}$$

In Table 4.8, the projectile impact responses of the composite plates and sandwiches are tabulated. In Table 4.8, PE refers to perforation and PP refers to partial perforation. It is noted in same table all composite samples and corrugated sandwiches except 5 mm thick composite face sheet corrugated sandwiches are perforated and all aluminum foam sandwiches structures show partial perforation at the similar impact velocities.

Table 4.8. The projectile impact responses of the composite plates.

Specimen	Incident Velocity (m/s)	Incident Kinetic Energy (J)	Residual Velocity (m/s)	Residual Kinetic Energy (J)	Energy Absorbed (J)	Damage	Ballistic Limit (m/s)
$[0°/90°]_s$ 2mm	152.1	1295.5	84.2	397	898	P	126.6
$[0°/90°]_s$ 3mm	175.2	1719	114.4	732.9	986.1	P	132.8
$[0°/90°]_s$ 5mm	154.82	1342.3	65.41	239.6	1102.7	P	140.32
$[±45°]_s$ 2mm	144.5	1169.3	75.1	315.8	853.5	P	123.5
$[±45°]_s$ 3mm	180.6	1826.5	111.7	698.71	1127.81	P	141.9
$[±45°]_s$ 5mm	150.9	1275.2	47.5	126.35	1148.85	P	143.2

(cont. on next page)

Table 4.8. (cont.).

Aluminum Foam (0.15)	150	1237.5	90	445.5	792	P	120
Big fin corrugated structure epoxy sticking	150	1237.5	74.83	307.97	929.53	P	130
Small fin corrugated structure brazed	150	1237.5	66.7	244.7	992.8	P	134.4
Big fin corrugated structure brazed	150	1237.5	90	445.5	792	P	120
Big fin corrugated composite sandwich (2mm)	166.8	1530.2	72.5	289.1	1241.1	P	150.2
Big fin corrugated composite sandwich (3mm)	164.6	1490.1	6.4	2.25	1487.85	P	164.47
Big fin corrugated composite sandwich (5mm)	181.6	1813.82	0	0	1813.82	PP	>181.6
0.11 Al foam composite sandwich (2mm)	160.2	1411.5	0	0	1411.5	PP	>160.2
0.11 Al foam composite sandwich (3mm)	176.8	1719.2	0	0	1719.2	PP	>176.8
0.11 Al foam composite sandwich (5mm)	180.7	1795.9	0	0	1795.9	PP	>180.7
0.15 Al foam composite sandwich (2mm)	179.6	1774.1	0	0	1774.1	PP	>179.6
0.15 Al foam composite sandwich (3mm)	184.8	1878.3	0	0	1878.3	PP	>184.8
0.15 Al composite sandwich (5mm)	190	1985.5	0	0	1985.5	PP	>190

CHAPTER 5

DISCUSSION

5.1. Determination of Fiber Volume Fraction of Composite Samples

The volume fraction is a critical parameter as the theoretical equations for determining the stiffness, strength and hygrothermal properties of a unidirectional composite are function of fiber volume fraction. Voids, impurities, air entrapment during the resin infusion affect the volume fractions and cause a lower theoretical density than the actual density. The variations in the volume fractions cause relatively lower shear stiffness and strength, compressive strengths, transverse tensile strengths, fatigue resistance and moisture resistance. The targeted fiber volume fraction of the prepared composites is 0.6 with a thickness variation approximately +0.5 mm. While, the fiber volume fractions for 2 mm, 3 mm and 5 mm thick composite plates were found 0.506, 0.512 and 0.515, respectively, which were lower than the calculated fiber fraction. The lower volume fraction obtained in the prepared composites after burn-off tests is partly due to the number of plies calculated. In the calculation, the numbers of E-glass piles are found 3.27, 4.91, 8.18 for 2 mm, 3 mm and 5 mm thick composite. These numbers are rounded as 3, 4 and 8 layers of E-glass fibers. However, by changing the number of plies, the fiber volume fraction of the composite plates was also changed.

.

5.2. Tension Properties of Composite Samples

The experimental tensile test results of the composite samples are tabulated in Table 5.1 together with those of similar composites in the literature. Tensile testing of composite plates for principal directions 1 and 2 results in nearly similar modulus and strength values because of the symmetry arising from the fiber architecture. In contrast, the elastic modulus and strength values in direction 3 show significant variations from those in planes of 1 and 2. In the principal direction 3 in which the matrix properties are dominant, the strength and elastic modulus values are much lower than those of 1 and 2

direction. It is further noted the determined strength values are also in agreement with those in literature.

Generally, the specimens fail in the same manner for principal directions 1 and 2 but in direction 3 the samples the fiber-matrix debonding is the main failure mechanism. The failed tensile test specimen picture in 1 direction is shown in Figure 5.1. The macroscopic damage mechanisms include matrix cracking, localized warp fiber fracture, weft fiber pull-out, and delamination along the middle plies.

Table 5.1. The tensile properties of E-glass/polyester composite samples.

Mechanical Properties		**Experimental**	**Literature[34]**
Tensile Modulus (GPa)	E_1	16.6	14
	E_2	16.51	14
	E_3	6.8	5.3
Tensile Strength (MPa)	σ_1	412	430
	σ_2	407.8	430
	σ_3	4.2	-
Poisson's Ratio	υ_{21}	0.13	-
	υ_{31}	0.23	-
	υ_{32}	0.23	-

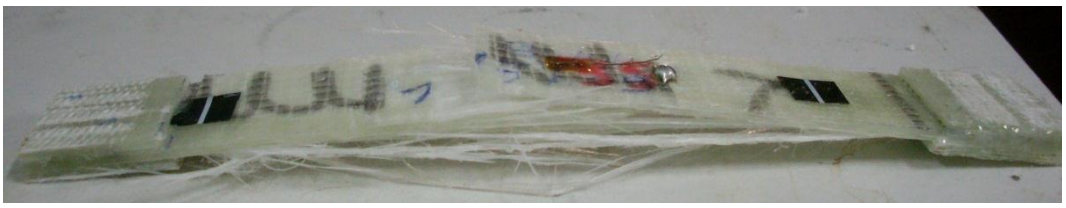

Figure 5.1. The tested tensile test specimens in direction 1.

When the results are compared with data from the literature, there is not such a big difference in the results except the tensile strength in the principle direction 3.

5.3. Mechanical Properties of Composite Samples

Both composite samples are found to be strain rate sensitive and increasing strain rate increases the compression stresses and elastic modulus of $[0°/90°]_s$ and $[\pm45°]_s$ composites at the same strain. The increase in failure stress in 3 direction with increasing strain rate is more pronounced in both composites. This effect is mainly attributed to the strain rate sensitivity of polyester matrix in this direction. It is also noted that $[0°/90°]_s$ composite samples have higher elastic modulus and strength but lower strains in principle directions 1 and 2. The elastic moduli for $[0°/90°]_s$ composite samples are higher in the principle direction 3. $[\pm45°]_s$ composite samples show higher elastic modulus in the principal direction 3. The effect of fiber orientation leads to variations in the moduli and strength values in tested composites.

Compression loading of a unidirectional composite perpendicular to the fiber involves failure of the matrix and fiber/matrix interface and often occurs in shear type. Generally, four types of failure modes are seen; axial splitting, shear failure, kink zone and buckling. In Figures 5.2(a-c), the failure modes in all principal directions for $[0°/90°]_s$ composite samples tested at quasi-static strain rate are shown. Shear banding and axial splitting are the main failure modes of the $[0°/90°]_s$ composite samples in 1 and 2 direction as seen in Figures 5.2(a) and (b), while shear banding is the main deformation mode in 3 direction as seen in Figure 5.2(c). The corresponding failure modes of the same composite in the same test directions in SHPB testing are also shown in Figure 5.3(a-c) for comparison. At high strain rates, the composite fails by splitting in 1 and 2 direction (Figures 5.3(a) and (b)), while it fails by shear type failure in the 3 direction (Figure 5.3(a)). The dominant failure mechanisms in the principle directions 1 and 2 of $[\pm45°]_s$ composite samples at quasi-static strain rates are also shear banding and longitudinal splitting as shown in Figures 5.4(a) and (b). In the principle direction 3, the failure mechanism is the shear deformation (Figure 5.4(c)). At high strain rates, as similar with $[0°/90°]_s$ composite sample, $[\pm45°]_s$ composite sample fails by axial splitting in 1 and 2 direction (Figures 5.5(a) and (b)), while it fails by shear type failure in the 3 direction (Figure 5.5(a)). It is noted that at high strain rates the deformation predominantly proceeds with axial splitting, while shear banding and splitting are dominant in quasi-static testing.

(a) (b) (c)

Figure 5.2. $[0°/90°]_s$ failed composite samples in directions of (a) 1, (b) 2 and (c) 3

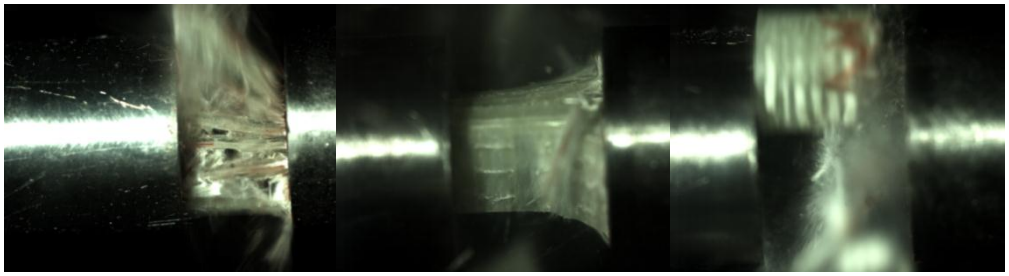

(a) (b) (c)

Figure 5.3. SHPB test of $[0°/90°]_s$ composite samples in principle directions(a)1, (b) 2 and (c) 3.

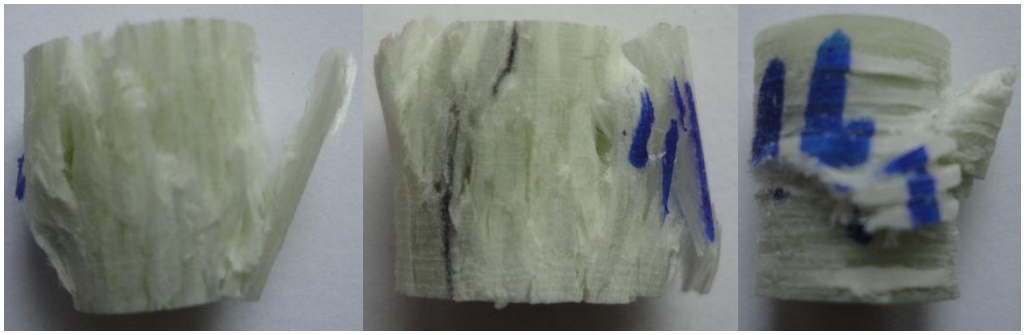

(a) (b) (c)

Figure 5.4. $[0°/90°]_s$ failed composite samples in directions of (a) 1, (b) 2 and (c) 3.

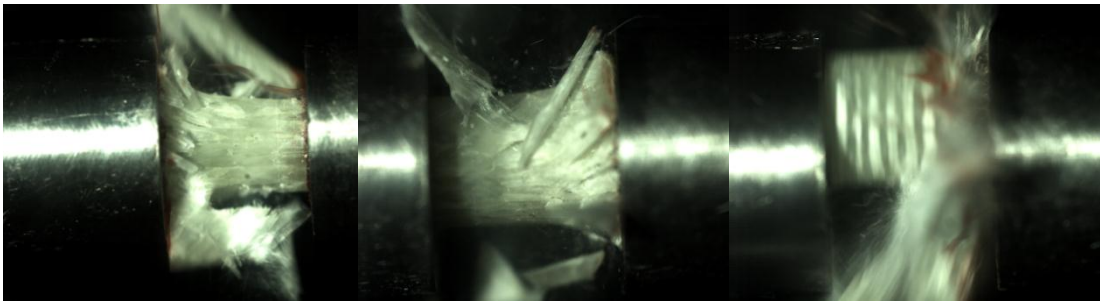

(a) (b) (c)

Figure 5.5. SHPB test of $[\pm 45°]_s$ composite samples in principle directions(a) 1, (b) 2 and (c) 3.

The shear strength in tension is the highest in the principal plane 12 and lowest in principal planes 23 and 31 directions. This is attributed to the fiber/matrix interface debonding in these directions. The major failure modes in shear testing are matrix cracking, fiber pull-out, fiber bundle pull-out and delamination as seen in Figure 5.6.

Figure 5.6. $[\pm 45°]_s$ failed composite samples in shear tests.

The curves in flexural testing are almost linear elastic up to the peak load, followed by a gradual softening then an abrupt load drop which corresponds with tensile fiber failure in the bottom plies. The flexural strength and flexural modulus slightly increases with the increasing specimen thickness. Figure 5.7 shows the picture of a failed specimen in flexure testing. The deformation mechanisms are the fiber fracture at the top plies while tensile fiber fracture at the bottom plies and delamination is observed.

Figure 5.7. Failed composite samples in flexure tests.

The interlaminar shear strength for the $[0°/90°]_s$ and $[\pm 45°]_s$ composite samples is very close to each other and it slightly changes with the fiber orientation. The typical failure mode, in the short beam test, is delamination in the plies as shown in Figure 5.8.

Figure 5.8. Delamination in the short beam test specimen.

5.4. Compression Properties of Aluminum Foam and Corrugated Aluminum Structures

In compression tests, cellular metals show a plateau stress region, which makes them available for energy absorbing applications where at a relatively low constant stress a large amount of deformation can be absorbed. The mechanical properties of the metallic foams depend on relative density and the yield strength and the plateau stress increase with the increasing relative density. The compression testing of corrugated Al structures shows that epoxy bonding of layers results in higher crushing stresses than brazed corrugated structure. The main reason for that is reduction of material strength due to the applied heat treatment in brazing. Although brazed sample cores show partly buckling and shearing without tearing, the corrugated epoxy bonded core show tearing in addition to buckling and shearing as depicted in Figure 5.9.

(a) (b) (c)

Figure 5.9. Corrugated big fin aluminum structures; (a) undeformed, (b) deformed brazed and (c) deformed epoxy bonded.

The deformation energy is assumed to be absorbed by the corrugated structures by a deformation occurring layer by layer sequence. First, the plastic bending and stretching of the core walls occur and then the bent core walls start to fold in a progressive axisymmetric manner. Moreover, the shear of the folded layers occurs and up and down layers of the corrugated panels move in the opposite directions. Finally, the densification starts when the shear of the layers is completed.

It should be noted that the manufacturing processes of the aluminum foams are more complicated and expensive than the corrugated structures. The aluminum foams show much more variations in mechanical properties at the same relative densities as compared with corrugated structure.

5.5. Low Velocity Impact Properties of Composite Plates

The low velocity impact force-time histories of $[0°/90°]_s$ and $[\pm 45°]_s$ composite samples are found quite similar to each other. It is noted that when the back surface splitting occurs, a sudden drop in the force-time history is seen. On the other hand, in the tests of no or little back surface splitting, there is not such a significant force drop. The contact of the impactor on the composite samples creates a linear force region at the beginning as the impactor is only pushing the sample down. The oscillations appear on the force-time history curve when damage starts to develop on the samples. The damage is in the form of delamination, crack or indentation. If the impact energy is high enough,

back surface splitting is noticed. If the energy absorbed by the specimen is not too high the impactor is pushed back and a rebound occurs. In the rebound case, the first force drop indicates the first material damage and the second force drop the initial lamina failure. If the sample has no residual internal energy to rebound the impactor, the impactor stops and this situation is known as saturation. In the saturation case, the first force drop indicates the material damage initiation and the second force drop the first lamina failure but after the second significant force drop the force almost stays constant for a while; then goes to zero. When the impactor energy is higher than the samples energy absorbing limit, the impactor passes through the sample. In this case, the force stays constant after the perforation because of the friction of the edges of the perforation hole against the lateral surface of the impactor.

When the impact tests are investigated, the results indicate that $[\pm 45°]_s$ composite samples with 5 mm thickness have the highest resisting force while the $[0°/90°]_s$ composite samples with 2 mm thickness have the lowest resisting forces. The maximum force increased with the increasing impact velocity for the whole samples. The rebound velocity of the $[\pm 45°]_s$ composite samples with 5 mm thickness is found 4.21 m/s, the saturation velocity is 7.30 m/s and the perforation velocity is 8.45 m/s. The front and back faces of 5 mm thick composite sample picture corresponding to the rebound, saturation and perforation cases are shown in Figures 5.10 (a-c), respectively.

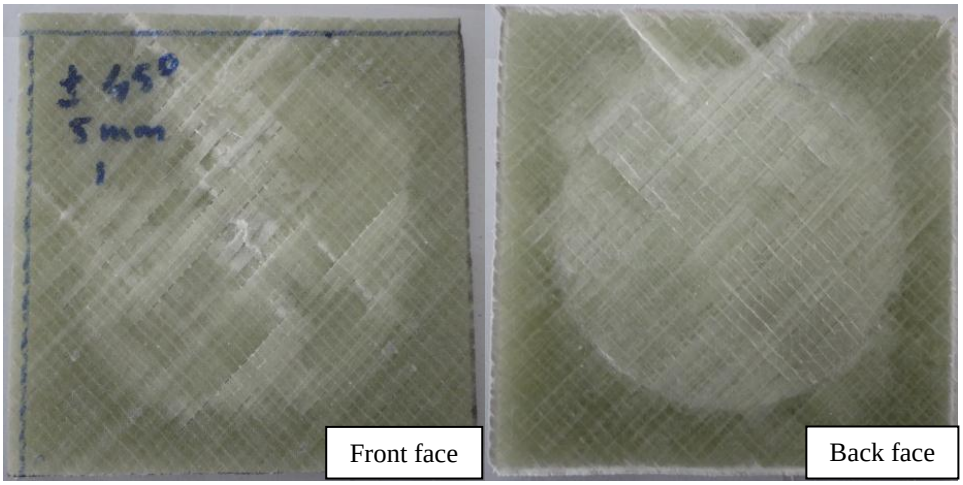

(a)

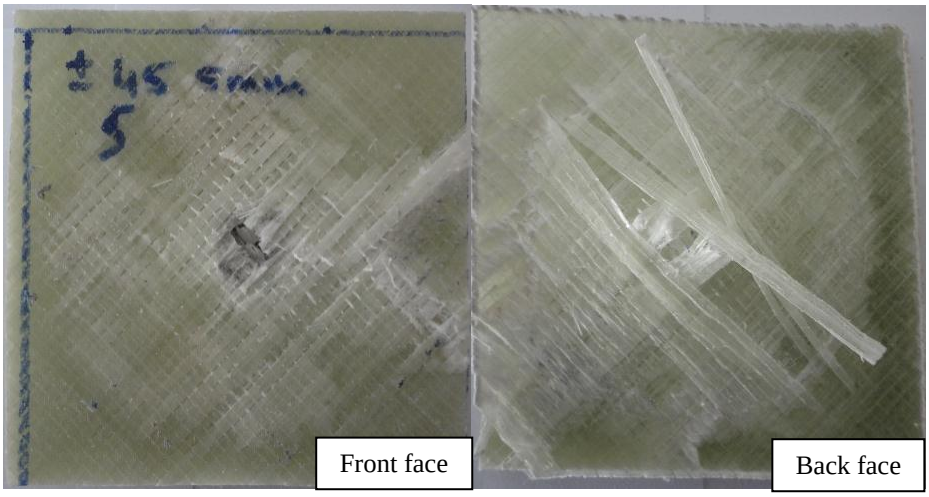

(b)

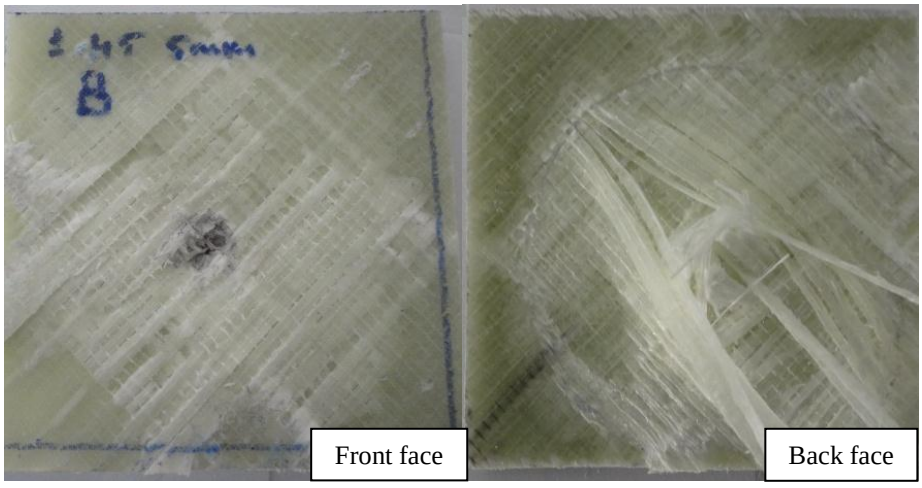

(c)

Figure 5.10. Interaction cases of the 5 mm $[\pm 45°]_s$ composite sample; (a) rebound, (b) saturation and (c) perforation.

Matrix cracking, debonding or delamination between the plies, fiber breakage and buckling and penetration are major energy absorbing damage mechanisms in the low velocity impact tests. Matrix cracks are usually oriented in the planes parallel to the fiber direction due to tension, compression and shear. A bending crack perpendicular to the laminate occurs on the tensile side because of the induced high tensile bending stresses. Generally, the bending stress causes the flexural deformation of the laminate. Delamination is the separation of plies which is a result of bending stiffness mismatch between the adjacent layers. Bending induced stresses are the major causes of the delamination. Fiber failure occurs after the matrix cracking and delamination are completed in damage process. Fiber failure occurs below the impactor because of the high local stresses and indentation effects and also on the non-impacted face due to high bending stresses. Penetration process takes place when the fiber failure reaches a critical level. The major energy absorbing mechanisms in penetration are; shear plug, delamination and elastic flexure.

When the impact tests are investigated in the point of energy absorption, $[\pm 45°]_s$ composite samples with 5 mm thickness have the highest energy absorbing characteristic because of the higher penetration resisting velocities. On the other hand, $[0°/90°]_s$ composite samples with 2 mm thickness have the lowest energy absorbing characteristic. The major failure mechanisms 5 mm $[0°/90°]_s$ composite samples in the rebound case are the matrix cracking along the fiber direction and fiber failure at the impact side (Figure 5.11). In the penetration case of the 5 mm thick $[0°/90°]_s$ composite sample, matrix cracking, delamination, fiber failure and shear plug formation are the energy absorbing deformation mechanisms (Figure 5.12).

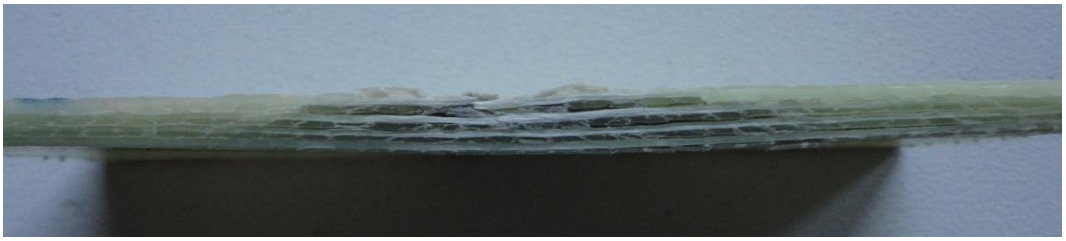

Figure 5.11. 5 mm thick $[0°/90°]_s$ composite sample cross-section for rebound case.

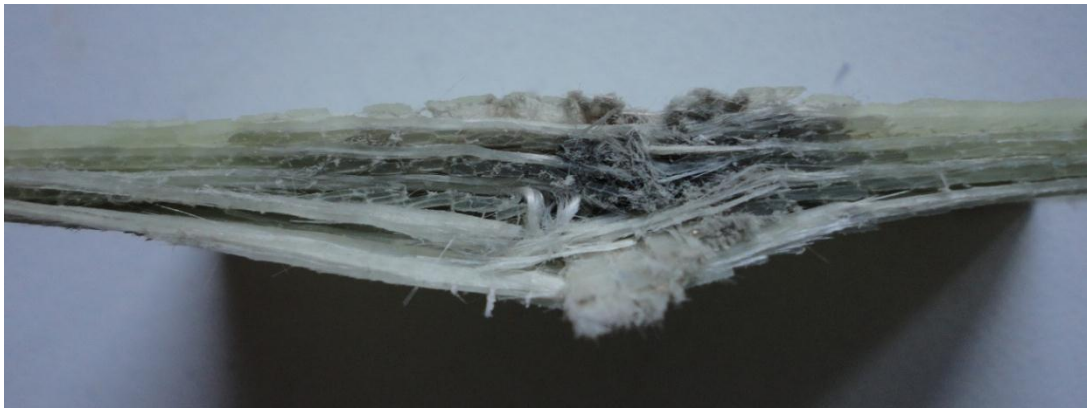

Figure 5.12. 5 mm thick $[0°/90°]_s$ composite sample cross-section for perforation case.

The deformation mechanisms of the $[\pm45°]_s$ composite sample with 5 mm thickness in the rebound case are the matrix cracking between the plies, delamination and fiber failure at the impact side (Figure 5.13). In the penetration case of the 5 mm thick $[\pm45°]_s$ composite sample are the matrix cracking, delamination, fiber failure and shear plug formation (Figure 5.14).

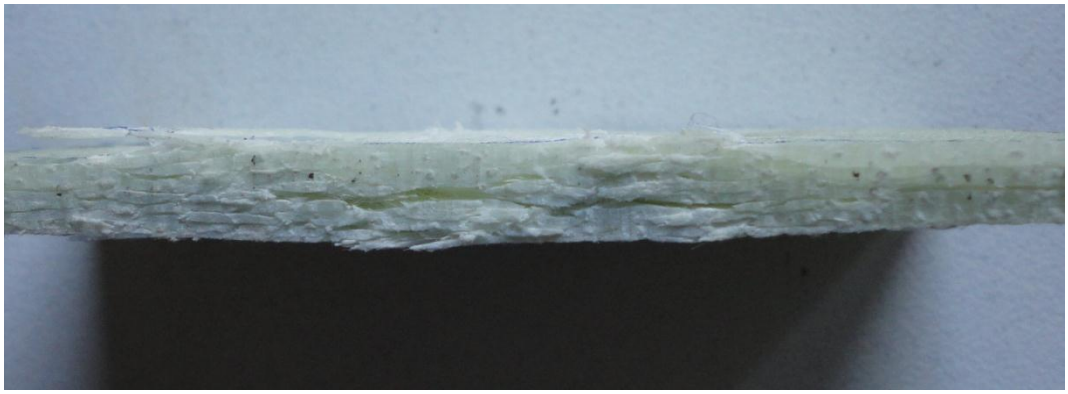

Figure 5.13. 5 mm thick $[\pm45°]_s$ composite sample cross-section for rebound case.

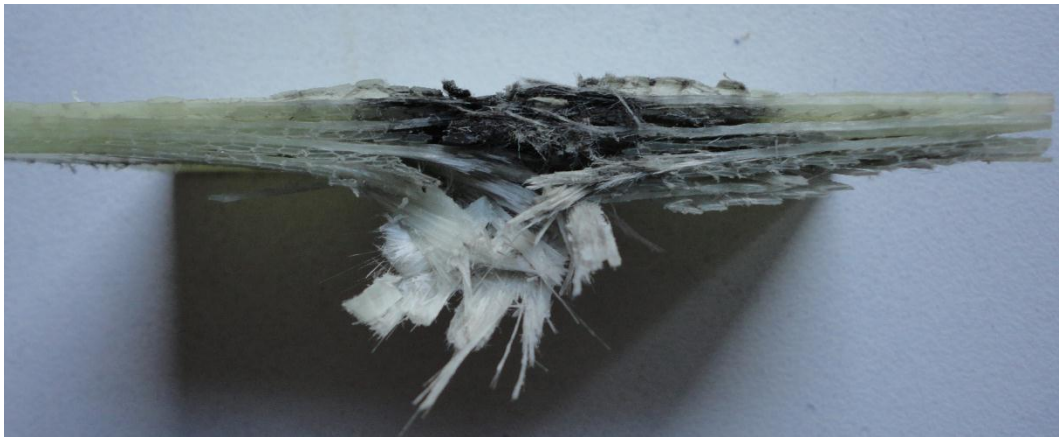

Figure 5.14. 5 mm thick $[\pm 45°]_s$ composite sample cross-section for perforation case.

5.6. Projectile Impact Properties of Composite Plates and Sandwich Structures

Composite laminates with different orientations and thicknesses, composite face sandwich structures with aluminum foam cores and corrugated aluminum cores, sandwich panels with corrugated aluminum and aluminum face sheets were subjected to projectile impact tests at velocities ranging from 127 m/s to 190 m/s. The main ambition in the projectile impact tests is, to simulate the foreign object damage on aircraft structures while flying and take-off or landing on the runways and obtain the most effective energy absorber. The maximum velocity of the projectile was determined as nearly 150 m/s based on the previous studies.

5.6.1. Projectile Impact Properties of Composite Plates

The impact velocity and exit velocity of the projectile were recorded by the velocity measuring system to determine the ballistic limit and energy absorption and the impact instant was recorded by a high velocity camera to see the deformation on the front face. A difficulty raised while measuring the residual velocity of the projectile because of the many small particles, fibers and shear plugs pushed out by the projectile. These materials trigger the velocity system before the projectile arrives and causes wrong measurements. The problem was solved by attaching a nylon bag between the

sensor and the target which stops the particles but enables the projectile pass with a negligible velocity loss.

When the impact velocity and the residual velocity are obtained from the experiments, the data are substituted into Equation 5.1 and 5.2, respectively. In Figure 5.15, the ballistic limit of $[0°/90°]_s$ and $[\pm45°]_s$ composite laminates with respect to thickness is given. It can be concluded that up to 2.5 mm thickness $[0°/90°]_s$ composite samples have higher ballistic limits but when the thickness increases $[\pm45°]_s$ composite laminates become more effective. Moreover, with the increasing thickness, the ballistic limit of the laminates increases for both orientations.

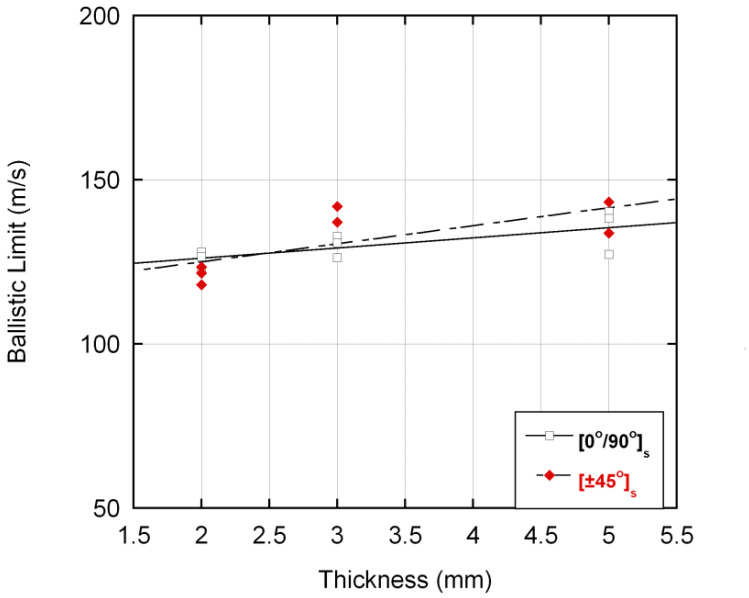

Figure 5.15. Ballistic limit of composite samples with respect to laminate thickness.

In Figure 5.16, the perforation energy of $[0°/90°]_s$ and $[\pm45°]_s$ composite laminates with respect to thickness is given. 3mm and 5 mm $[\pm45°]_s$ composite laminates have higher perforation energy than the $[0°/90°]_s$ counterparts. On the other hand, $[0°/90°]_s$ samples with 2 mm thickness have higher perforation energies.

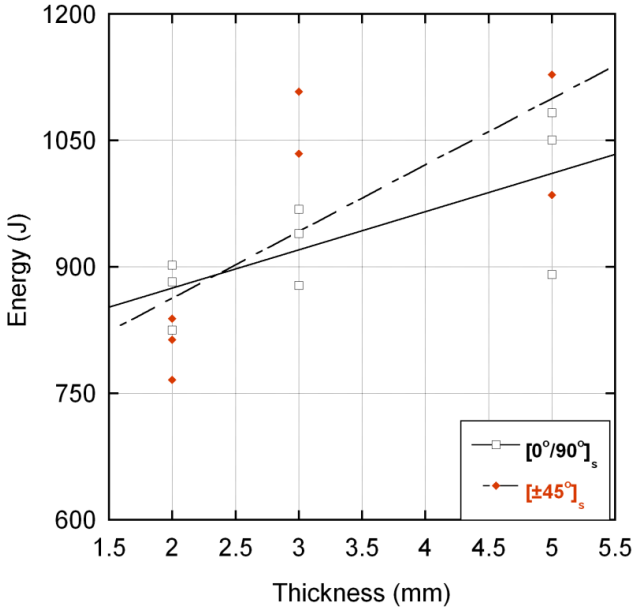

Figure 5.16. Perforation energy of composite samples with respect to laminate thickness.

In general, the initial contact of the projectile and the composite target occurs and a stress is created at the beginning. Then the projectile induces compressive stress on the layers and the fiber starts to break which is followed by the shear deformation also compressive and tensile stresses act on the front and back surfaces, delamination occurs. Finally shear plugging occurs because of the dynamic friction between the projectile and the target. In Figure 5.17, the deformation sequence of composite laminate is shown schematically.

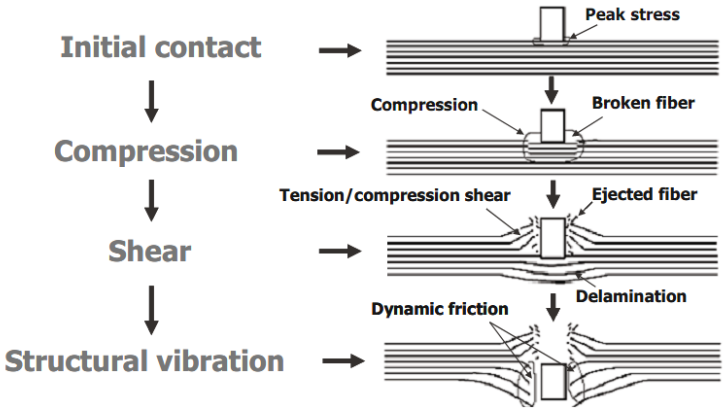

Figure 5.17. Deformation sequence of a composite plate at projectile impact. (Source: Abrate, 2011)

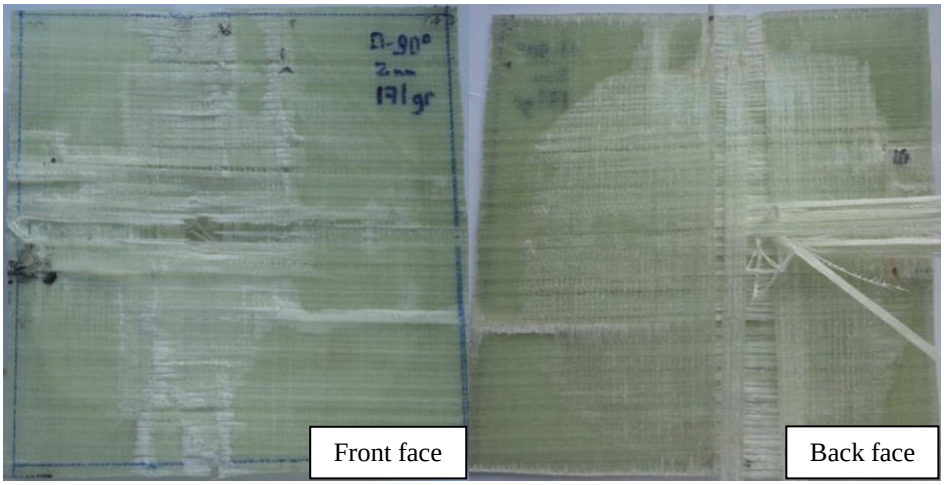

(a)

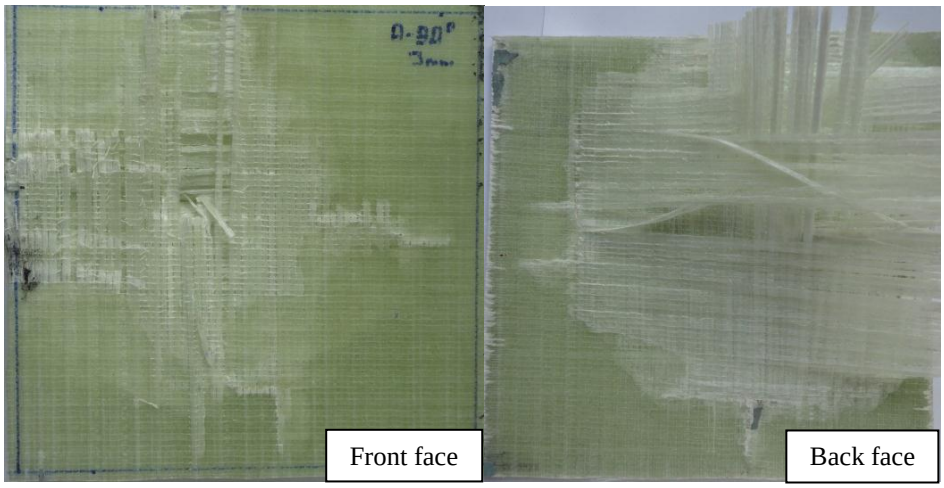

(b)

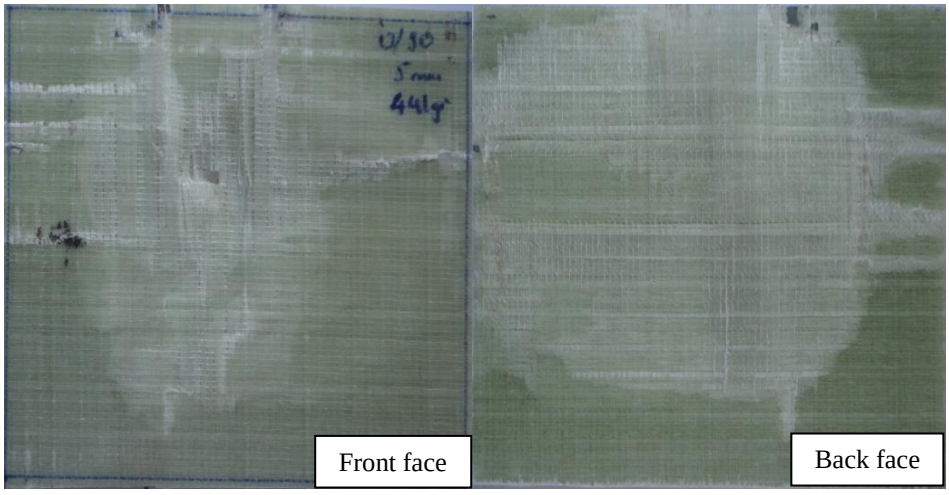

(c)

Figure 5.18. Deformations in the front and back faces of $[0°/90°]_s$ composite samples; (a) 2 mm thick, (b) 3 mm thick and (c) 5 mm thick.

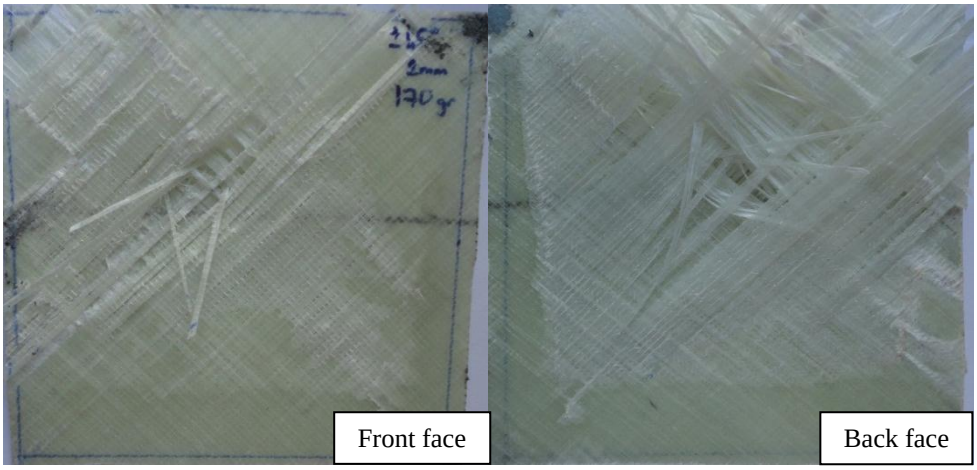

(a)

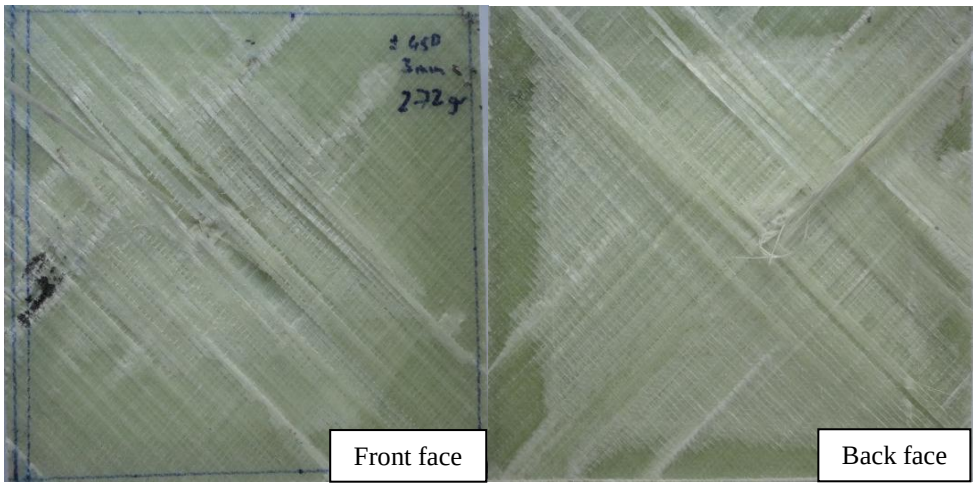

(b)

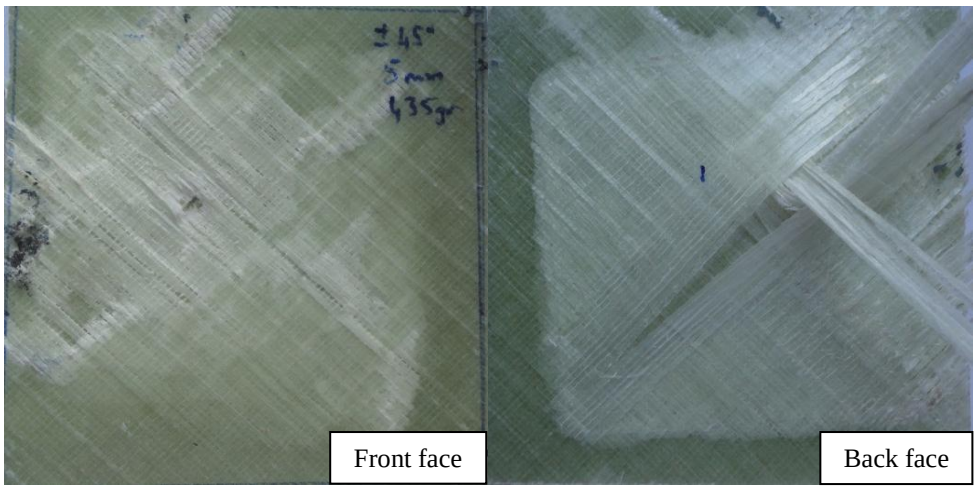

(c)

Figure 5.19. Deformations in the front and back faces of $[\pm 45°]_s$ composite samples; (a) 2 mm thick, (b) 3 mm thick and (c) 5 mm thick.

In Figure 5.18 (a-c) and 5.19 (a-c), the deformation mechanisms of the $[0°/90°]_s$ and $[\pm45°]_s$ composite plates are given. In both of the orientations; delamination, fiber breakage and shear plugging are the major failure modes. The amount of delamination on the back face increases with the decreasing thickness and becomes a global deformation instead of a localized deformation.

5.6.2. Projectile Impact Properties of Sandwich Structures

Projectile impact tests were conducted on sandwich structures with; aluminum foam core composite face sheets which have $[0°/90°]_s$ and $[\pm45°]_s$ fiber orientations with 2 mm, 3 mm and 5 mm thicknesses, corrugated aluminum core composite face sheets and corrugated aluminum core aluminum face sheets. Same experimental conditions were used in the tests to investigate the change of ballistic limit, energy absorption characteristics, effect of face and core thickness and effect of core density and thickness.

5.6.2.1. Projectile Impact Properties of Corrugated Al Core Al Sandwich Structures

Aluminum sandwich structures with big and small fin corrugated cores of the same number of layers were exposed to projectile impact testing. Both groups of samples have 7 layers of corrugated structures and 6 interlayers of 0.5 mm 1050 Al sheets but the thicknesses of the fins are different. The big fin cores is 9 mm and the small fin cores 4 mm in thickness and the total thickness of the sandwich structures with 1.5 mm face sheets is 70 mm and 34 mm, respectively. The average mass of the big fin corrugated aluminum core aluminum sandwiches is 1039 g and the density is approximately 371 kg/m^3. The small fin corrugated aluminum core aluminum sandwich is 931 g and the density is approximately 711 kg/m^3.

In Figure 5.20, the variation of the ballistic limit with the mass of the foam and corrugated sandwich core structures is shown. As the thickness of the corrugated sandwich core structure increases; while, the energy absorbed by the material decreases. Furthermore, the big fin corrugated structure with epoxy sticking has a higher ballistic

limit than the brazed counterpart. Small fin corrugated structure has higher ballistic limit than the other corrugated structure and 0.15 relative density aluminum foam. The empty space between the fins are less than the big fins so this increases its density and ballistic limit with respect to other corrugated structures and the face sheets at the bottom and top faces increase the ballistic limit with respect to 0.15 relative density aluminum foam. The energy absorbing mechanisms during the full penetration process are found as, the ductile hole formation at the front face, corrugated structure wall bending, folding and collapse at the core and shear plug and petalling on the back faces as shown in Figure 5.21.

In Figure 5.22 and 5.23, the impacted big and small fin corrugated cores cross-section pictures are shown sequentially. In big fin corrugated aluminum sandwich structures, the folding seems to only occur in the first layer around the tunnel of the projectile. In the other layers, the material fails because of compression at the point of contact, tension at the other side of the contact point and shear plugs at the back face. For small fin corrugated structure, folding occurs at all layers around the tunnel of the projectile and different from the big fin corrugated structure deformation is the back face delamination.

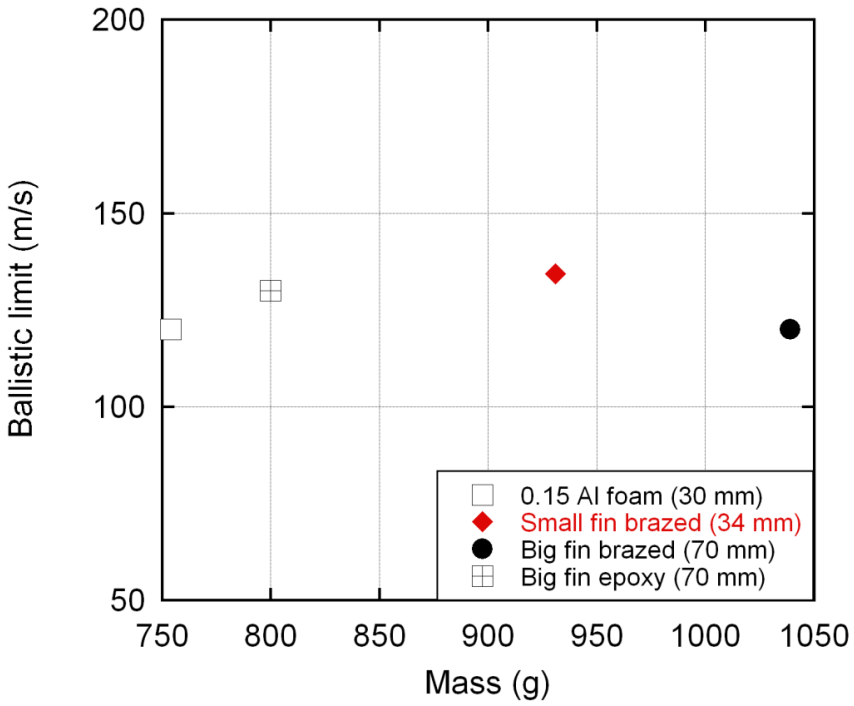

Figure 5.20. Ballistic limit and mass of the corrugated structures.

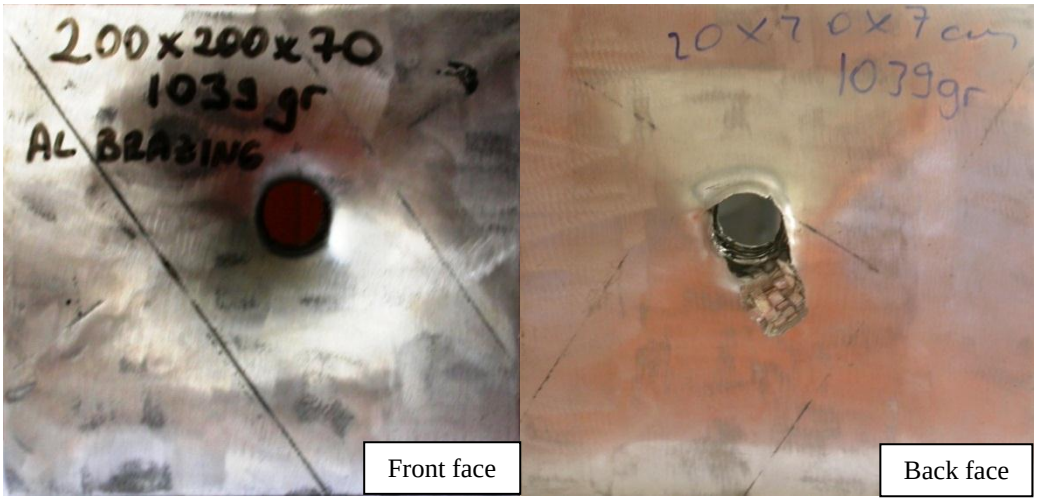

Figure 5.21. Front and back face deformations.

Figure 5.22. Big fin corrugated aluminum core aluminum sandwich cross-sectional view.

Figure 5.23. Small fin corrugated aluminum core aluminum sandwich cross-sectional view.

5.6.2.2. Projectile Impact Properties of Corrugated Al Core Composite Sandwich Structures

Big fin corrugated aluminum core composite sandwich structures with different face sheet thicknesses were tested to determine the ballistic limit and energy absorption capacity. All samples contain 6 layers of big fin corrugated aluminum structures and 5 interlayers of 0.5 mm thick 1050 Al sheets in the cores. Composite laminates with 2 mm, 3 mm and 5 mm thicknesses are used as the face sheets. The total thickness of the sandwich structures with 2 mm, 3 mm and 5 mm face sheet thicknesses are 60.5 mm, 62.5 mm and 66.5 mm, respectively. The average mass of the big fin corrugated aluminum core composite sandwiches with 2 mm face sheets is 887 g and the density is approximately 367 kg/m^3. For the big fin corrugated aluminum core composite sandwiches with 3 mm face sheets is 1008 g and the density is approximately 403 kg/m^3. Finally, for the big fin corrugated aluminum core composite sandwiches with 5 mm face sheets is 1413 g and the density is approximately 531 kg/m^3. In Figure 5.24, the variation of the ballistic limit with the mass of the corrugated aluminum core composite sandwich structures is shown. The ballistic limit of the sandwich structures increases with the increasing mass and the thickness of the composite face sheets. As the thickness of the sandwich structure increases, the energy absorbed by the material also increases. This is accomplished by increasing the thickness of the face sheets while keeping core thickness constant.

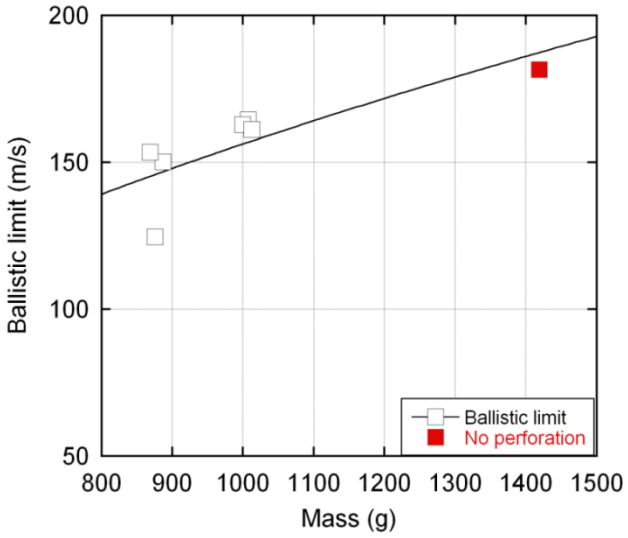

Figure 5.24. The relationship of mass and ballistic limit of corrugated aluminum core composite sandwiches.

The energy absorbing mechanisms during the impact are the onset delamination and matrix cracking, compression, tension and shear, fiber fracture and shear plug formation on the front face, corrugated structure wall bending, folding and collapse at the core and the onset delamination and matrix cracking, compression, tension and shear, fiber fracture and shear plug formation on the back faces if full penetration occur (Figures 5.25 (a-c)). There is a severe back face deformation because of the full penetration in Figures 5.25 (a) and (b), on the other hand there is little deflection and no deformation at the back face of Figure 5.25 (c) case because the projectile stuck in the core.

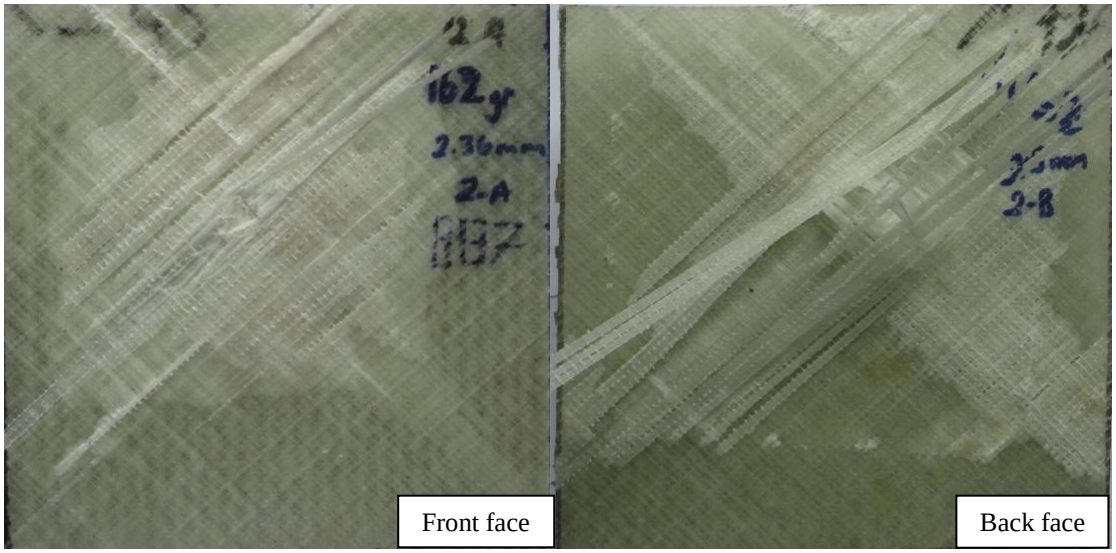

(a)

Figure 5.25. Deformations on the front and back face of the corrugated aluminum core composite sandwiches with (a) 2 mm thick composite laminates, (b) 3 mm thick composite laminates and (c) 5 mm thick composite laminates.

(cont. on next page)

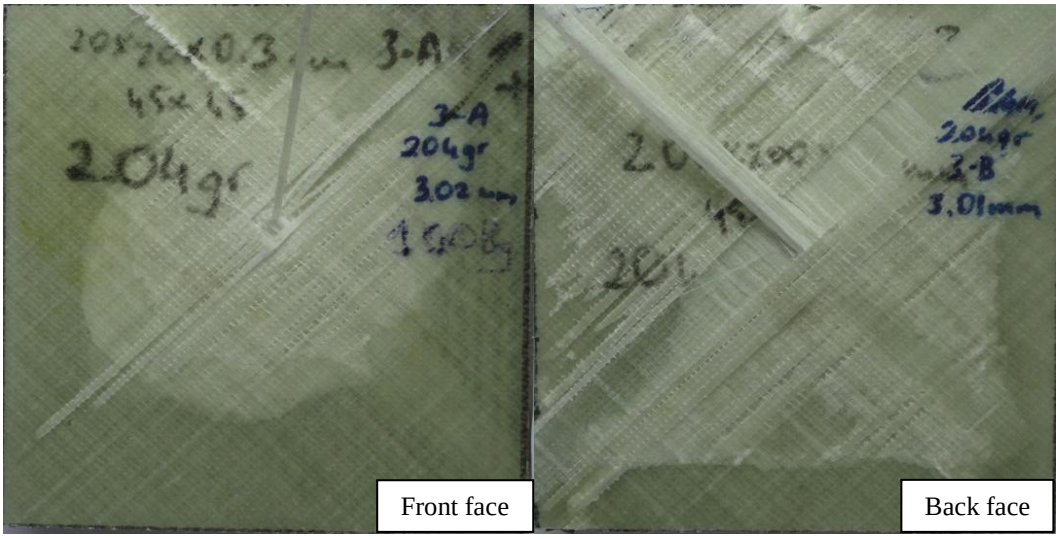

(b)

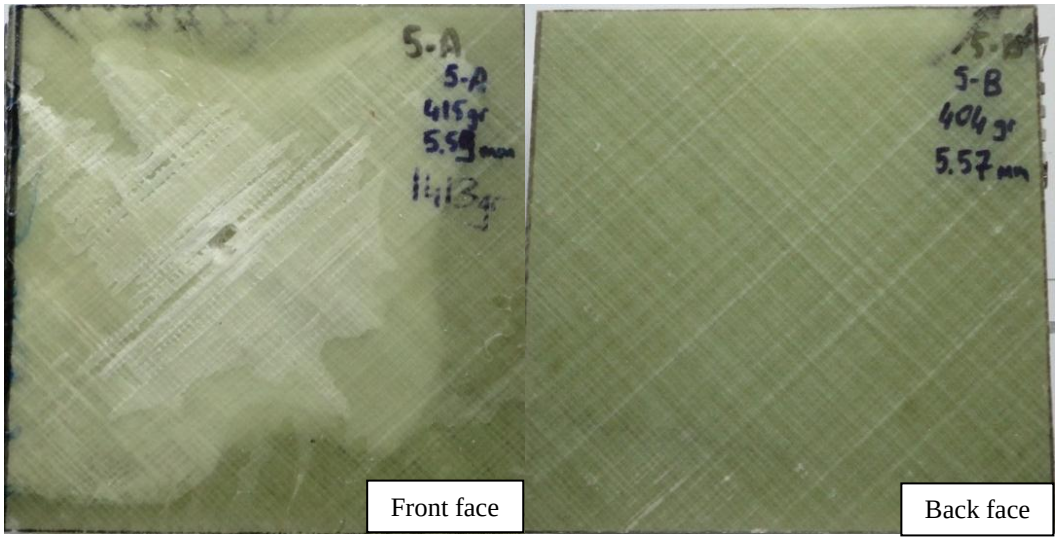

(c)

Figure 5.25. (cont.).

The deformations in the core materials of the sandwiches with 2, 3 and 5 mm face sheets at the cross-section are sequentially shown in Figure 5.26 (a-c). Figure 5.26(a) represents the deformation of the core when the impact velocity is 124.7 m/s which is lower than the ballistic limit of 2 mm thick composite laminate faced sandwich structure, Figure 5.26 (b) shows the deformation in the core when the impact velocity is higher than the ballistic limit of 3 mm thick composite laminate faced sandwich structure and Figure 5.26(c) depicts the deformation in the core when the impact velocity is lower than the ballistic limit of 5 mm thick composite laminate faced

sandwich structure. In general, the cores fail by bending, folding, compression, tension and shear plug. In 5 mm thick composite laminate faced sandwich structure, there is densification of the core at the contact point of the projectile, causing bulging and dishing of the corrugated aluminum core.

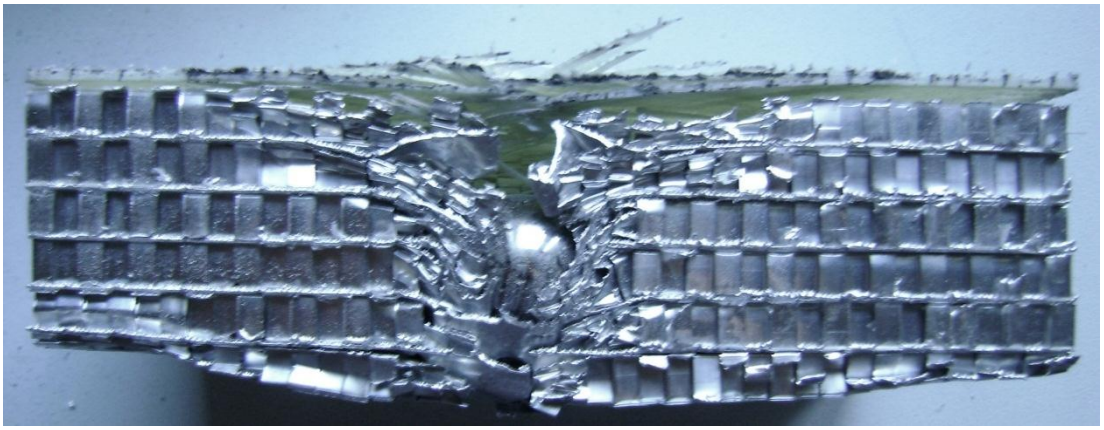

(a)

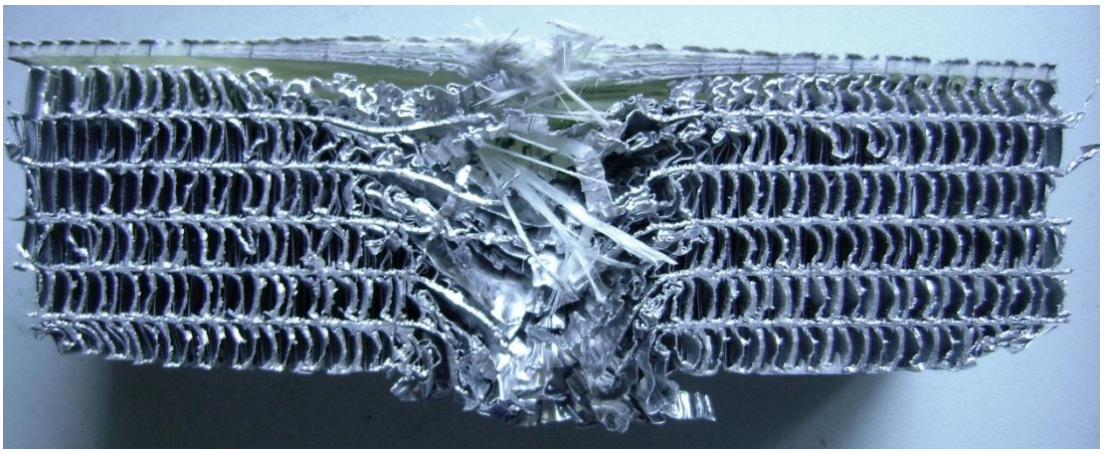

(b)

Figure 5.26. Cross-sectional view of corrugated aluminum core composite sandwiches; (a) 2 mm thick composite laminates, (b) 3 mm thick composite laminates, and (c) 5 mm thick composite laminates.

(cont. on next page)

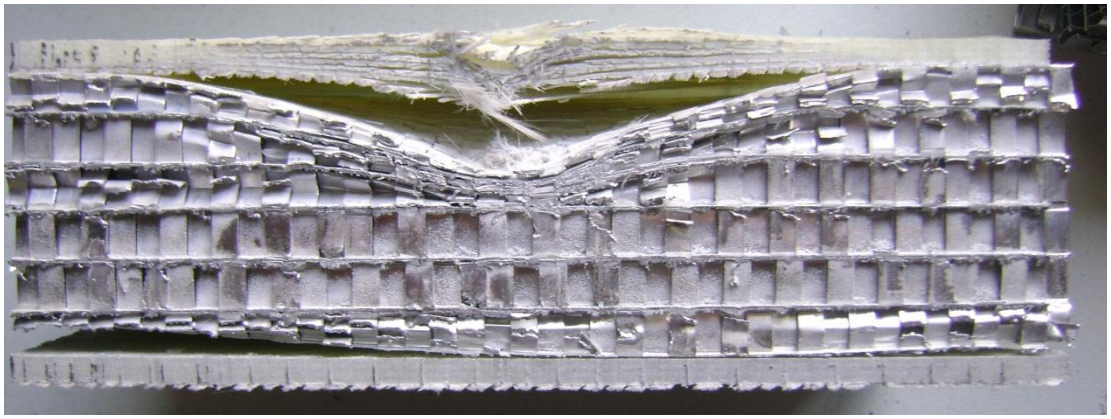

(c)

Figure 5.26. (cont.).

5.6.2.3. Projectile Impact Properties of Aluminum Foam Core Composite Sandwich Structures

Aluminum foam core composite sandwich structures with different face sheet thicknesses and core densities were projectile impact tested. All samples contain cores of 30 mm thick Alulight closed cell aluminum foam with 0.11 or 0.15 relative densities. Composite laminates with 2 mm, 3 mm and 5 mm thicknesses were used as the face sheets. The total thickness of the sandwich structures with 2 mm, 3 mm and 5 mm face sheet thicknesses is 34 mm, 36 mm, 40 mm, respectively. The average mass of the 0.11 relative density aluminum foam core composite sandwiches with 2 mm face sheets is 1072 g and the density is approximately 724 kg/m^3. For the 0.11 relative density aluminum foam core composite sandwiches with 3 mm face sheets is 1169 g and the density is approximately 860 kg/m^3. Finally, for the 0.11 relative density aluminum foam core composite sandwiches with 5 mm face sheets is 1597 g and the density is approximately 1174 kg/m^3. The average mass of the 0.15 relative density aluminum foam core composite sandwiches with 2 mm face sheets is 1280 g and the density is approximately 939 kg/m^3. For the 0.15 relative density aluminum foam core composite sandwiches with 3 mm face sheets is 1887 g and the density is approximately 1387 kg/m^3. Finally, for the 0.15 relative density aluminum foam core composite sandwiches with 5 mm face sheets is 1968 g and the density is approximately 1450 kg/m^3.

The variation of the ballistic limit (no perforation) with foam core density is shown in Figure 5.27. It is seen in the same figure that as the composite face thickness

increases the ballistic limit of the both sandwich structures increases. The ballistic limit of the sandwich structures also increases with the increasing density of the foam core. For the same face sheet thickness, 0.15 relative density aluminum foam has higher impact resistance.

The energy absorbing mechanisms during the impact are found to be onset delamination and matrix cracking, compression, tension and shear, fiber fracture and shear plug formation on the front face, bending, extension and compression of cell edges and cell walls, buckling of cell walls and collapse at the core and the onset delamination and matrix cracking, compression, tension and shear, fiber fracture and shear plug formation on the back faces if full penetration occurs (Figures 5.28 (a-c) and 5.29 (a-c)). In general, the cores fail by bending, extension, compression, buckling and collapse of the cell walls. Moreover, as the thickness of the composite laminate increases, the indentation of the projectile through the core decreases and also when the relative density of the core material increases, the amount of indentation decreases.

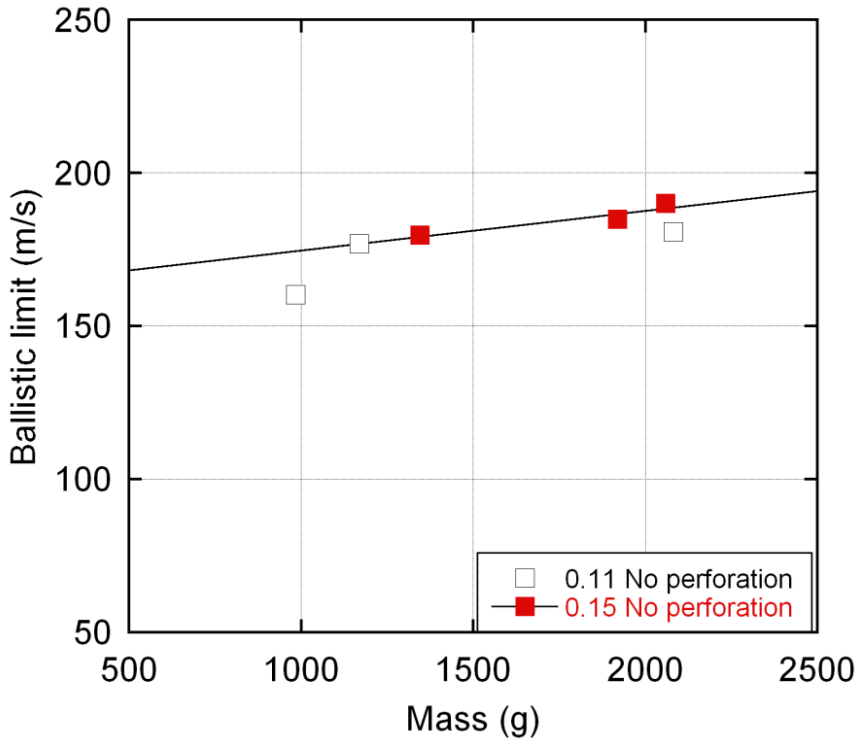

Figure 5.27. Projectile impact comparison of the 0.11 and 0.15 relative density aluminum foams.

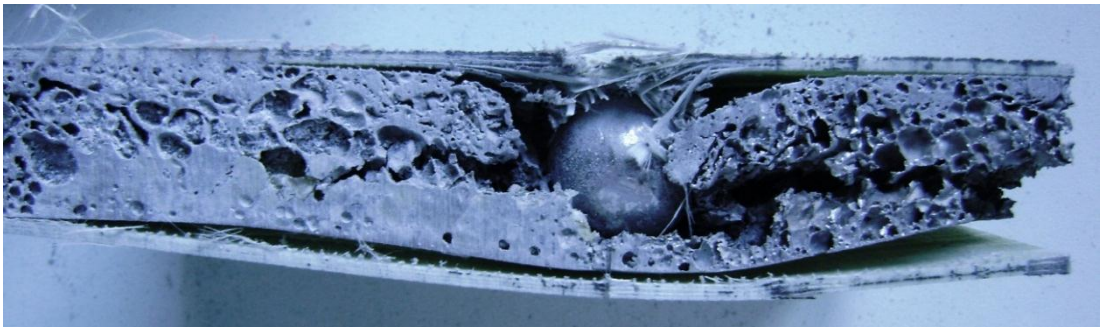

(a)

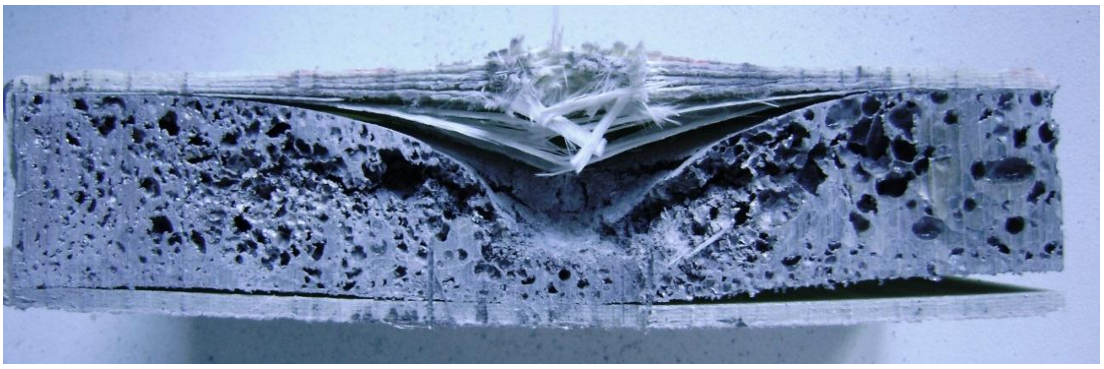

(b)

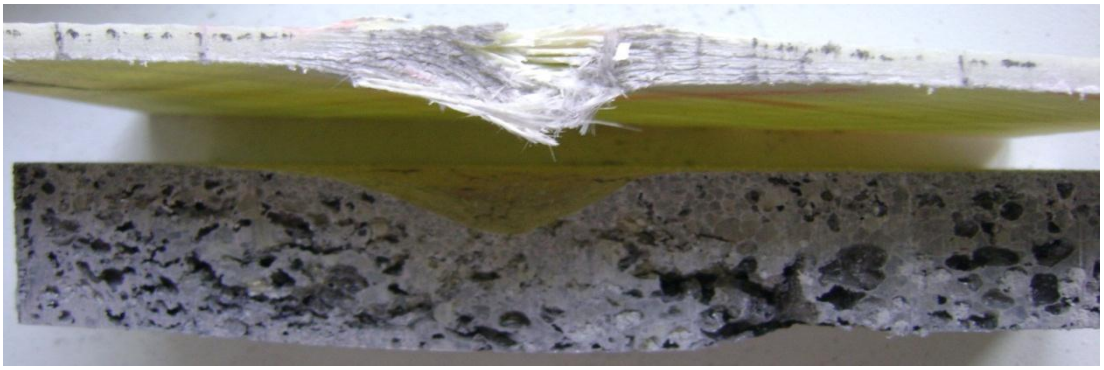

(c)

Figure 5.28. Cross-sectional view of 0.11 relative density aluminum foam core with (a) 2mm, (b) 3mm and (c) 5mm composite faced sandwiches.

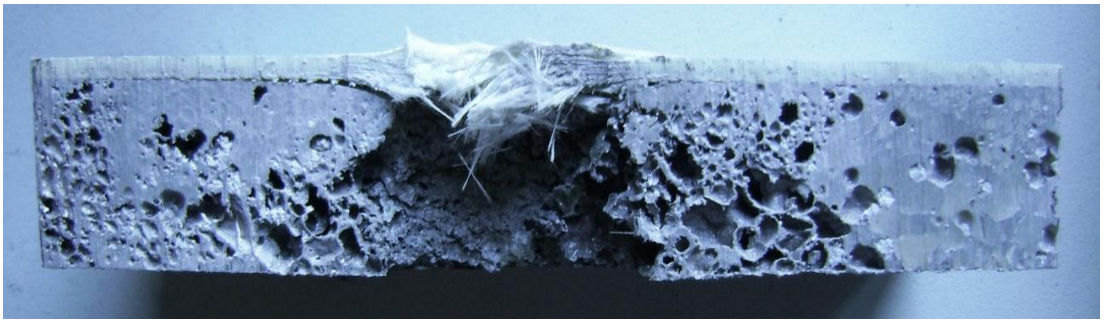

(a)

(b)

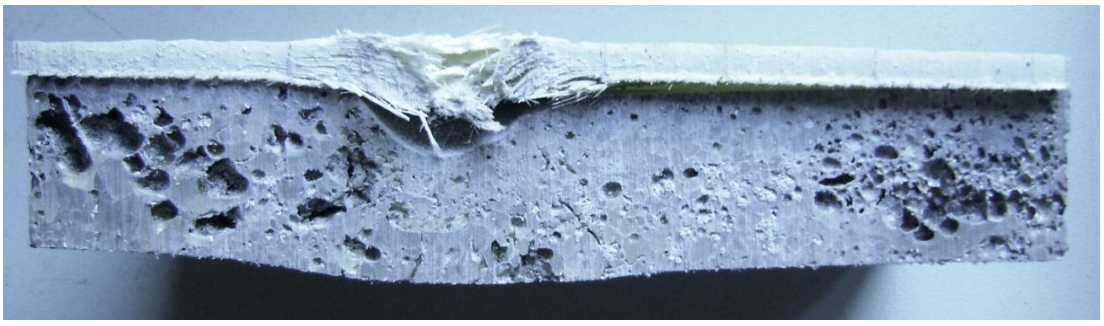

(c)

Figure 5.29. Cross-sectional view of 0.15 relative density aluminum foam core with (a) 2 mm, (b) 3 mm and (c) 5 mm composite faced sandwiches.

5.6.3. Comparison of Projectile Impact Properties of Test Materials

Figure 5.30 shows the variation of the ballistic limit of the composite laminates, corrugated core composite sandwich structures and aluminum foam core composite sandwich structures with the mass. It is concluded in the same figure that as the thickness of the material or mass of the material increases the ballistic limit of the sandwich increases. It is also clear that the use of core materials increases the ballistic limit of the sandwich structures. The application of the face sheets and aluminum foams increase the impact resistance and ballistic limit. Composite sandwich structures with 0.11 relative density aluminum foam core and composite sandwiches with 0.15 relative density aluminum foam core offer higher ballistic limits than the composite sandwiches with corrugated aluminum core. As the thickness of the face sheets increases the corrugated aluminum cores are observed to be more effective when the mass is considered. The results show that the corrugated aluminum structures have the potentials to be used as core material in composite sandwich structures.

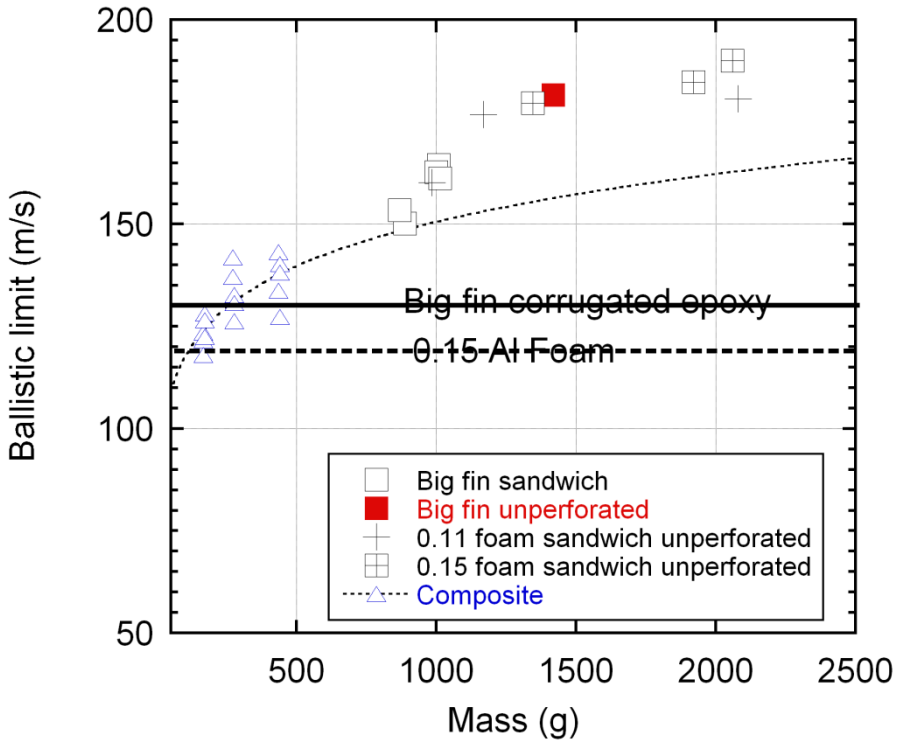

Figure 5.30. The comparison of the impact resistant materials used in the thesis.

CHAPTER 6

CONCLUSIONS

The projectile impact and energy absorption characteristics of the corrugated aluminum cored E-glass/polyester composite sandwich structures were determined at the impact velocities of 150 m/s. For comparison, E-glass/polyester sandwich structures cored with aluminum foam were also investigated. The test conditions were kept the same for each structure in order to identify the impact properties at the similar test conditions. The composite and the foam core composite sandwiches were produced by vacuum assisted resin transfer molding and the mechanical tests were performed on the composite and core samples based on ASTM. High strain rate tests were performed using a compression type split Hopkinson pressure bar and drop weight test set-up. Followings may be concluded;

- The fiber volume of the composites was determined to be less than the calculated volume fraction. This was attributed to the less number of layer used in the processing.
- The woven composite showed similar tensile properties in warp and weft directions but a significantly lower strength in through thickness direction.
- The composite showed a strain rate dependent compression behavior. As the strain rate increased both the stress and failure stress increased, while failure strain decreased. A more strain rate sensitivity was detected through thickness directions of both composite samples. The strain rate behavior was attributed to the strain rate sensitivity of the matrix.
- At high strain rates, the failure is dominated by the axial splitting in warp and weft directions, while proceeded with shear type in through thickness direction.
- Tsai-Wu failure criterion of the composite was in accord with experiments except 45 degrees.
- Epoxy mounted corrugated structures showed higher flow stresses than brazed samples. This was due to the softening of the Al sheets in the brazing process.

- In low velocity impact tests, $[\pm 45°]_s$ composites showed higher perforation velocities and energies than those of $[0°/90°]_s$ composite samples in through thickness direction.
- All the composite plates, 2, 3 and 5 mm, were perforated in projectile impact test, the highest ballistic limit was 142 m/s.
- Big fin corrugated sandwiches were perforated in projectile impact test except 5 mm composite faced.
- No perforation was found in the projectile impact testing of Al foam core sandwich structures.
- A comparison had shown that all core materials increased the ballistic limit of the composites. Al foam was found to show more resistance to projectile impact than corrugated structures. However, as the thickness of the face sheet increased corrugated structure distributed the impact load through a wider area.
- Corrugated structures were found to be effective as core materials. However, their structures should be optimized in terms of fin structure, interlayer Al sheet thickness and the alloy used.

For the future works, the tests done in this study can be modeled and analyzed in Ls-Dyna to compare the results. The optimization of the corrugated aluminum structure can be made to improve the ballistic performance. Corrugated composite cores can be manufactured to compare with the aluminum foams and corrugated aluminum structures. Furthermore, the blast performance of the corrugated cores can be investigated.

REFERENCES

[1] I. M. Daniel, *et al.*, "Deformation and failure of composite sandwich structures," *Journal of Thermoplastic Composite Materials*, vol. 16, pp. 345-364, Jul 2003.

[2] A. S. Herrmann, *et al.*, *Sandwich structures technology in commercial aviation - Present applications and future trends*. Dordrecht: Springer, 2005.

[3] W. J. Cantwell and J. Morton, "Impact perforation of carbon fibre reinforced plastic," *Composites Science and Technology*, vol. 38, pp. 119-141, 1990.

[4] Z. Guoqi, *et al.*, "Penetration of laminated Kevlar by projectiles--I. Experimental investigation," *International Journal of Solids and Structures*, vol. 29, pp. 399-420, 1992.

[5] Z. Guoqi, *et al.*, "Penetration of laminated Kevlar by projectiles--II. Analytical model," *International Journal of Solids and Structures*, vol. 29, pp. 421-436, 1992.

[6] S. W. R. Lee and C. T. Sun, "Modeling Penetration Process of Composite Laminates Subjected to a Blunt-Ended Punch," in *23rd International Sampe Technical Conference : Advanced Materials / Affordable Processes*. vol. 23, R. L. Carri, *et al.*, Eds., ed Covina: Soc Advancement Material & Process Engineering, 1991, pp. 624-638.

[7] S. W. R. Lee and C. T. Sun, "Ballistic Limit Prediction of Composite Laminates by a QuasiI-Static Penetration Model," in *Advanced Materials : Meeting the Economic Challenge / Advancements in Synthesis and Processes*. vol. 24, T. S. Reinhart, *et al.*, Eds., ed Covina: Soc Advancement Material & Process Engineering, 1992, pp. T497-T511.

[8] C. T. Sun and S. V. Potti, "A simple model to predict residual velocities of thick composite laminates subjected to high velocity impact," *International Journal of Impact Engineering*, vol. 18, pp. 339-353, Apr 1996.

[9] S. T. Jeno, *et al.*, "Predicting the Ballistic Limit for Plain Woven Glass Epoxy Composite Laminate," *International Journal of Impact Engineering*, vol. 15, pp. 451-464, Aug 1994.

[10] S. S. Morye, *et al.*, "Modelling of the energy absorption by polymer composites upon ballistic impact," *Composites Science and Technology*, vol. 60, pp. 2631-2642, 2000.

[11] H. H. Billon and D. J. Robinson, "Models for the ballistic impact of fabric armour," *International Journal of Impact Engineering*, vol. 25, pp. 411-422, Apr 2001.

[12] H. M. Wen, "Penetration and perforation of thick FRP laminates," *Composites Science and Technology,* vol. 61, pp. 1163-1172, 2001.

[13] X.-D. Cui, *et al.*, "Study on Ballistic Energy Absorption of Laminated and Sandwich Composites," *Key Engineering Materials,* vol. 306-308, pp. 739-744, 2006.

[14] E. P. Gellert, *et al.*, "A study of the effect of target thickness on the ballistic perforation of glass-fibre-reinforced plastic composites," *International Journal of Impact Engineering,* vol. 24, pp. 445-456, May 2000.

[15] N. Naik, *et al.*, "Ballistic impact behaviour of woven fabric composites: Parametric studies," *Materials Science and Engineering: A,* vol. 412, pp. 104-116, 2005.

[16] H. L. Gower, *et al.*, "Ballistic impact response of laminated composite panels," *International Journal of Impact Engineering,* vol. 35, pp. 1000-1008, 2008.

[17] B. Cheeseman, "Ballistic impact into fabric and compliant composite laminates," *Composite Structures,* vol. 61, pp. 161-173, 2003.

[18] C. Ulven, "Effect of projectile shape during ballistic perforation of VARTM carbon/epoxy composite panels," *Composite Structures,* vol. 61, pp. 143-150, 2003.

[19] G. Faur-Csukat, "Development of Composite Structures for Ballistic Protection," *Materials Science Forum,* vol. 537-538, pp. 151-159, 2007.

[20] G. A. O. Davies, *et al.*, "Impact damage and residual strengths of woven fabric glass/polyester laminates," *Composites Part a-Applied Science and Manufacturing,* vol. 27, pp. 1147-1156, 1996.

[21] G. Belingardi and R. Vadori, "Low velocity impact tests of laminate glass-fiber-epoxy matrix composite material plates," *International Journal of Impact Engineering,* vol. 27, pp. 213-229, Feb 2002.

[22] E. Sevkat, *et al.*, "Drop-weight impact of plain-woven hybrid glass–graphite/toughened epoxy composites," *Composites Part A: Applied Science and Manufacturing,* vol. 40, pp. 1090-1110, 2009.

[23] W. Hou, *et al.*, "Ballistic impact experiments of metallic sandwich panels with aluminium foam core," *International Journal of Impact Engineering,* vol. 37, pp. 1045-1055, 2010.

[24] A. Hanssen, *et al.*, "A numerical model for bird strike of aluminium foam-based sandwich panels," *International Journal of Impact Engineering,* vol. 32, pp. 1127-1144, 2006.

[25] A. M. Roach, *et al.*, "The penetration energy of sandwich panel elements under static and dynamic loading. Part I," *Composite Structures,* vol. 42, pp. 119-134, Jun 1998.

[26] G. a. C. Reyes Villanueva, W. J., "The high velocity impact response of composite and FML-reinforced sandwich structures," *Composites Science and Technology,* vol. 64, pp. 35-54, 2004.

[27] D. Zhou and W. Stronge, "Ballistic limit for oblique impact of thin sandwich panels and spaced plates," *International Journal of Impact Engineering,* vol. 35, pp. 1339-1354, 2008.

[28] L. Aktay, *et al.*, "Prediction of impact damage on sandwich composite panels," *Computational Materials Science,* vol. 32, pp. 252-260, 2005.

[29] W. Goldsmith, *et al.*, "Perforation of cellular sandwich plates," *International Journal of Impact Engineering,* vol. 19, pp. 361-379, May-Jul 1997.

[30] V. Rubino, *et al.*, "The dynamic response of clamped rectangular Y-frame and corrugated core sandwich plates," *European Journal of Mechanics a-Solids,* vol. 28, pp. 14-24, Jan-Feb 2009.

[31] D. D. Radford, *et al.*, "The response of clamped sandwich beams subjected to shock loading," *International Journal of Impact Engineering,* vol. 32, pp. 968-987, Jun 2006.

[32] L. A. C. a. R. B. Pipes, *Experimental characterization of advanced composite materials,* 2nd edition ed. NewYork: CRC press, 1997.

[33] S.P.Timoshenko, *Strength of Materials,* 3rd edition ed. Malabar: Krieger, 1984.

[34] S. Abrate. (2011). *Impact Engineering of Composite Structures*. *526*.